NASA Contractor Report 3640

Aeroelastic Loads Prediction for an Arrow Wing

Task I - Evaluation of R. P. White's Method

Christopher J. Borland

CONTRACT NAS1-15678
MARCH 1983

25th Anniversary
1958-1983

NASA

NASA Contractor Report 3640

Aeroelastic Loads Prediction for an Arrow Wing

Task I - Evaluation of R. P. White's Method

Christopher J. Borland
Boeing Commercial Airplane Company
Seattle, Washington

Prepared for
Langley Research Center
under Contract NAS1-15678

National Aeronautics
and Space Administration

**Scientific and Technical
Information Branch**

1983

CONTENTS

LIST OF TABLES

LIST OF FIGURES

LIST OF FIGURES (Concluded)

SUMMARY

The accurate prediction of loads on flexible, low aspect-ratio wings is critical to the design of reliable and efficient aircraft. The conditions for structural design frequently involve nonlinear aerodynamics.

Under previous NASA contracts (NAS1-12875, NAS1-14141, and NAS1-14962) a large experimental data base for three wing shapes was obtained, and linear theoretical methods were evaluated. The current contract, NAS1-15678, extends the evaluation of state-of-the-art theoretical predictive methods to two separated-flow computer programs and also evaluates a semi-empirical method for incorporating the experimentally measured separated-flow effects into a linear aeroelastic analysis.

The resultant three tasks have been documented separately. This volume describes the evaluation of R. P. White's (RASA Division of Systems Research Laboratories) separated-flow method (Task I). The evaluation of The Boeing Company's Three-Dimensional Leading-Edge Vortex (LEV) code (Task III) is presented in NASA CR-3642. The development and evaluation of a semi-empirical method to predict pressure distributions on a deformed wing by using an experimental data base (Task II) is described in NASA CR-3641.

The method of R. P. White was developed for moderately swept wings with multiple, constant-strength vortex systems. The flow on the highly swept wing used in this evaluation is characterized by a single vortex system of continuously varying strength. The data comparisons, as currently formulated, show that this method does not predict the pressure distribution on this highly swept wing.

INTRODUCTION

Accurate analytical techniques for the prediction of the magnitude and distribution of aeroelastic loads are required in order to achieve an optimum design of the structure of large flexible aircraft. Uncertainties in the characteristics of loads may result in an improper accounting for aeroelastic effects, leading to understrength or overweight designs and unacceptable fatigue life. In addition, the correct prediction of load distribution and the resultant structural deformation is essential to the determination of the aircraft stability and control characteristics, control power requirements, and flutter boundaries. The alternative to using satisfactory analytical techniques is the increased use of expensive, time-consuming wind tunnel testing for each aircraft configuration.

The problem of accurate load prediction becomes particularly acute for aircraft with low aspect-ratio wings where critical design conditions occur in the transonic speed regime. In this region, at typical design angles of attack, the flow is generally nonlinear – mixed flow, embedded shocks, separation, and vortex flow.

A program was started in 1974 to systematically obtain experimental pressure data for an arrow wing throughout the subsonic, transonic, and low supersonic Mach numbers. This program was comprised of three NASA contracts: NAS1-12875, NAS1-14141, and NAS1-14962 (documented in refs. 1 through 12). As the specific objective was to understand the change in load with aeroelastic deformation, three wing shapes were tested – all with the same planform and thickness distribution. The first wing was flat (no camber or twist); the second has a spanwise twist (typical of aeroelastic deformation) but no camber; and the third has the same twist with camber superimposed.

In addition to the creation of a data base, which is useful for evaluating aeroelastic effects, a second objective was to evaluate state-of-the-art theoretical methods that might be used for this purpose. Primarily these methods were linear. The evaluations showed that linear theories are adequate at low angles of attack typical of cruise conditions and are basically capable of predicting loading changes due to smooth changes in wing shape at these low angles. However, at the higher angles of attack typical of structural design conditions, these methods are not useful because the flow is nonlinear due to leading-edge separation of the flow. The limited comparisons that were made with advanced separated-flow methods indicated some hope even though the aerodynamic panel model available at that time was very crude (only a few panels to represent the camber surface).

The current evaluation of methods for predicting pressure distributions when the flow is separated is divided into three tasks. Two currently available computer codes were evaluated in Tasks I and III, and an approach involving semi-empirical corrections to linear theory was investigated in Task II. The three tasks are essentially independent efforts and are documented separately: Task I, an evaluaton of R. P. White's computer code in this document; Task II, the development and evaluation of a semi-empirical method in NASA CR-3641; and Task III, an evaluation of Boeing's Three-Dimensional Leading-Edge Vortex computer code in NASA CR-3642.

The computer code evaluated in Task I is the method of R. P. White of the RASA Division of Systems Research Laboratories, which models the vortex as a concentrated region of vorticity over the wing, and adds the results of this phenomenon to that of the linearized flow over a thin wing. The NASA arrow-wing configuration data base described above was used for this evaluation to determine the possible applicability of this method to the prediction of aeroelastic loads on highly swept wings. The following are discussed: theoretical basis of White's method; implementation of the method in a computer code; modeling of the arrow wing for analysis by the method; comparisons of calculated and experimental data; and the results of the evaluation.

SYMBOLS

b	wing span, cm
BL	buttock line, cm; distance outboard from model plane of symmetry
c	section chord length, cm
$\bar{c}$, M.A.C.	mean aerodynamic chord length, cm
C_B	surface bending moment coefficient referenced to y_{ref}, positive wingtip up
C_C	surface chord force coefficient; positive aft
C_c	section chord force coefficient; positive aft
C_M	surface pitching moment coefficient, referenced to 0.25 M.A.C.; positive leading edge up
C_m	section pitching moment coefficient referenced to section leading edge; positive leading edge up
$C_{m.25c}$	section pitching moment coefficient referenced to section 0.25c; positive leading edge up
C_N	surface normal force coefficient; positive up
C_n	section normal force coefficient; positive up
C_p	pressure coefficient = $\frac{\text{measured pressure} - \text{reference pressure}}{q}$
D	body diameter, cm
M	Mach number
MS	model station, cm; measured aft along the body centerline from the nose
p_s	static pressure, kN/m^2
p_t	total pressure, kN/m^2
q	dynamic pressure, kN/m^2
S	reference area used for surface coefficients, cm^2
S_h	area of streamwise strip associated with a pressure station, cm^2; used in summation of section force coefficients (app. B)
V_∞	free stream velocity

x,y,z	general coordinates for distances in the longitudinal, lateral, and vertical directions respectively
y_{ref}	distance outboard of model centerline of the bending moment reference point, cm
α	corrected angle of attack, degrees; the angle between the wing-root chord and the relative wind measured in the model plane of symmetry; includes compensation for sting deflection, tunnel-flow angularities, and wall effects; positive nose up with respect to relative wind
α_{sec}	wing twist angle relative to wing reference plane, degrees; positive leading edge up
β	angle of sideslip, degrees; positive nose left with respect to relative wind
δ	control surface deflection, degrees; positive leading edge down for leading edge (see exception in app. B) and trailing edge down for trailing edge
η	fraction of wing semispan, y/(b/2)
Λ	sweep angle, degrees; measured from a line perpendicular to the model centerline, positive aft
ϕ	angle defining location of pressure orifices on the surface of the cylindrical body at a constant MS, degrees; measured from the top of the body

Subscripts:

L.E.	leading-edge control surface
r	wing root
s	referenced to segment of local chord
T.E.	trailing-edge control surface

DATA BASE

The data obtained, both experimental and theoretical, have been presented in several papers (refs. 1 through 3) and are presented in more detail in numerous NASA reports (refs. 4 through 12).

WIND TUNNEL MODELS

The configuration chosen for this study was a thin, low aspect-ratio, highly swept wing mounted below the centerline of a high fineness-ratio body. The general arrangement and characteristics of the model are shown in figure 1. Two complete wings were constructed for contract NAS1-12875, one with no camber or twist and one with no camber but with a spanwise twist variation. A third wing with camber and twist was constructed for contract NAS1-14962. Deflectable control surfaces were available on all three of these wings.

The three wings, body, and fin used to create this data base are described in detail in appendix A. The wings all have the same planform, thickness distribution, and placement of orifices. The twisted wing and the cambered-twisted wing have the same twist, i.e., the coordinates of the leading edges and trailing edges of the two wings are the same. This twist distribution is shown in figure 2. Sections at the root, midspan, and tip of the cambered-twisted wing (fig. 3) show not only the camber but the position of the sections of the cambered-twisted wing and the twisted wing, relative to the wing reference plane (flat wing). The flat wing had a sharp leading-edge segment in addition to the rounded leading-edge segment common to all three wings.

The capability to measure the detailed load distribution on the wing and body of this configuration was provided by distributing 300 pressure orifices on the model. Each wing had 217 pressure orifices equally divided into seven streamwise sections on the left half. Orifices were located on both the top and bottom surfaces at the chordwise locations shown in figure 4. Pressure orifices were located on the body in five streamwise rows of 15 orifices each. An additional eight orifices in the area of the wing-body junction made a total of 83 orifices on the left side of the body.

WIND TUNNEL TESTING

The experimental data used in this study were obtained in the Boeing Transonic Wind Tunnel (BTWT) under NASA contracts NAS1-12875 and NAS1-14962. A description of the tunnel and tests are in appendix A. The current study was limited to the wings that had both leading-edge and trailing-edge control surfaces undeflected. Table 1 shows a summary of these data.

DATA

The measured pressures were edited, as necessary, to account for plugged or leaking orifices or missing data points. The pressure coefficients were then integrated, as described in appendix B, to obtain streamwise section coefficients and total surface coefficients. When pressure coefficients were required at points other than where measured, a linear interpolation was used.

Table 1.–Summary of Subsonic/Transonic Test Conditions by Test and Run Number

Contract	Test number	Mach number							Data document
		0.40	0.70	0.85	0.95	1.00	1.05	1.10	
Flat wing, rounded leading edge									
NAS1-12875	BTWT 1415	269	263	267	266	268	264	262	NASA CR-132727
Flat wing, sharp leading edge									
NAS1-12875	BTWT 1415	368	366	372	374	373	367	365	NASA CR-132727
Twisted wing, rounded leading edge									
NAS1-12875 NAS1-14962	BTWT 1415 BTWT 1627	450 15	445 14	449 13	447 12	448 11	446 10	444 –	NASA CR-132727 NASA CR-165701
Cambered-twisted wing, rounded leading edge (fin off)									
NAS1-14962	BTWT 1627	43	41	40	39	38	37	–	NASA CR-165701

THEORY AND ASSUMPTIONS

The basis of R. P. White's prediction method (ref. 13) is that the flow over a wing at high angles of attack may be considered as the sum of the contributions of two quite separate phenomena:

1) the flow over a thin wing, which is described by the linearized small disturbance potential equation, and

2) the flow due to a concentrated region of vorticity, which occurs above the upper wing surface and originates due to the flow separation along the leading edge.

These two phenomena are inconsistent as the presence of a region of vorticity violates the irrotational assumption of potential flow.

Earlier investigators, however, have found that this assumption can be used with reasonable engineering accuracy. Brown and Michael (ref. 14), for example, represented the flow over a slender delta wing as a two-dimensional potential flow in the cross-flow plane, with a concentrated potential vortex added into the field above the wing. In their method, the strength and position of the vortex was determined by solution of the potential-flow equations subject to the boundary conditions of no flow through the surface, smooth flow at the leading edge (Kutta condition), and a condition of zero force on both the vortex and the feeding sheet transmitting vorticity from the wing leading edge to the concentrated vortex. Later investigators used similar methods with minor variations. A highly sophisticated version of this approach is the Boeing-developed Leading-Edge Vortex (LEV) method of reference 15, which uses a three-dimensional panel method for the wing surface and the rolled-up leading-edge vortex (evaluation discussed in Task III documentation, NASA CR-3642).

The White method differs from these previous approaches in several aspects. Some of these may be described as follows:

1) The position of the vortex is determined by the user and given as input data. This information may be determined from theoretical or empirical methods, such as that of Smith as described in reference 16, or from experimental data. The results of the program are very sensitive to the vortex location chosen.

2) The strength of the vortex is determined iteratively from calculated leading-edge vortex strength given by an incompressible doublet-lattice panel method, not as part of a simultaneous solution of the coupled lifting-surface potential vortex flow as in the Brown and Michael method (ref. 14). The strength of the vortex is assumed constant in White's method.

3) The region of vorticity is considered to be of finite extent and is given by a self-similar solution of the Navier-Stokes equation. The suction pressures on the surface determined by the vortex solution are superimposed on those calculated by the doublet-lattice lifting-surface method.

4) The vortex is considered to be free, i.e., not connected to the wing surface by a feeding sheet transmitting vorticity from the leading edge to the vortex core. Thus, the Kutta condition of smooth flow off the leading edge cannot be inherently satisfied.

Further details of White's method, including a description of the viscous flow solutions and the empirical constants used, may be found in reference 13.

The method described in reference 13 has been incorporated in a computer code for use on the Control Data Corporation 6600/Cyber 175 series of computers. This code is described fully in reference 17. During the performance of the contract, the code was received from RASA, installed on the Boeing computers, checked out and validated, and modified as required for the NASA arrow-wing configuration.

VALIDATION OF THE COMPUTER CODE

The case used by RASA for development and validation of the code was a moderate aspect-ratio, moderately swept planform with a strake based on the F-4 airplane (see ref. 13). The flow over this planform at high angles of attack is characterized by the presence of multiple vortex systems (strake, leading edge, and wing tip) that tend to increase in strength only over a small portion of the lifting surface and behave as free vortices over most of the wing. An excellent comparison of measured and calculated pressures was obtained by RASA for the F-4 wing.

The F-4 planform was used as a test case to validate the code after its installation at Boeing. After receiving additional corrections from RASA, the calculated results were in agreement with those provided by RASA (within the accuracy of computer and operating system differences).

MODIFICATION OF THE COMPUTER CODE

The computer code, as received, needed several modifications before application to the NASA arrow wing could be attempted. These modifications were made jointly by Boeing and RASA personnel and may be described as follows:

1) The airfoil section definition in the code, as received from RASA, is given by a polynomial definition (see ref. 18) representing the NACA 00XX series of airfoils (where XX is the thickness ratio in percent chord). This airfoil is assumed constant across the span. Different airfoil definitions were incorporated in the code by including the polynomial coefficients obtained from a least squares fit of the surface ordinates used to construct the arrow-wing wind tunnel models.

2) In the original code, the mean plane of the wing was assumed to be flat. For the twisted and cambered-twisted arrow-wing configurations, modification of the surface geometry to account for spanwise variations was required.

3) As received, the code did not contain an iteration procedure to automatically determine vortex strength from the potential-flow calculation. This was incorporated by RASA during the contract.

Other modifications, which were discussed but not made, were the incorporation of compressibility (the current code is for incompressible flow), inclusion of a feeding sheet model, iteration of the vortex position as well as strength (this was included in the code but not found to be operative), and modifications to the separated flow criteria described in reference 13.

APPLICATION OF THE METHOD

After installation and validation of the code, the NASA arrow-wing configuration was modeled for input to the program. The cases that were run for comparison with the experiment consisted of the flat, twisted, and cambered-twisted wings at a Mach number of 0.40 and an angle of attack of 16°. In addition, the flat wing was run at an angle of attack of 8°. The results of these cases and the comparison with experimental data are described in this section.

MODELING

The modeling consists of three general parts. The procedure for this modeling, along with the difficulties that were encountered, are described.

PLANFORM GEOMETRY AND PANELING

Surface paneling of the wing is required for implementation of the doublet-lattice method for the linear part of the flow. Paneling in the code is either manual (user input of constant percent chord (x/c) and constant fraction of semispan (y/(b/2)) locations for the panel edges) or automatic (a standard set of nondimensional paneling). The automatic option was used for the arrow wing. Figure 5 shows the paneling used. The code assumes the paneling is the same for the upper and lower surfaces of the wing.

SURFACE GEOMETRY

In the White method, the boundary condition of no flow through the surface is specified on the actual airfoil surface. It is, therefore, necessary to provide an accurate representation of the surface thickness, camber, and twist distributions. In the original code, an NACA 00XX series airfoil was used with the surface shape represented by the polynomial description given in reference 18. The wing was assumed to be symmetric about the mean plane, i.e., no twist or camber. In order to represent the various configurations of the NASA arrow wing, development of new surface representations and modifications to the code were required.

The polynominal coefficients to represent the thickness of these airfoils (with both rounded and sharp leading edges) were obtained with a least squares fit of the surface coordinates of the airfoil (z/c versus x/c). Table 2 shows the form of the polynomial used to fit the geometry and the coefficients obtained. These coefficients were used to define surface geometry and slope in White's code. A comparison of the forward portions of the rounded- and sharp-airfoil sections, as used, are shown in figure 4.

The nondimensional airfoil sections also varied as a function of span because the trailing edge is a constant 0.0254 cm (0.01 in.) thick due to manufacturing constraints on the models. It was assumed for purposes of incorporating the geometry in White's code that a constant spanwise section could be used. This assumption caused some difficulty as the answers varied greatly, depending on whether the root section or tip section was chosen as representative.

The root section, which has a relatively sharp trailing edge, was originally used to define the airfoil. This gave large bumps in the pressure distribution near the trailing edge, which were not observed in the experimental data. As previously mentioned, the

Table 2.–Polynomial Coefficients for Airfoil Definition

$$\left(\frac{z}{c}\right)_u = A_1 + A_2\sqrt{\frac{x}{c}} + \sum_{n=1}^{10} A_{n+2}\left(\frac{x}{c}\right)^n \qquad \left(\frac{z}{c}\right)_l = -\left(\frac{z}{c}\right)_u$$

		Rounded L.E. root section	Rounded L.E. tip section	Sharp L.E. tip section
Upper surface	A_1	0.00	0.00	0.00
	A_2	.10095021E+00	.10093185E+00	0.00
	A_3	-.20101451E+00	-.19951709E+00	.26196052E+00
	A_4	.47539204E+00	.45661141E+00	-.10548058E+01
	A_5	-.22656037E+01	-.20088269E+01	-.54993659E+01
	A_6	.11448311E+02	.97680669E+01	.68051393E+02
	A_7	-.38620912E+02	-.32431182E+02	-.28466430E+03
	A_8	.81190343E+02	.67393001E+02	.65260528E+03
	A_9	-.10711414E+03	-.88096659E+02	-.89728052E+03
	A_{10}	.86521116E+02	.70665296E+02	.73847873E+03
	A_{11}	-.39099350E+02	-.31768977E+02	-.33591049E+03
	A_{12}	.75650206E+01	.61223848E+01	.65013256E+02

tip section had a slight bluntness at the trailing edge when measured in percent of chord because of manufacturing constraints on the model. Figure 6 shows the nondimensional geometry of the trailing edge of the root and tip sections with the vertical scale exaggerated. When the tip section (blunt trailing edge) was used, the bumps in the pressure distribution were not observed. A comparison of the resulting pressures for the two airfoil definitions is shown in figure 7. The cause of the discrepancy is not known at this time, but it is suspected to be anomalies in the numerical method for calculating the linear part of the pressure distribution. The modeling for the subsequent comparisons used the definition that was based on the tip airfoil.

Camber and twist distributions were added to the basic symmetrical surface to obtain models for comparison with experimental data on the twisted and cambered-twisted wings. These distributions for the model are defined in appendix A.

VORTEX MODELING

The vortex modeling requires both the vertical and horizontal location of the vortex. In the analysis of the F-4 wing performed by RASA, flow visualization techniques were used to determine the horizontal and vertical locations. Three-dimensional flow-visualization data were not available for the arrow wing, although surface pressure data could be used to determine the horizontal location. Only a single vortex system was modeled for the arrow wing, whereas three systems were used for the F-4.

Several different approaches were tried in modeling the vertical position of the vortex. The initial approach was to obtain the vertical position by assuming that the angle between the wing and the vortex was one half the angle of attack (see sketch), i.e., 8° for an angle of attack of 16°. This is the theoretical limit for a concentrated force-free vortex above a slender delta wing of vanishing aspect ratio. For this assumption, the vortex had almost no effect on the wing surface pressures, and considerable disagreement was observed in the comparison of calculated and measured pressures.

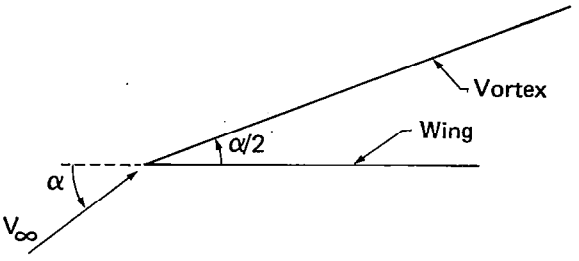

The second approach was to use a vortex similar to that used for the F-4 wing; namely, one half the angle of attack to the 0.25 root-chord position, then at a constant distance above the surface to the trailing edge, then parallel to the free stream aft of the trailing edge (see sketch). With this modeling, a significant effect of the vortex on the surface pressures was observed. However, this effect appeared to be exaggerated compared with experimental pressures, i.e., more suction pressure due to the vortex.

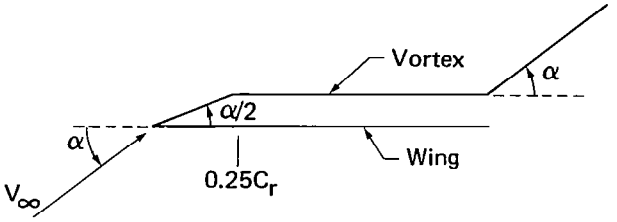

At the suggestion of RASA personnel, the third approach was to use the method described by Smith (ref. 16) to locate the vortex position. This method assumes conical flow and, therefore, provides a straight vortex emanating from the apex of the wing and includes the effect of both angle of attack and semi-apex angle. Starting the vortex at the wing apex gives a very large, unrealistic suction peak. Therefore, the vortex was started at a location 20 percent of the root chord aft of the apex. As shown in figure 8, at 16° angle of attack, the horizontal location of the vortex, as given by the Smith method, agreed excellently with that determined from the suction peaks in the experimental data for the flat wing with rounded leading edge. The vertical location of the vortex (Smith method) shows the vortex above the wing at approximately one quarter of the angle of attack. For 8° angle of attack, however, the pressure data indicates that the vortex starts along the leading edge at about the midspan point, and proceeds aft in a curving path to the trailing edge, with a fairly significant disagreement with the conical flow assumption, as shown in figure 8.

The Smith method for placing the vortex was used for all calculated results.

In White's method, the leading edge vortex is assumed to contain a central core region of predominantly axial turbulent flow. In the core, the circumferential velocity is assumed to vary directly with vortex radius, resembling a solid-body rotation. Outside the core, the circumferential velocity varies inversely with radius, similar to a potential vortex. The core radius is given by the solution to the viscous flow equations, but an initial value must be chosen. The initial core radius is a user-input parameter and is ideally obtained from photographic flow-visualization data which, however, were not available for the arrow wing. A nominal value of 0.0107 m (0.035 ft) was initially chosen. In an attempt to improve the comparisons, a sensitivity study on the initial core

radius was performed. Higher and lower values of 0.0427 m (0.140 ft) and 0.0030 m (0.01 ft) were tried. A comparison of the calculated pressures for these three values is shown in figure 9. It may be seen that no consistent trend in the pressures can be observed due to this change in core radius, therefore, the initial core radius of 0.0107 m (0.035 ft) was used for the study.

COMPARISON OF ANALYSIS AND TEST

Calculations on the arrow-wing configuration were performed using White's code, modified to account for the exact surface geometry. Since the code was limited to incompressible flow, the results are compared to experimental data at a Mach number of 0.40, the lowest Mach number tested. Most of the calculations were done for an angle of attack of 16°. Some calculations were later performed at about 8°.

Chordwise pressure distributions on the arrow wing were measured at seven spanwise locations: y/(b/2) = 0.09, 0.20, 0.35, 0.50, 0.65, 0.80, and 0.93. The code, as written, evaluates pressures at y/(b/2) = 0.01 and at each increment of 0.02 across the wing. This difference in fraction of semispan of 0.01, where it occurs, was assumed negligible in comparing calculated and experimental pressures.

Figures 10 through 13 show a comparison of calculated and experimental data at 16° angle of attack. Figure 10 shows the calculated and measured upper-surface pressure coefficients for the flat wing with sharp leading edge. The pressure distribution is not predicted accurately and is not adequate for design loads. The calculated pressure distributions show "humps," which may be interpreted as the effect of vortex suction. At one section (y/(b/2) = 0.20), the comparison of theoretical and experimental pressures shows fairly good agreement; unfortunately, this appears to be merely fortuitous. The vortex effect is far more pronounced in the experimental data, particularly at midspan (y/(b/2) = 0.35 and 0.50), where the values of the theoretical data are much lower than the experimental. On the outboard wing (y/(b/2) = 0.65, 0.80, and 0.93), the experimental data indicate that the flow is separated, i.e., the pressure level is nearly constant without significant pressure recovery near the trailing edge. The calculated values, on the other hand, are typical of classical linear theory, with high suction pressures near the leading edge and recovery to static pressure near the trailing edge.

White's method contains a "separated-flow criteria" for determining whether, at any point on the wing, separation has occurred. A section was assumed to be stalled if the net aerodynamic angle of attack (the geometric angle of attack minus the induced angle) was greater than an empirically defined angle. Considerable effort on this separated flow criteria failed to reproduce the experimentally observed behavior. It would appear, therefore, that significant difficulties in modeling the vortex flow remain in the code. Similar observations can be made for the flat, twisted, and cambered-twisted wings with the rounded leading edge, shown in figures 11 through 13.

A comparison of experimental and calculated data for the flat wing with rounded leading edge at 8° angle of attack is shown in figure 14. The comparison at 8° is better than that at 16°, probably because at 8° the vortex is present only over the outboard portion of the wing (fig. 8), and it is weaker as well. This is consistent with the observed difficulties in predicting the effect of the vortex. Since at 8° angle of attack the flow is predominately potential, the vortex would be expected to have a smaller effect on the lifting-surface pressure relative to the linear portion predicted by the doublet-lattice method at 8° than at 16° angle of attack.

CONCLUSIONS

White's method has been evaluated for its applicability to the calculation of surface pressures that are due to separated vortex flow on a highly swept configuration using a variety of surface shapes. The shapes are those that would be typical of the deformed geometry of a low aspect-ratio wing under aeroelastic load.

From the comparisons of experimental and calculated surface pressures, it does not appear that the method is capable of accurate predictions of pressure with the modeling that is available in the code. The method was developed for applicability to less highly swept wings with multiple vortex systems. These vortices were not characterized by the continuous variation of vortex strength that is typical of highly swept configurations. Furthermore, the method is highly sensitive to the placement of the vortex in the flow field. Although this information could be made available from wind tunnel tests for an undeformed wing, the use of the method in an aeroelastic solution would require that the solution be capable of predicting changes in the vortex position in response to surface geometric changes due to aeroelastic deformation.

It cannot be recommended, therefore, that the method be considered further for incorporation in an aeroelastic analysis unless significant changes are made to:

- the assumptions used in modeling the vortex system, especially to allow changes in vortex strength,
- the solution procedure to allow the vortex to be properly repositioned automatically as part of the solution, and
- include the effects of compressibility.

Boeing Commercial Airplane Company
P. O. Box 3707
Seattle, Washington 98124
May 1982

APPENDIX A

DESCRIPTION OF DATA BASE

WIND TUNNEL MODELS

The configuration chosen for this study was a thin, low aspect-ratio, highly swept wing mounted below the centerline of a high fineness-ratio body. The general arrangement and characteristics of the model are shown in figure A-1. Two complete wings were constructed for contract NAS1-12875, one with no camber or twist and one with no camber but with a spanwise twist variation. A third wing with camber and twist was constructed for contract NAS1-14962. Deflectable control surfaces were available on all three of these wings.

FLAT WING

The mean surface of the flat wing is the wing reference plane. The nondimensional wing thickness distributions (shown in table A-1) deviate slightly from a constant for all streamwise sections to satisfy a manufacturing requirement for a finite thickness of 0.0254 cm (0.01 in.) at the trailing edge. The wing was designed with a full-span, 25-percent chord, trailing-edge control surface. Sets of fixed angle brackets allowed streamwise deflections of $\pm 4.1^{\circ}$, $\pm 8.3^{\circ}$, $\pm 17.7^{\circ}$, and $\pm 30.2^{\circ}$, as well as 0.0°. A removable full-span leading-edge control surface (15 percent of streamwise chord) could be placed in an undeflected position and also drooped 5.1° and 12.8° with fixed angle brackets. Both the leading- and trailing-edge control surfaces extended from the side of the body (0.087 b/2) to the wingtip and were split near midspan (0.570 b/2). The inboard and outboard portions of the control surfaces were able to be deflected separately and were rotated about points in the wing reference plane. An additional leading-edge control surface for this wing was constructed with a sharp (20° included angle) leading edge to examine the effects of leading-edge shape. The surface ordinates and slopes of this leading-edge segment were continuous with those of the flat wing at the leading-edge hingeline (table A-1). The sharp leading edge was smoothly faired from 0.180 b/2 into the fixed portion of the rounded leading edge at 0.090 b/2.

TWISTED WING

The mean surface of the twisted wing was generated by rotating the streamwise section chord lines about the 75-percent local chord points (trailing-edge control surface hingeline). The spanwise variation of twist is shown in figure A-2. The hingeline was straight and located in the wing reference plane at its inboard end (0.087 b/2) and 2.261 cm (0.890 in.) above the wing reference plane at the wingtip. The airfoil thickness distribution (table A-1) and the trailing-edge control surface location and available deflections were identical to those of the flat wing.

CAMBERED-TWISTED WING

The mean surface of the cambered-twisted wing was generated by superimposing a camber on the twisted-wing definition but keeping the coordinates of the leading edge and trailing edge of the cambered-twisted wing the same as those of the twisted wing.

Table A-1.—Wing Half-Thickness Distribution, Percent Chord

x/c, percent chord	0 b/2	0.09 b/2	0.20 b/2	0.35 b/2	0.50 b/2	0.65 b/2	0.80 b/2	0.93 b/2	1.00 b/2
Flat wing with rounded leading edge, twisted wing, and cambered-twisted wing									
.0000	.0000	.0000	.0000	.0000	.0000	.0000	.0000	.0000	.0000
.1250	.3359	.3359	.3359	.3359	.3360	.3360	.3360	.3362	.3364
.2500	.4506	.4506	.4506	.4506	.4507	.4507	.4508	.4509	.4512
.5000	.6064	.6064	.6064	.6064	.6065	.6065	.6066	.6068	.6072
.7500	.7247	.7247	.7247	.7248	.7248	.7249	.7250	.7253	.7258
1.0000	.8182	.8182	.8182	.8183	.8183	.8184	.8185	.8188	.8194
1.5000	.9520	.9520	.9520	.9521	.9522	.9523	.9525	.9530	.9538
2.5000	1.1191	1.1191	1.1192	1.1192	1.1194	1.1195	1.1199	1.1206	1.1219
5.0000	1.3448	1.3448	1.3449	1.3450	1.3453	1.3456	1.3462	1.3475	1.3497
8.5000	1.4809	1.4809	1.4811	1.4813	1.4816	1.4822	1.4832	1.4855	1.4892
10.0000	1.5195	1.5196	1.5197	1.5200	1.5204	1.5210	1.5222	1.5250	1.5293
12.5000	1.5444	1.5445	1.5447	1.5450	1.5456	1.5463	1.5479	1.5514	1.5568
15.0000	1.5630	1.5631	1.5634	1.5638	1.5644	1.5654	1.5673	1.5715	1.5781
17.5000	1.5720	1.5722	1.5724	1.5729	1.5737	1.5748	1.5770	1.5821	1.5898
20.0000	1.5813	1.5815	1.5818	1.5823	1.5832	1.5845	1.5871	1.5929	1.6018
30.0000	1.6214	1.6217	1.6222	1.6230	1.6242	1.6262	1.6301	1.6389	1.6522
40.0000	1.6398	1.6402	1.6408	1.6419	1.6435	1.6462	1.6514	1.6630	1.6807
45.0000	1.6282	1.6286	1.6293	1.6305	1.6324	1.6354	1.6413	1.6544	1.6742
50.0000	1.5901	1.5906	1.5914	1.5927	1.5948	1.5981	1.6046	1.6192	1.6412
60.0000	1.4344	1.4350	1.4359	1.4375	1.4400	1.4440	1.4518	1.4692	1.4956
65.0000	1.3121	1.3127	1.3137	1.3155	1.3181	1.3225	1.3310	1.3498	1.3784
70.0000	1.1627	1.1634	1.1644	1.1663	1.1692	1.1739	1.1831	1.2034	1.2341
72.5000	1.0792	1.0799	1.0810	1.0830	1.0860	1.0908	1.1003	1.1213	1.1532
75.0000	.9921	.9928	.9940	.9960	.9991	1.0041	1.0139	1.0357	1.0686
77.5000	.9006	.9013	.9025	.9046	.9078	.9129	.9231	.9456	.9796
80.0000	.8069	.8077	.8089	.8111	.8143	.8197	.8302	.8534	.8885
85.0000	.6132	.6140	.6153	.6176	.6211	.6268	.6379	.6626	.6999
90.0000	.4156	.4165	.4178	.4203	.4240	.4300	.4418	.4679	.5074
95.0000	.2153	.2162	.2177	.2202	.2241	.2305	.2430	.2706	.3122
100.0000	.0113	.0123	.0138	.0165	.0206	.0273	.0405	.0695	.1134
Sharp leading edge									
.0000	.0000	.0000	.0000	.0000	.0000	.0000	.0000	.0000	.0000
.1250	.3359	.3359	.0293	.0307	.0329	.0364	.0433	.0585	.0815
.2500	.4506	.4506	.0557	.0580	.0614	.0670	.0781	.1024	.1392
.5000	.6064	.6064	.0998	.1021	.1055	.1111	.1222	.1465	.1833
.7500	.7247	.7247	.1439	.1462	.1496	.1552	.1663	.1906	.2274
1.0000	.8182	.8182	.1880	.1903	.1937	.1993	.2103	.2347	.2715
1.5000	.9520	.9520	.2761	.2784	.2818	.2875	.2985	.3229	.3596
2.5000	1.1191	1.1191	.4524	.4547	.4581	.4638	.4748	.4992	.5359
5.0000	1.3448	1.3448	.8933	.8956	.8990	.9046	.9156	.9400	.9768
8.5000	1.4809	1.4809	1.3413	1.3429	1.3453	1.3493	1.3570	1.3741	1.4001
10.0000	1.5195	1.5196	1.4547	1.4559	1.4578	1.4609	1.4669	1.4803	1.5007
12.5000	1.5444	1.5445	1.5203	1.5210	1.5221	1.5238	1.5272	1.5347	1.5461
15.0000	1.5630	1.5631	1.5634	1.5638	1.5644	1.5654	1.5673	1.5715	1.5781

The camber is defined analytically in two parts: a typical cruise airfoil (basic) camber; and, an estimate of the aeroelastic deformation at a moderate positive angle of attack. The aeroelastic deformation was based on calculations – using a typical configuration – of deformation under load. This definition was modified slightly to provide zero camber at the model centerline so this wing would fit on the existing model body. This was achieved by using a factor k (fig. A-3) on the basic camber term, which provides a transition from no camber at the model centerline to the definition camber at 0.25 b/2. The defined wing is smoother than indicated in this figure as section geometry was directly calculated at only those sections marked in figure A-3. The full equation for the camber is:

$$\frac{z}{c} = \left(\frac{z}{c}\right)_{Basic} + \left(\frac{z}{c}\right)_{Aero}$$

$$\left(\frac{z}{c}\right)_{Basic} = k\left(\frac{4.0}{3.0}\right)\left(0.078 + \frac{\alpha_{sec}}{57.3}\right)\left(\frac{x}{c}\right)\left(\frac{x}{c} - 1.0\right)\left(\frac{x}{c} - 0.75 - \frac{1.0}{4.0}\left(\frac{2y}{b}\right)\right)$$

$$k = \left(\frac{2y}{b}\right)\left(1.0 + 12.0\left(\frac{2y}{b}\right)\right) \qquad \text{for } \left(\frac{2y}{b}\right) \leq 0.25$$

$$k = 1.0 \qquad \text{for } \left(\frac{2y}{b}\right) \geq 0.25$$

$$\left(\frac{z}{c}\right)_{Aero} = -\frac{57.3}{3.0}\left(\frac{9.0}{4.0}\right)\left(\frac{2y}{b}\right)\left(1.0 - 0.75\left(\frac{2y}{b}\right)^2\right)\left(\sec\left(\frac{3.0}{57.3}\right) - \sec\left(\frac{(3.0)\left|1.0 - 2.0\left(\frac{x}{c}\right)\right|}{57.3}\right)\right)$$

The resulting nondimensional camber is shown in table A-2. The camber at the tip is approximately a 6° arc of a circle with the leading and trailing edges up. Sections at the root, midspan, and tip (fig. A-3) show not only the camber but the position of the sections of the cambered-twisted wing and the twisted wing relative to the wing reference plane (flat wing). The airfoil thickness distribution (table A-1) and the trailing-edge control surface location and available deflections were identical to those of the flat wing.

BODY

The body was circular in cross section and had a straight centerline. The body geometry is shown in figure A-1. The sting was an integral part of the model body.

RELATIVE WING AND BODY LOCATION

The wing reference plane was located 3.149 cm (1.240 in.) below and parallel to the body centerline (zero incidence). The apex (extension of the wing leading edge to the centerline) of the wing was located 33.496 cm (13.187 in.) aft of the model nose.

Table A-2.—Wing Section Camber Definition, Percent Chord

x/c, percent chord	0 b/2	0.09 b/2	0.20 b/2	0.35 b/2	0.50 b/2	0.65 b/2	0.80 b/2	0.93 b/2	1.00 b/2
.0000	.0000	.0000	.0000	.0000	.0000	.0000	.0000	.0000	.0000
.1250	−.0005	−.0014	.0015	.0000	−.0048	−.0076	−.0064	−.0042	−.0200
.2500	−.0005	−.0023	.0024	−.0017	−.0120	−.0177	−.0159	−.0118	−.0256
.5000	−.0005	−.0038	.0033	−.0067	−.0277	−.0394	−.0367	−.0297	−.0403
.7500	−.0005	−.0054	.0043	−.0115	−.0433	−.0608	−.0573	−.0473	−.0547
1.0000	−.0005	−.0071	.0054	−.0164	−.0591	−.0823	−.0780	−.0651	−.0695
1.5000	−.0005	−.0107	.0072	−.0263	−.0897	−.1240	−.1184	−.1003	−.0993
2.5000	−.0005	−.0174	.0080	−.0474	−.1480	−.2025	−.1946	−.1673	−.1567
5.0000	−.0005	−.0332	.0027	−.1035	−.2870	−.3878	−.3740	−.3233	−.2888
8.5000	−.0004	−.0577	−.0117	−.1876	−.4826	−.6449	−.6200	−.5312	−.4581
10.0000	−.0004	−.0695	−.0201	−.2257	−.5677	−.7552	−.7249	−.6184	−.5275
12.5000	−.0004	−.0910	−.0378	−.2922	−.7102	−.9377	−.8979	−.7613	−.6407
15.0000	−.0004	−.1139	−.0607	−.3624	−.8510	−1.1147	−1.0654	−.8991	−.7497
17.5000	−.0004	−.1375	−.0892	−.4359	−.9869	−1.2823	−1.2239	−1.0296	−.8530
20.0000	−.0004	−.1613	−.1229	−.5115	−1.1162	−1.4385	−1.3716	−1.1511	−.9493
30.0000	−.0004	−.2542	−.2941	−.8168	−1.5559	−1.9432	−1.8468	−1.5368	−1.2525
40.0000	−.0003	−.3359	−.4894	−1.0939	−1.8638	−2.2613	−2.1419	−1.7666	−1.4261
45.0000	−.0003	−.3695	−.5830	−1.2098	−1.9658	−2.3531	−2.2248	−1.8263	−1.4670
50.0000	−.0003	−.3968	−.6677	−1.3048	−2.0313	−2.4002	−2.2652	−1.8504	−1.4791
60.0000	−.0002	−.4273	−.7928	−1.4143	−2.0430	−2.3551	−2.2147	−1.7922	−1.4189
65.0000	−.0002	−.4275	−.8242	−1.4182	−1.9819	−2.2577	−2.1195	−1.7074	−1.3456
70.0000	−.0002	−.4154	−.8280	−1.3806	−1.8708	−2.1068	−1.9746	−1.5836	−1.2424
72.5000	−.0001	−.4041	−.8179	−1.3444	−1.7955	−2.0108	−1.8831	−1.5068	−1.1796
75.0000	−.0001	−.3892	−.7990	−1.2959	−1.7067	−1.9008	−1.7787	−1.4201	−1.1093
77.5000	−.0001	−.3704	−.7707	−1.2344	−1.6039	−1.7768	−1.6613	−1.3235	−1.0315
80.0000	−0001	−.3476	−.7324	−1.1593	−1.4870	−1.6386	−1.5308	−1.2169	−.9464
85.0000	−.0001	−.2893	−.6236	−.9864	−1.2095	−1.3190	−1.2304	−.9737	−.7541
90.0000	−.0001	−.2127	−.4683	−.7126	−.8714	−.9409	−.8762	−.6903	−.5324
95.0000	−.0000	−.1166	−.2622	−.3928	−.4697	−.5021	−.4668	−.3661	−.2811
100.0000	.0000	.0000	.0000	.0000	.0000	.0000	.0000	.0000	.0000

WING FIN

The wing fin is a 3-percent biconvex airfoil placed streamwise and perpendicular to the wing reference plane on the upper surface of the cambered-twisted wing at 0.725 semispan. The dimensions of the fin and its relationship to the wing are shown in figure A-4. To obtain configurations with the outboard trailing-edge control surface deflected, the fin is extended down to touch the top of the control surface. (See fig. A-4.)

PRESSURE ORIFICE LOCATIONS

All pressure orifices were located on the left side of the model and distributed as shown in figure A-5 and tables A-3 and A-4. The flat wing with rounded leading edge, the twisted wing, and the cambered-twisted wing each had 214 orifices distributed in streamwise pressure stations of 31 (or 30) orifices at each of seven spanwise locations. One of these orifices was located at the leading edge; the remainder were distributed so that upper- and lower-surface orifices were located at the same chordwise locations. The orifice locations on the sharp leading edge were identical except for the omission of the leading-edge orifice at each spanwise station. The 83 orifices on the body were located at 15 stations along the length of the model. At each station, orifices were located at angles of 0^0, 45^0, 90^0, 135^0, and 180^0 measured from the top of the body. In the area of the wing-body intersection, the orifices that are nominally identified as being at 135^0 and 180^0 were located on the wing lower surface at the same lateral location as the orifices at 45^0 and 0^0, respectively. Eight additional orifices were placed on the body, close to the juncture of the body with the wing upper surface.

DESIGN AND CONSTRUCTION

The objectives of this study dictated that the contours and physical characteristics of the flat wing, the twisted wing, and the cambered-twisted wing be as nearly identical as possible. The model was constructed of steel to minimize aeroelastic deflections and to provide strength for testing to a Mach number of 3.0. The aft body was flared approximately 4^0 from 194.310 cm (76.500 in.) aft of the nose to provide the required safety factor on predicted loads (fig. A-1). The model size was selected as the best compromise between minimizing potential tunnel blockage and providing adequate room to install orifices in the model.

A computerized lofting program was used to provide the wing definition. This definition was then used to machine the model components using numerically controlled machines. The tolerance on the contour was +0.1524, −0.0 mm (+0.006, −0.0 in.). The leading- and trailing-edge control surfaces were cut from the wings after they had been machined to final contour. A cut along the 15-percent chord line of the twisted wing removed enough material to simulate the elastic characteristics of the flat wing (fig. A-6). As a result of the previous tests it was determined that it was not necessary to remove this material on the cambered-twisted wing as the wings were very rigid. Fixed angle brackets (arranged as shown in fig. A-6) were used to obtain the required control surface deflections with all pivot points located midway between the upper and lower surfaces at the hingelines. The brackets were also machined on numerically controlled machines. The same sets of trailing-edge brackets were used on all three wings, and the same sets of leading-edge brackets were used for both the rounded and sharp leading edges.

Table A-3.—Wing Pressure Orifice Locations, Percent Local Chord

(a) Section at $0.09\frac{b}{2}$, chord = 102.89 cm

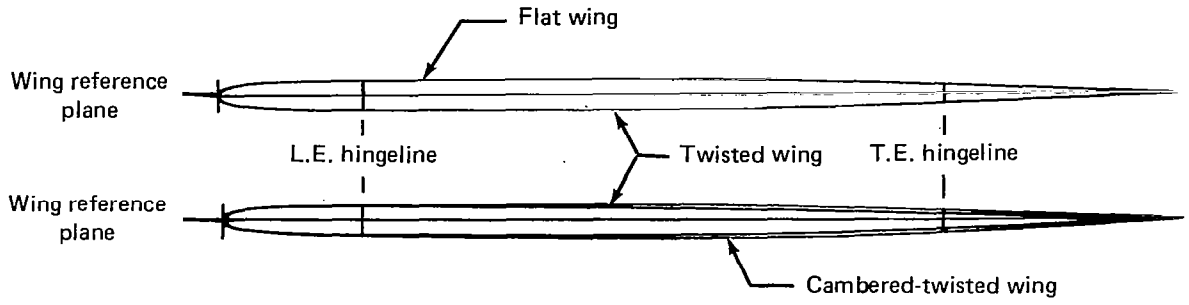

Nominal	Flat wing, $\alpha_{sec} = 0.0°$				Twisted wing, $\alpha_{sec} = -0.01°$		Cambered-twisted wing, $\alpha_{sec} = -0.01°$	
	Rounded leading edge		Sharp leading edge		Rounded leading edge		Rounded leading edge	
	Upper surface	Lower surface	Upper surface	Lower surface	Upper surface	Lower surface	Upper surface	Lower surface
0.00	0.00		—	—	0.00		0.00	
2.50	2.45	2.59	2.61	2.54	2.26	2.26	2.58	2.51
5.00	4.95	5.07	5.06	5.03	4.76	4.76	5.10	5.04
8.50	8.45	8.53	8.59	8.58	8.40	8.26	8.64	8.56
11.30	—	—	—	11.31	—	—	—	—
12.25	—	—	—	—	12.23	12.27	—	—
12.50	12.45	12.55	12.58	—	—	—	12.63	12.54
17.50	17.49	17.62			17.59	17.66	17.64	17.55
20.00	19.94	20.08			20.03	20.03	20.14	20.00
30.00	29.92	30.09			29.98	29.89	30.14	30.00
45.00	45.00	45.07			44.96	44.89	45.12	45.03
60.00	59.98	60.08			60.01	59.97	60.11	60.00
70.00	70.03	70.13			70.05	69.95	70.09	70.04
72.50	72.55	72.60			72.58	72.51	72.62	72.54
77.50	77.53	77.62			77.56	77.51	77.63	77.52
85.00	85.11	85.14			85.03	85.00	85.12	85.04
90.00	90.10	90.10			90.04	89.98	90.12	90.00
95.00	95.09	95.05			94.96	94.98	95.10	95.03

Table A-3.—(Continued)

(b) Section at $0.20\frac{b}{2}$, chord = 91.80 cm

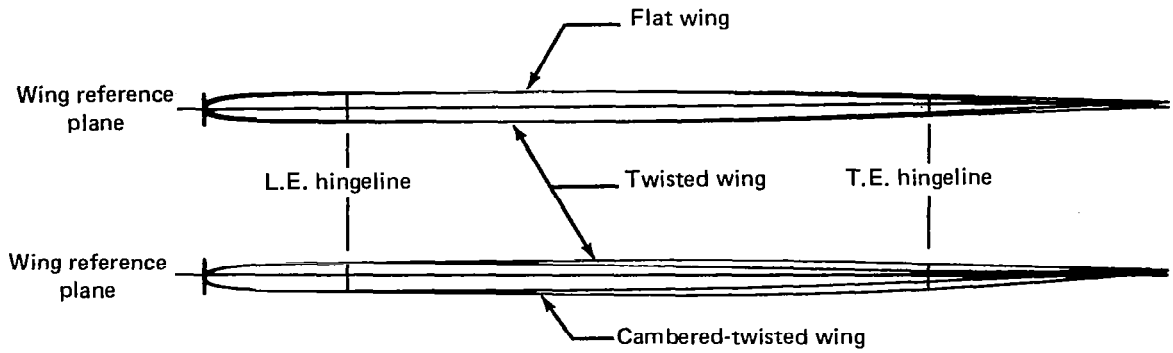

Nominal	Flat wing, $\alpha_{sec} = 0.0°$				Twisted wing, $\alpha_{sec} = -0.47°$		Cambered-twisted wing, $\alpha_{sec} = -0.47°$	
	Rounded leading edge		Sharp leading edge		Rounded leading edge		Rounded leading edge	
	Upper surface	Lower surface	Upper surface	Lower surface	Upper surface	Lower surface	Upper surface	Lower surface
0.00	0.00		–	–	0.00		0.00	
2.50	2.59	2.69	2.62	2.65	2.52	2.42	2.63	2.59
5.00	5.05	5.00	5.14	5.14	5.00	4.93	5.09	5.05
8.50	8.54	8.59	8.67	8.62	8.52	8.40	8.61	8.64
11.40	–	–	–	11.37	–	–	–	–
12.50	12.54	12.49	12.63	–	12.53	12.42	12.51	12.62
17.50	17.63	17.61			17.65	17.52	17.59	17.63
20.00	20.08	20.07			20.00	19.90	19.95	20.05
30.00	30.04	30.09			30.02	29.89	30.05	29.97
45.00	45.08	45.09			45.03	44.92	45.04	45.01
60.00	60.02	60.13			60.03	59.91	60.02	60.06
70.00	70.11	70.13			70.06	69.96	70.03	70.01
72.50	72.63	72.61			72.55	72.50	72.59	72.67
77.50	77.59	77.65			77.59	77.52	77.53	77.57
85.00	85.07	85.13			85.02	85.00	85.09	85.10
90.00	90.14	90.11			90.07	89.97	90.04	89.98
95.00	95.14	95.10			95.05	95.08	95.06	94.98

Table A-3.—(Continued)

(c) Section at $0.35\frac{b}{2}$, chord = 76.69 cm

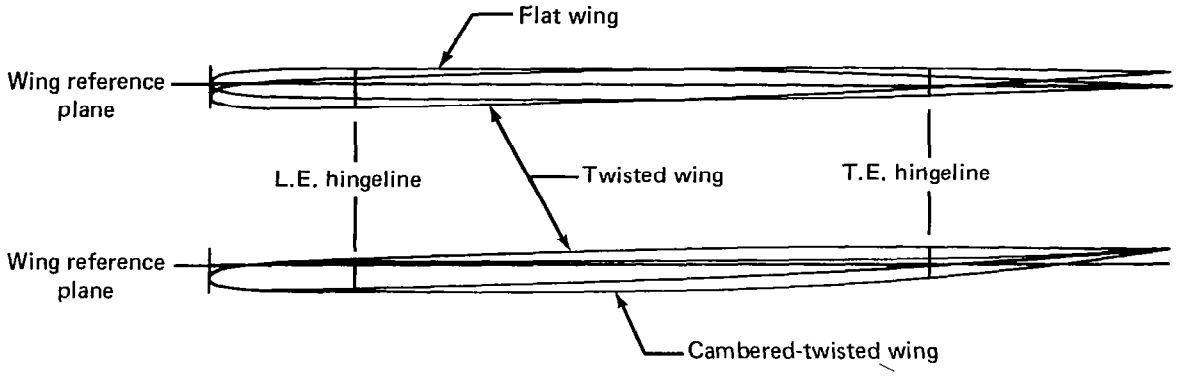

Nominal	Flat wing, $\alpha_{sec} = 0.0°$				Twisted wing, $\alpha_{sec} = -1.70°$		Cambered-twisted wing, $\alpha_{sec} = -1.70°$	
	Rounded leading edge		Sharp leading edge		Rounded leading edge		Rounded leading edge	
	Upper surface	Lower surface	Upper surface	Lower surface	Upper surface	Lower surface	Upper surface	Lower surface
0.00	0.00		–	–	0.00		0.00	
2.50	2.45	2.59	2.59	2.58	2.39	2.33	2.76	2.60
5.00	4.93	5.07	5.11	5.04	5.12	4.78	5.05	5.10
8.50	8.60	8.54	8.65	8.63	8.49	8.32	8.68	8.70
10.50	–	–	–	10.46	–	–	–	–
11.00	–	11.03	–	–	–	–	–	–
12.50	12.37	–	12.57	–	12.50	12.33	12.59	12.68
17.50	17.64	17.63			17.54	17.53	17.64	17.62
20.00	20.00	20.09			19.94	19.84	20.03	20.07
30.00	30.01	30.10			29.88	29.87	30.00	29.93
45.00	44.99	45.09			44.96	44.79	45.00	45.13
60.00	60.03	60.08			59.97	59.89	60.00	60.10
70.00	70.07	70.08			70.03	69.90	70.04	70.03
72.50	72.55	72.58			72.56	72.44	72.61	72.52
77.50	77.60	77.61			77.54	77.51	77.50	77.60
85.00	85.11	85.14			85.08	84.96	85.09	84.93
90.00	90.06	90.09			89.89	89.89	89.98	90.04
95.00	95.07	95.09			94.95	94.86	94.98	95.10

Table A-3.–(Continued)

(d) Section at 0.50 $\frac{b}{2}$, chord = 61.57 cm

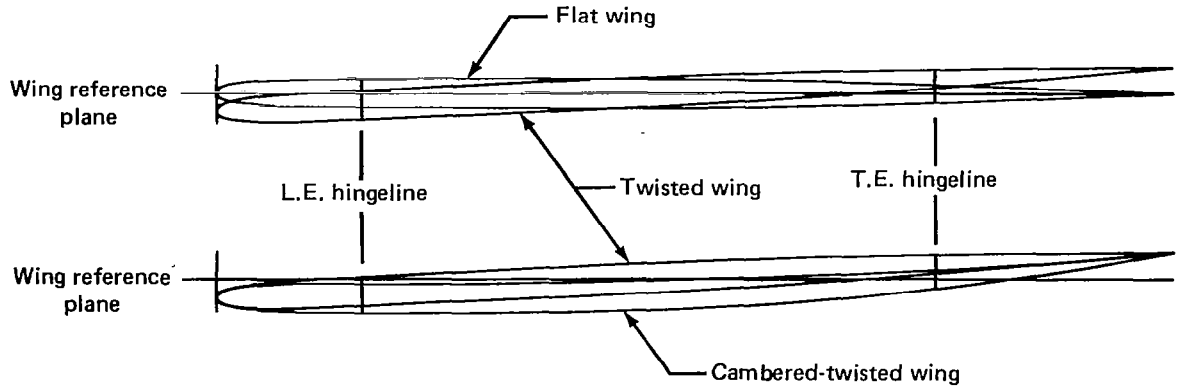

Nominal	Flat wing, $\alpha_{sec} = 0.0°$				Twisted wing, $\alpha_{sec} = -2.85°$		Cambered-twisted wing, $\alpha_{sec} = -2.85°$	
	Rounded leading edge		Sharp leading edge		Rounded leading edge		Rounded leading edge	
	Upper surface	Lower surface	Upper surface	Lower surface	Upper surface	Lower surface	Upper surface	Lower surface
0.00	0.00		–	–	0.00		0.00	
2.50	2.47	2.53	2.69	2.60	2.44	2.38	2.78	2.62
5.00	4.99	4.95	5.13	5.06	4.92	4.80	5.13	5.15
8.50	8.48	8.38	8.66	8.61	8.46	8.38	8.64	8.56
10.10	–	–	–	10.14	–	–	–	–
11.10	–	11.08	–	–	–	–	–	–
12.50	12.39	–	12.61	–	12.50	12.31	12.71	12.55
17.50	17.64	17.52			17.54	17.24	17.71	17.44
20.00	19.98	19.97			19.92	19.83	20.15	19.89
30.00	30.07	30.06			29.91	29.85	30.04	29.72
45.00	44.98	45.06			45.00	44.85	44.95	44.97
60.00	59.97	60.00			59.95	59.92	59.96	59.94
70.00	70.07	70.10			70.03	69.88	69.93	69.86
72.50	72.65	72.61			72.56	72.44	72.53	72.34
77.50	77.66	77.65			77.61	77.43	77.58	77.43
85.00	85.19	85.18			84.85	84.90	84.96	84.92
90.00	90.22	90.12			89.93	89.93	89.94	89.91
95.00	95.05	94.94			94.88	94.93	94.98	94.88

Table A-3.—(Continued)

(e) Section at $0.65\frac{b}{2}$, chord = 46.46 cm

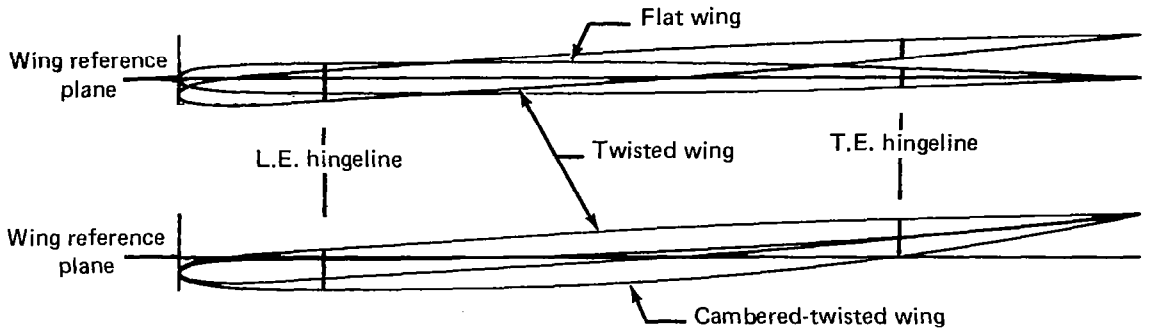

Nominal	Flat wing, $\alpha_{sec} = 0.0°$				Twisted wing, $\alpha_{sec} = -3.59°$		Cambered-twisted wing, $\alpha_{sec} = -3.59°$	
	Rounded leading edge		Sharp leading edge		Rounded leading edge		Rounded leading edge	
	Upper surface	Lower surface	Upper surface	Lower surface	Upper surface	Lower surface	Upper surface	Lower surface
0.00	0.00		–	–	0.00		0.00	
2.50	2.56	2.66	2.49	2.38	2.18	2.49	2.76	2.79
5.00	5.06	5.12	4.94	4.95	4.76	5.01	5.35	5.40
8.50	8.55	8.55	8.46	8.40	8.32	8.45	8.85	8.74
12.20	–	–	12.12	–	12.21	–	–	–
12.60	12.57	–	–	–	–	–	12.71	12.77
17.50	17.60	17.65			17.24	17.44	17.74	17.58
20.00	20.17	20.11			19.70	19.88	20.19	19.96
30.00	30.05	30.11			30.26	29.73	30.13	29.85
45.00	45.16	45.23			44.75	44.89	45.03	44.75
60.00	60.13	60.13			59.81	59.87	60.02	59.99
70.00	69.89	70.12			69.92	69.90	70.09	69.88
72.50	72.59	72.69			72.38	72.49	72.83	72.15
77.50	77.74	77.76			77.22	77.49	77.56	77.43
85.00	85.25	85.32			84.79	84.93	84.93	84.76
90.00	90.22	90.21			89.70	89.92	89.95	89.98
95.00	95.13	95.27			95.12	94.86	94.97	94.98

Table A-3.—(Continued)

(f) Section at $0.80\frac{b}{2}$, chord = 31.35 cm

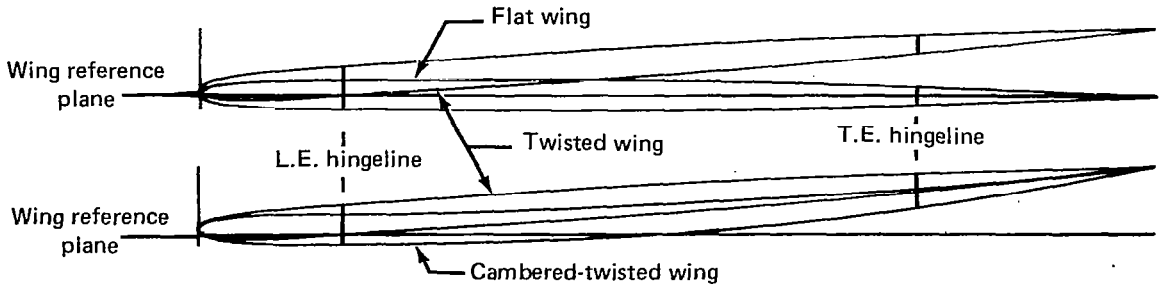

Nominal	Flat wing, $\alpha_{sec} = 0.0°$				Twisted wing, $\alpha_{sec} = -3.84°$		Cambered-twisted wing, $\alpha_{sec} = -3.84°$	
	Rounded leading edge		Sharp leading edge		Rounded leading edge		Rounded leading edge	
	Upper surface	Lower surface	Upper surface	Lower surface	Upper surface	Lower surface	Upper surface	Lower surface
0.00	0.00		–	–	0.00		0.00	
2.50	2.55	2.47	2.50	2.46	2.33	2.43	2.76	2.62
5.00	5.01	5.02	5.01	4.93	4.86	4.74	5.27	5.21
8.50	8.55	8.59	8.58	8.41	8.32	–	8.78	8.54
12.50	12.50	–	12.58	–	12.47	12.43	12.69	12.58
17.50	17.53	17.57			17.36	17.47	17.83	17.34
20.00	20.16	20.13			19.79	19.82	20.11	19.79
30.00	30.00	30.11			29.83	29.83	30.15	29.48
45.00	44.91	45.15			44.81	44.91	44.81	44.75
60.00	59.94	60.10			59.80	59.92	59.84	59.79
70.00	70.06	70.11			69.89	69.87	69.77	69.94
72.50	72.61	72.60			72.22	72.39	72.50	72.33
77.50	77.73	77.72			77.29	77.41	77.22	77.40
85.00	85.25	85.18			84.80	84.95	84.92	84.92
90.00	90.20	90.34			90.62	90.03	90.19	90.09
95.00	95.41	95.49			95.71	95.00	95.05	94.94

Table A-3.—(Concluded)

(g) Section at $0.93\frac{b}{2}$, chord = 18.25 cm

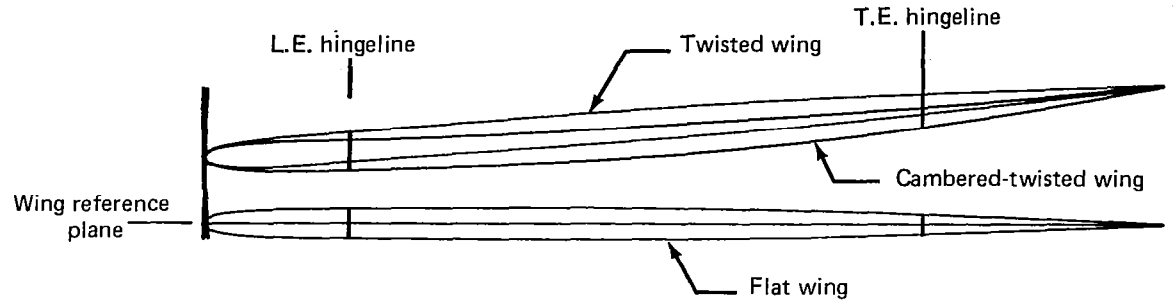

Nominal	Flat wing, $\alpha_{sec} = 0.0°$				Twisted wing, $\alpha_{sec} = -4.14°$		Cambered-twisted wing, $\alpha_{sec} = -4.14°$	
	Rounded leading edge		Sharp leading edge		Rounded leading edge		Rounded leading edge	
	Upper surface	Lower surface	Upper surface	Lower surface	Upper surface	Lower surface	Upper surface	Lower surface
0.00	0.00		—	—	0.00		0.00	
2.51	1.70	1.81	2.12	1.86	1.74	2.59	2.77	2.26
5.00	4.38	4.68	4.72	4.52	4.41	4.65	5.11	4.79
8.50	7.89	8.24	8.21	8.06	7.92	8.23	8.64	8.13
11.59	—	—	—	—	11.59	—	—	—
12.25	12.33	—	12.19	—	—	—	12.64	12.16
17.50	17.36	16.60			16.60	17.49	18.03	16.83
20.00	19.78	19.81			19.58	19.96	19.94	19.44
30.00	29.67	29.00			29.17	29.62	30.22	28.66
45.00	44.70	44.80			44.12	44.44	44.33	44.77
60.00	59.68	59.47			59.18	59.71	59.47	59.38
70.00	69.69	70.33			68.99	69.31	69.10	70.07
72.50	72.15	71.89			71.59	72.01	71.78	72.74
77.50	77.38	77.31			76.80	77.12	76.49	77.36
85.00	84.62	84.90			84.54	84.82	84.93	85.29
90.00	89.51	89.81			89.21	89.74	90.72	90.35
95.00	94.46	94.68			94.41	94.56	95.26	94.87

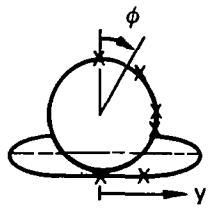

Table A-4.—Body Pressure Orifice Locations

	x/L, percent body length														
Nominal locations	4.5	7.5	11.0	14.5	21.8	25.0	33.0	39.0	50.0	55.0	60.0	64.0	70.0	75.5	80.0
$\phi = 0.0°$	0.0	0.0	0.0	0.0	0.0	0.0	0.0	0.0	0.0*	0.0*	0.0*	0.0	0.0	0.0	0.0
$\phi = 45.0°$	44.3	44.3	44.5	44.7	44.4	44.8	45.0	44.8	45.0	44.8	44.8	45.0	44.8	45.0	44.8
$\phi = 90.0°$	90.0	89.9	90.5	90.3	90.4	89.9	90.1	90.2	90.2	90.0	89.9	89.9	89.8	90.1	89.8
$\phi \approx 110.0°$	———	———	———	———	110.2	110.0	110.1	110.1	110.2	116.8	119.9	124.2	———	———	———
Body, $\phi = 135.0°$	136.1	135.3	135.0	135.2									134.6	134.5	134.8
Flat wing, y = 3.094 cm					3.025	3.028	3.028	3.056	3.071	3.056	3.043	3.045			
Twisted wing, y = 3.094 cm					3.132	3.106	3.048	3.048	3.005	2.926	3.094	3.094			
Cambered-twisted wing, y = 3.094 cm					3.040	3.056	3.075	3.072	3.079	3.067	3.084	3.069			
Body, $\phi = 180.0°$	180.0	180.0	180.0	180.0						180.0*	180.0*	180.0	180.0	180.0	180.0
Flat wing, y = 0.0 cm					−.018	−.030	−.064	.081	−.048						
Twisted wing, y = 0.0 cm					.020	−.008	−.041	−.043	−.056						
Cambered-twisted wing, y = 0.0 cm					−.046	−.060	−.027	.002	−.032						

*For the first 149 runs of the first test in the BTWT, pressure readings at these orifices did not always stabilize.

Pressure tubing used in this model was 1.016 mm (0.040 in.) o.d. Monel with a 0.1524 mm (0.006 in.) wall thickness. The major channels for wing pressure tubing were machined into the surface. The detailed grooves required to route tubing from the orifices to these channels were cut by hand. The pressure orifices were installed normal to and flush with the local surface. After installation of the pressure tubing, the grooves were filled with solder and brought back to contour by hand-filing to match templates prepared by numerically controlled machining.

Quick disconnects were used at the wing-body junction to reduce the time required for installing a different wing. Unfortunately, by the time the cambered-twisted wing was installed in the test section, one quick-disconnect block had become worn out due to the two previous tests and model checkout. The connection did not seal properly and measurements at a series of orifices (x/c from 0.125 through 0.600) on the lower surface at 0.80 b/2 were not sufficiently accurate to be used. Data values to be used in the integration were obtained by linear spanwise interpolation between adjacent sections.

The tubing for body pressure orifices was run through the hollow center of the model body rather than running it in grooves in the outside contour. Tubing from all the orifices was routed through the hollow body to the scanivalves located in the body nose. Wiring from the scanivalves was routed through the body to the sting.

The nose portion of the body was removable to provide access to the fifteen 24-position scanivalves. Figure A-1 shows the aft body location of the strain gages that were used to measure normal force and pitching moment.

PRESSURE INSTRUMENTATION

The model was instrumented with fifteen 24-position scanivalves. Each scanivalve contained a 103.42-kN/m^2 (15-psi) differential Statham, variable resistance, unbonded strain gage transducer. These transducers are calibrated against a high accuracy standard and, if placed in a temperature-controlled environment, will read within an accuracy of 0.1 percent of full scale. The transducers were located inside the model and subjected to large temperature excursions. During testing in the Boeing Transonic Wind Tunnel (BTWT), temperatures recorded at the scanivalves indicated that the accuracy of the readout was 0.75 percent of full-scale capability based on the calibration data. For tests in the 9- by 7-ft supersonic leg of the NASA Ames Unitary Wind Tunnel, the accuracy of pressure measurements was better than ± 0.3 percent, based on the maximum temperature measured in the test section.

During the first test in the BTWT (NAS1-12875), two problems were encountered. For the first 149 runs, the data filter for one of the scanivalves was inadvertently set at too low of a cutoff frequency. This caused a lag that affected five body pressure measurements, which produced a maximum error of approximately 0.684 kN/m^2 (0.1 psi) at an angle of attack of 16° and M = 0.95. Table A-4 identifies the specific data affected. During the first half (approximately) of the test, the scanivalve that recorded lower surface pressures between the hingelines for the sections at 2y/b = 0.09, 0.20, 0.35, and 0.50 was intermittent at an angle of attack of 16°. This problem was eventually traced to an electrical problem in the strut. Rather than sacrifice all of these data, the incorrect measurements were replaced by extrapolating the data from angles of attack of 12° and 14°.

In the second test in the BTWT (NAS1-14962), damage to one of the quick disconnects for the wing caused the loss of measurements at a series of orifices (x/c from 0.125 through 0.600) on the lower surface at 0.80 b/2. Replacement values were obtained by a linear-spanwise interpolation between the adjacent sections.

WIND TUNNEL FACILITIES AND CAPABILITIES

The majority of testing (NASA contracts NAS1-12875 and NAS1-14962) of this model was conducted in the Boeing Transonic Wind Tunnel (BTWT). There was also limited testing (NASA contract NAS1-14141) of the flat and twisted wings in the 9- by 7-ft supersonic leg of the NASA Ames Unitary Wind Tunnel. These two facilities are described in some detail.

BOEING TRANSONIC WIND TUNNEL (BTWT)

The BTWT is a continuous-flow, closed-circuit, single-return facility with an operating range of Mach number from 0.0 to nearly 1.1. The test section is 2.438 by 3.658 by 4.420 m (8 by 12 by 14.5 ft) with 11.0 percent of the wall area in slots.

The tunnel layout is shown in figure A-7. The tunnel stagnation pressure is atmospheric with a total temperature range of 300 K to 356 K (540° to 640° R). The variation with Mach number of Reynolds number based on the mean aerodynamic chord (M.A.C.) of this model is shown in figure A-8., which also shows the variation of dynamic pressure with Mach number. The 26 856-kW (36 000-hp) wound-rotor induction motor in tandem with a 13 428-kW (18 000-hp) synchronous motor provides the power to drive a 7.315-m (24-ft) diameter fan up to a maximum speed of 470 rpm. The fan is made up of a 5.486-m (18-ft) diameter hub with 72 fixed-pitch fiberglass blades 0.914 m (36 in.) long in two stages and directs circuit air through two stages of 67 hollow steel stators.

Data System

The BTWT data system provides the capabilities of real-time test data acquisition, feedback control computation, and display. The data system consists of an Astrodata acquisition subsystem and a computing subsystem that uses a Xerox data system (XDS 9300) digital computer. The Astrodata system acquires signals from the sensors, conditions them, and passes them directly to the computer. Test data (averaged from as many as 256 samples per test point) are recorded on a rapid-access data drum. As final computations are performed, selected on-line displays are provided on analog X-Y plotters and teletypewriters. Real-time computations and displays are performed every 200 milliseconds for control and test monitoring functions. Any test data may be retrieved from rapid-access drum storage and displayed on an oscilloscope. On-line programs also provide for the preparation of magnetic tapes for plotting or interfacing with off-line programs. Figure A-9 is a schematic of the data acquisition and reduction system.

Mach Number

Mach number in the BTWT is referenced to the horizontal and lateral center of the test section at tunnel station 1000, which was the pitch point of this model (40-percent M.A.C.).

The pressures used in determining the Mach number, p_s, and p_t are measured through permanently positioned sensors. Static pressure p_s is measured by a 103.42-kN/m^2 (15-psi) absolute transducer. A 103.42-kN/m^2 (15-psi) differential transducer is used to obtain total pressure by measuring (p_t-p_s). These transducers are temperature compensated in addition to being in a $\pm 1.11^0$ C ($\pm 2^0$ F) environment. Transducer performance is checked periodically, and both the static and differential transducers have shown a maximum deviation of ± 0.02 percent of full scale.

The static pressure tap is located out of the test section above the ceiling in the pressure cap plenum. A correction is made to adjust this static pressure reading to the measured test-section-centerline static pressure determined during calibrations at station 1000. The tunnel total pressure is obtained from a total pressure probe mounted near the tunnel ceiling in the bellmouth throat (fig. A-7).

Signals from the pressure sensors are fed to the XDS 9300 computer. The XDS system computes and updates the Mach display five times per second. Accounting for the entire system, calculated Mach number is accurate within ± 0.002. Data are recorded only when the tunnel is within a preselected Mach tolerance. For this test, a tolerance of ± 0.003 was used.

Dynamic Pressure

The dynamic pressure q is computed from the Mach number and the corrected static pressure. The estimated tolerance on dynamic pressure is ± 95.8 N/m^2 (± 2.0 psf).

Angle of Attack

The angle of attack of the reference point (0.25 M.A.C. for this model) for a sting-mounted model is a combination of the input angle measured at the base of the sting and several incremental corrections. The input angle of attack is determined by an encoder mounted in the strut. This angle is accurate within $\pm 0.02^0$. This angle is then modified by the effects of sting deflection, up-flow, and wall corrections.

Sting deflections due to load were determined during the calibrations of the strain gages, which are mounted on the integral sting body of the model. These deflections are known within $\pm 0.02^0$. The corrections for sting deflection are based on the normal force and pitching moment loads obtained during wind-on data acquisition. The sting deflection was taken into account when setting test angles of attack, to minimize the variation in final angle of attack for the various model configurations. The strain gages attached to the sting body of this model have an estimated accuracy of ± 5 percent of full-scale reading. This means that the sting deflections based on maximum model loads were known within $\pm 0.11^0$.

During run 55 of the second test in the BTWT, the wiring for the pitching moment gage broke, affecting both the normal force and pitching moment measurements and, therefore, the calculation of sting deflection under load. For the remainder of that test, the model angle was set using the angle of attack as determined by the encoder for the most similar previously run configuration. After the test, the normal force and pitching moment obtained by integrating the pressure data were used to correct the final angle of attack. To verify this procedure, a comparison of these two methods was made using data obtained prior to run 55; the results matched within $\pm 0.01^0$.

Up-flow corrections were made based on data obtained from upright and inverted runs on a calibration model of similar span. These corrections were less than 0.2°. It is generally accepted that the up-flow values are known within ±0.05°.

A correction to model angle was made for the effect of lift interference for 11-percent slotted walls. The lift interference is a function of the ratio of model-to-test section size, test section shape, C_N, and wall geometry. For $C_N = 1.0$, this correction is on the order of −0.48°. Due to the limited amount of experimental substantiation, the wall correction could be in error by ±20 percent.

NASA AMES UNITARY WIND TUNNEL, 9- BY 7-FT SUPERSONIC LEG

The 9- by 7-ft supersonic leg of the NASA Ames Unitary Wind Tunnel is a continuous-flow, closed-return, variable-density facility with an operating range of Mach number from 1.54 to 2.50. (A schematic is shown in fig. A-10.) The tunnel is equipped with an asymmetrical sliding-block nozzle and a flexible upper plate; variation of the test section Mach number is achieved by translating, in the streamwise direction, the fixed-contour block that forms the floor of the nozzle. For this test, the Reynolds number was selected as 8.65 by 10^6 based on the mean aerodynamic chord ($\bar{c}$) of this model. The test section is 2.74 by 2.13 by 5.49 m (9 by 7 by 18 ft).

The tunnel air is driven by an 11-stage axial-flow compressor that is powered by four variable-speed, wound-rotor induction motors with a combined output of 134 280 kW (180 000 hp). Four 850 m^3 (30 000 ft^3) spherical storage tanks provide dry air for tunnel pressurization. The temperature is controlled by aftercooling.

Data System

The data acquisition system is comprised of a Beckman 210 analog-digital recorder and a minicomputer. Output from the Beckman 210 is converted to an acceptable format and transmitted by the minicomputer to an IBM 360 computer, which is located in the AMES Research Center central computer facility for the processing and preparation of final data. This flow is illustrated in figure A-11.

Angle of Attack

The angle of attack of the reference point (0.25 M.A.C. for this model) for a sting-mounted model is a combination of the input angle at the base of the sting and an increment due to sting deflection. The input angle of attack at the base of the sting is accurate within 0.02°.

Sting deflections due to load were determined during the calibration of the strain gages mounted on the integral sting body of the model. The corrections for sting deflection are based on the normal force and pitching moment loads obtained during wind-on data acquisition. The sting deflection was taken into account when setting test angles of attack to minimize the variation in final angle of attack for the various model configurations. Only a crude calibration of the normal force and pitching moment gages was obtained since the force and pitching moment measurements were used primarily for calculating sting deflection. Comparison with the integrated pressure results indicates that both force and moment measurements may be about 10 percent low, which could yield a maximum error in final angle of attack of 0.1°.

TESTS AND DATA ACQUISITION

BOEING TRANSONIC WIND TUNNEL (BTWT)

Tests

As previously stated, tests were conducted in the BTWT under two NASA contracts. Table A-5 shows the 54 configurations that were tested under contract NAS1-12875. The 12 configurations tested under contract NAS1-14962 are shown in table A-6. Two of the configurations were included in both tests to ensure that data from the two tests are consistent. Photographs of some of the configurations are shown in figures A-12 through A-15; a diagram of the model installation in the BTWT is shown in figure A-16.

Pressure and total force data were obtained at Mach numbers of 0.40, 0.85, 0.95, and 1.05 for all configurations and at Mach numbers of 0.70, 1.00, and 1.11 for selected configurations. Test angles of attack were from -8^{0} to $+16^{0}$ in 2^{0} increments, however, not all angles of attack were included for all configurations and/or Mach numbers. Tables A-5 and A-6 show the run numbers for each Mach number and configuration for which these data were obtained.

During the first test, wingtip deflection pictures were taken for representative configurations at three Mach numbers to evaluate the stiffness of the wing. These were compared to wind-off reference pictures to determine the relative deflection and twist. Configurations included the flat and twisted wings, and trailing-edge control surfaces deflected $+30.2^{0}$, 0.0^{0}, and -17.7^{0}. Whereas the tip did deflect (less than 2 cm), the change in incidence was negligible even at M = 1.05; and, due to model flexibility, no corrections to the data were required.

Data Repeatability

Comparisons of data from both tests (NASA CR-165701), show that the data are within the tolerances expected for repeat runs during a single test. Therefore, data from both tests are compared without regard to the test in which the data were obtained.

Data Acquisition and Initial Processing

The pressure data were recorded through the use of fifteen 24-position scanivalves located in the fore body of the model. Pressure transducers in the scanivalves measured the differential pressure between the local surface pressures and tunnel total pressure. Signals from the scanivalves, force and moment data, tunnel parameters, and model attitude angle were recorded on the Astrodata system and reduced using the XDS 9300 computer.

NASA AMES UNITARY WIND TUNNEL, 9- BY 7-FT SUPERSONIC LEG

Tests

Table A-7 lists the 13 configurations that were tested. Photographs of two of these are shown in figures A-17 and A-18; a diagram of the model installation in the test section is shown in figure A-19. Pressure and total force data were obtained at Mach numbers of 1.70, 2.10 and 2.50 for all configurations. Table A-7 shows the run numbers for each Mach number and configuration for which these data were obtained. Test angles of attack were from -8^{0} to $+14^{0}$ in 2^{0} increments and $+15^{0}$.

Table A-5.—Summary of Subsonic/Transonic Test Conditions by Run Number (NASA Contract NAS1-12875)

Leading-edge deflection, deg	Mach. no.	Trailing-edge deflection, deg																
		Full span									Outboard (inboard = 0.0)				Inboard (outboard = 0.0)			
		30.2	17.7	8.3	4.1	0.0	−4.1	−8.3	−17.7	−30.2	17.7	8.3	−8.3	−17.7	17.7	8.3	−8.3	−17.7
Flat wing, rounded leading edge, trip strip off																		
Full span=0.0	0.40					10												
	0.70					15												
	0.85					7												
	0.95					16												
	1.05					14												
	1.11					9												
Flat wing, rounded leading edge, trip strip on																		
Full span=0.0	0.40	37	32	46	48	21,269	55	78	66	75	280	275			252	259		
	0.70	34	29	43	50	23,263	57	80	63	72	277	271			248	255		
	0.85	36	31	45	52	25,267	59	82	65, 69	74	279	274			250	258		
	0.95	35	30	44	51	24,266	58	81	64, 68	73	278	273			249	257		
	1.00					268												
	1.05	33	28	42	49	22,264	56	79	62	71	276	272			247	256		
	1.11			40	47	20,262	54	77				270				254		
Inboard =0.0	0.40					223					215	209	196	202	246	241	235	229
Outboard=5.1	0.70					218					211	205	192	198	243	237	231	228
	0.85					221					214	208	195	201	245	240	233	227
	0.95					220					213	207	194	200	244	239	232	226
	1.05					219					212	206	193	199	242	238	230	224
	1.11					217					210	204	191	197		236		

Table A-5.—(Continued)

Leading-edge deflection, deg	Mach no.	Trailing-edge deflection, deg																
		Full span									Outboard (inboard = 0.0)				Inboard (outboard = 0.0)			
		30.2	17.7	8.3	4.1	0.0	−4.1	−8.3	−17.7	−30.2	17.7	8.3	−8.3	−17.7	17.7	8.3	−8.3	−17.7
Flat wing, rounded leading edge, trip strip on																		
Inboard =5.1 Outboard=0.0	0.40					319					286	313			329	324		
	0.70					315					283	311			326	321		
	0.85					318					285	312			328	323		
	0.95					317					284	310			327	322		
	1.05					316					282	308			325	320		
	1.11					314												
Full span=5.1	0.40		177	149	138	183		189	132									
	0.70		173	145	140	179		185	134									
	0.85		175	148	142	182		188	136									
	0.95		174	147	141	181		187	135									
	1.05		172	146	139	180		186	133									
	1.11			144	137	178		184	131									
Full span=12.8	0.40		118	115	109	98		85	126									
	0.70		121	112	105	100		87	128									
	0.85		123	114	108	102		89	130									
	0.95		122	113	107	101		88	129									
	1.05		120	111	106	99		86	127									
	1.11		116		104	97		84	124									

Table A-5.—(Concluded)

Leading-edge deflection, deg	Mach no.	Trailing-edge deflection, deg																
		Full span									Outboard (inboard = 0.0)				Inboard (outboard = 0.0)			
		30.2	17.7	8.3	4.1	0.0	−4.1	−8.3	−17.7	−30.2	17.7	8.3	−8.3	−17.7	17.7	8.3	−8.3	−17.7
Flat wing, sharp leading edge, trip strip on																		
Full span=0.0	0.40					368												
	0.70					366												
	0.85					372												
	0.95					374												
	1.00					373												
	1.05					367												
	1.11					365												
Flat wing, twisted trailing edge, rounded leading edge, trip strip on																		
Full span=0.0	0.40		352	347	342	337		358	363									
	0.70		349	344	339	333		354	360									
	0.85		351	346	341	336		356	362									
	0.95		350	345	340	335		357	361									
	1.05		348	343	338	334		353	359									
	1.11					332												
Twisted wing, rounded leading edge, trip strip on																		
Full span=0.0	0.40	427	422	416	411	450		435	442									
	0.70	424	419	413	408	445		432	439									
	0.85	426	421	415	410	449		434	441									
	0.95	425	420	414	409	447		433	440									
	1.00					448												
	1.05	423	418	412	407	446		431	438									
	1.10					444												

Table A-6.—Summary of Subsonic/Transonic Test Conditions by Run Number (NASA Contract NAS1-14962)

Mach number	Trailing-edge deflection, degrees			
	Full span		Outboard (inbd=0.0)	Inboard (outbd=0.0)
	0.0	8.3	8.3	8.3
Twisted wing				
0.40	15	25	30	20
0.70	14	24	29	19
0.85	13	23	28	18
0.95	12	22	27	17
1.00	11			
1.05	10	21	26	16
Cambered-twisted wing, fin off				
0.40	43	65	80	57
0.70	41			
0.85	40	62	78	59
0.95	39	64	79	58
1.00	38			
1.05	37	61	77	55
Cambered-twisted wing, fin on				
0.40	49	70	75	54
0.70	45			
0.85	48	68	73	52
0.95	47	69	74	53
1.00	46			
1.05	44	67	72	51

Table A-7.—Summary of Supersonic Test Conditions by Run Number. Reynolds Number = 8.65 x 10^6 (NASA Contract NAS1-14141)

Leading-edge deflection, deg	Mach no.	Trailing-edge deflection, deg							
		Full span				Outboard (inboard = 0.0)		Inboard (outboard = 0.0)	
		8.3	4.1	0.0	−4.1	8.3	4.1	8.3	4.1
Flat wing, rounded L.E.									
Full span = 0.0	1.543			19					
	1.70	26	37	20	44	23	40	30	34
	2.10	27	38	21	45	24	41	31	35
	2.50	28	39	22	46	25	42	32	36
Full span = 5.1	1.70			16					
	2.10			17					
	2.50			18					
Flat wing, sharp L.E.									
Full span = 0.0	1.70			51					
	2.10			52					
	2.50			53					
Full span = 5.1	1.70			48					
	2.10			49					
	2.50			50					
Twisted wing, rounded L.E.									
Full span = 0.0	1.60			1					
	1.70	11		3					
	1.90			4, 6					
	2.10	12		9					
	2.50	13		10					

Data Acquisition and Initial Processing

The pressure data were recorded through the use of fifteen 24-position scanivalves located in the fore body of the model. Pressure transducers in the scanivalves measured the differential pressure between the local surface pressures and a known reference pressure. Signals from the scanivalves, force and moment data, tunnel parameters, and model attitude angle were recorded on the Beckman 210 analog-digital recorder and reduced by the Ames staff.

TRIP STRIP

A trip strip of no. 60 carborundum grit was used throughout the tests with the exception of one series. On the body, the trip strip was 0.32 cm (0.125 in.) wide and placed 2.54 cm (1 in.) from the nose. On the wing, it was 0.32 cm (0.125 in.) wide from the side of body to the midspan control surface break (0.57 b/2), and tapered to 0.16 cm (0.0625 in.) wide at the wingtip. On the upper surface of the wing, the trip strip was placed at 15-percent chord; and, on the lower surface, it was placed just aft of the location of the leading-edge control surface brackets on the flat wing (see fig. A-6). Density of the grit was 4 to 5 grains per quarter-inch (6 to 8 grains per cm) of trip strip length.

FINAL DATA

Final data (pressure coefficients, tunnel parameters, and model attitude) were merged on magnetic tapes with appropriate configuration and test point identification for integration and plotting of these data.

A detailed description of the data editing and integration procedure are included in appendix B.

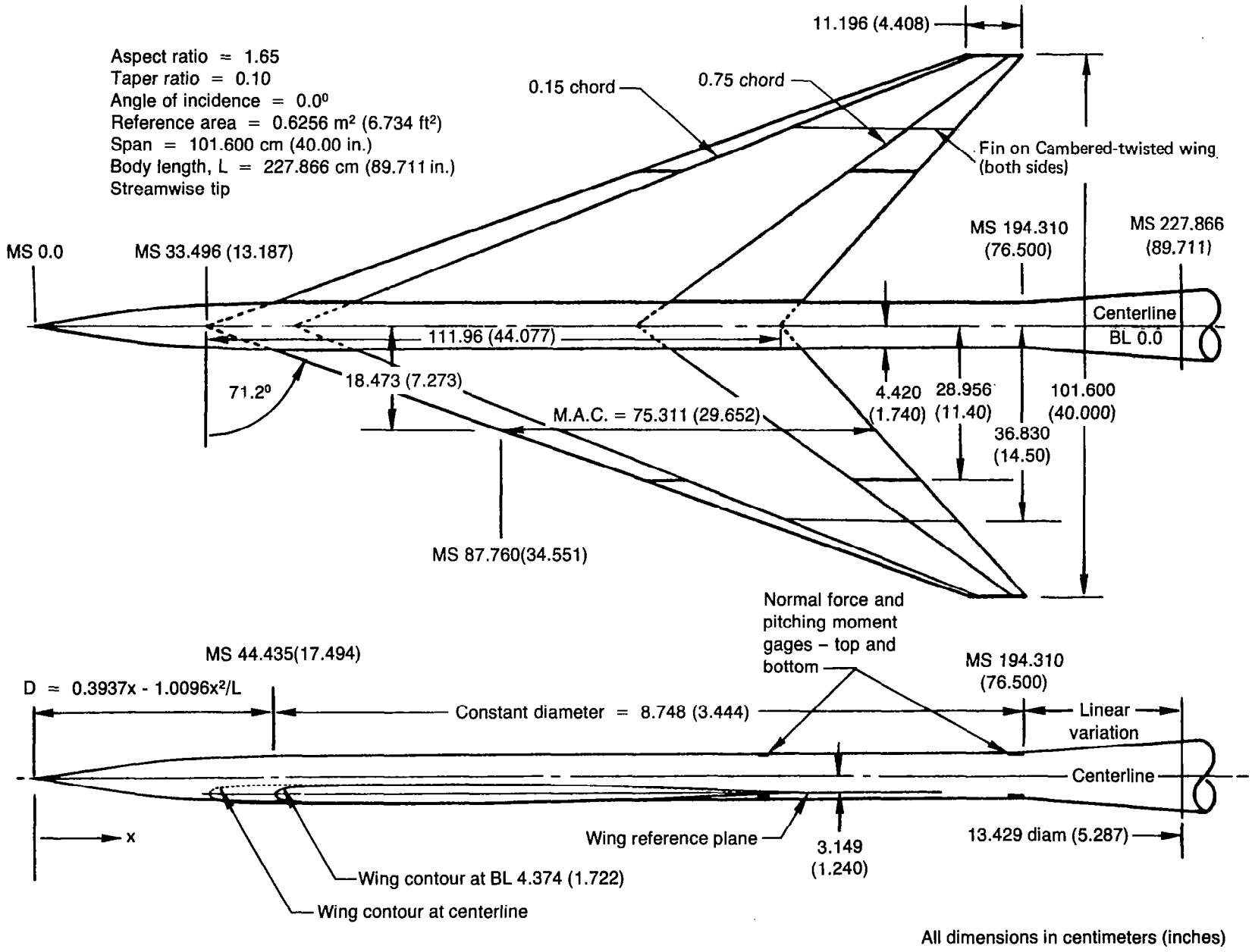

Figure A-1.—General Arrangement and Characteristics

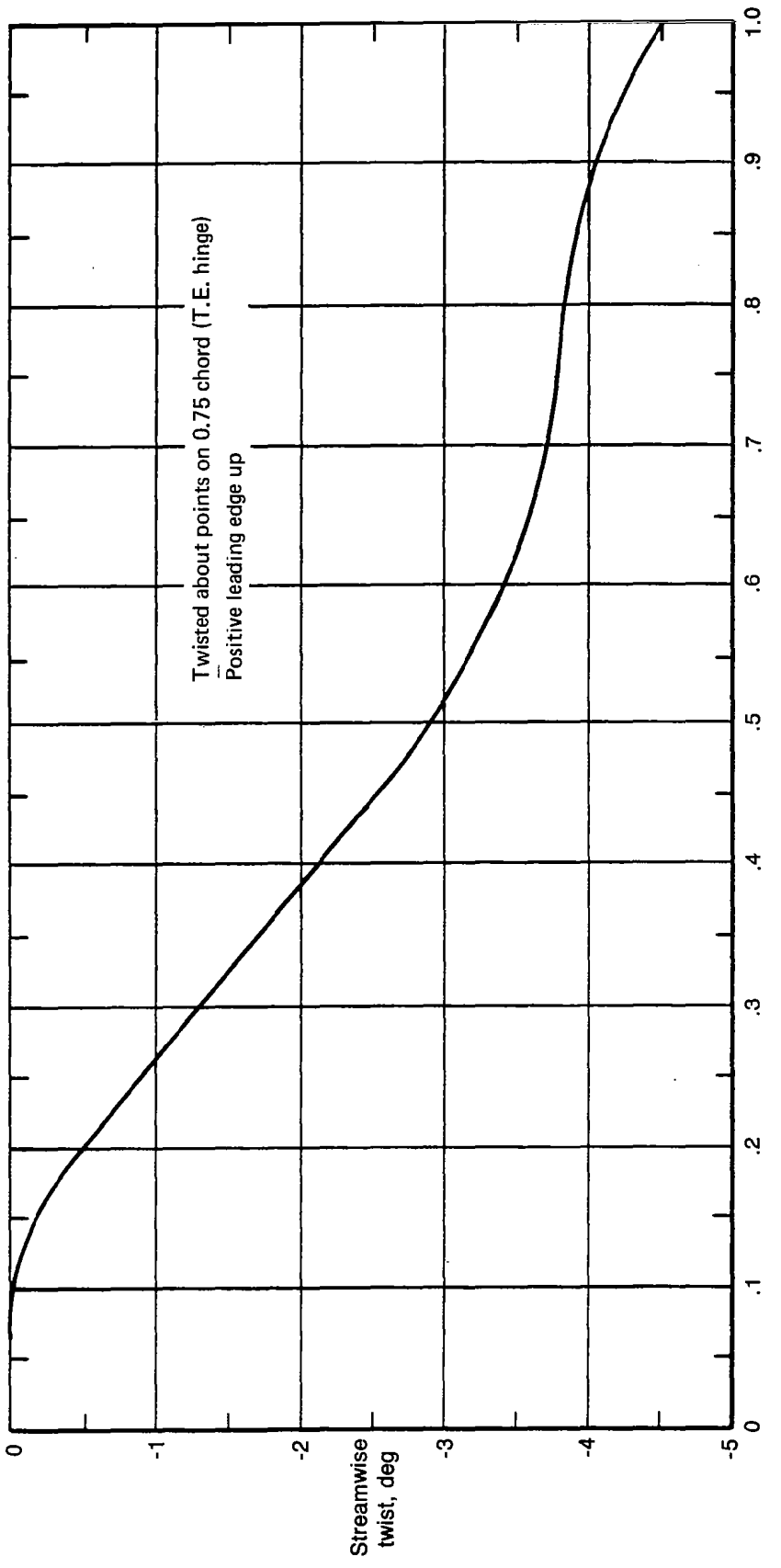

Figure A-2.—Spanwise Twist Distribution for the Model Wing

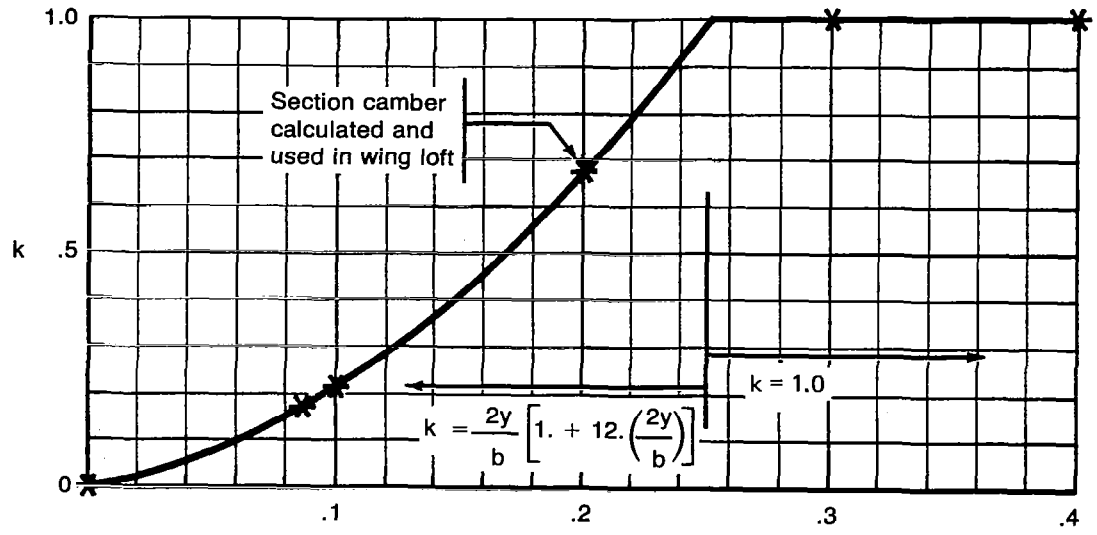

(a) Definition of k, Factor on Basic Camber

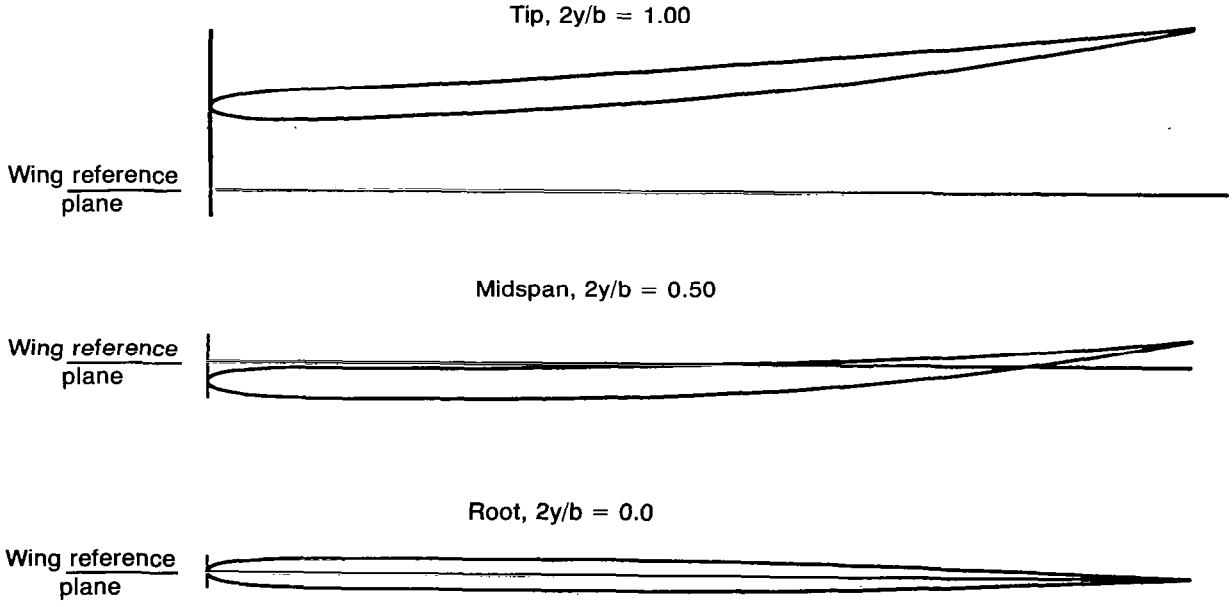

(b) Typical Sections

Figure A-3.—Cambered-Twisted Wing Section Geometry

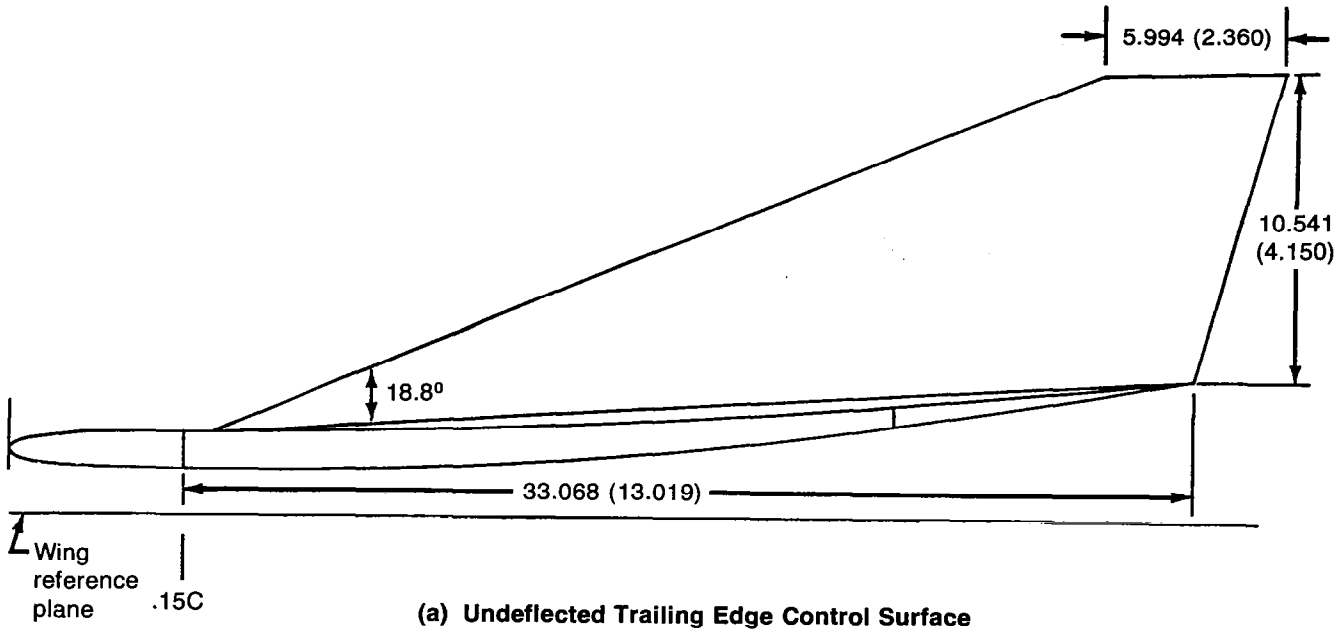

(a) Undeflected Trailing Edge Control Surface

All dimensions in centimeters (inches)

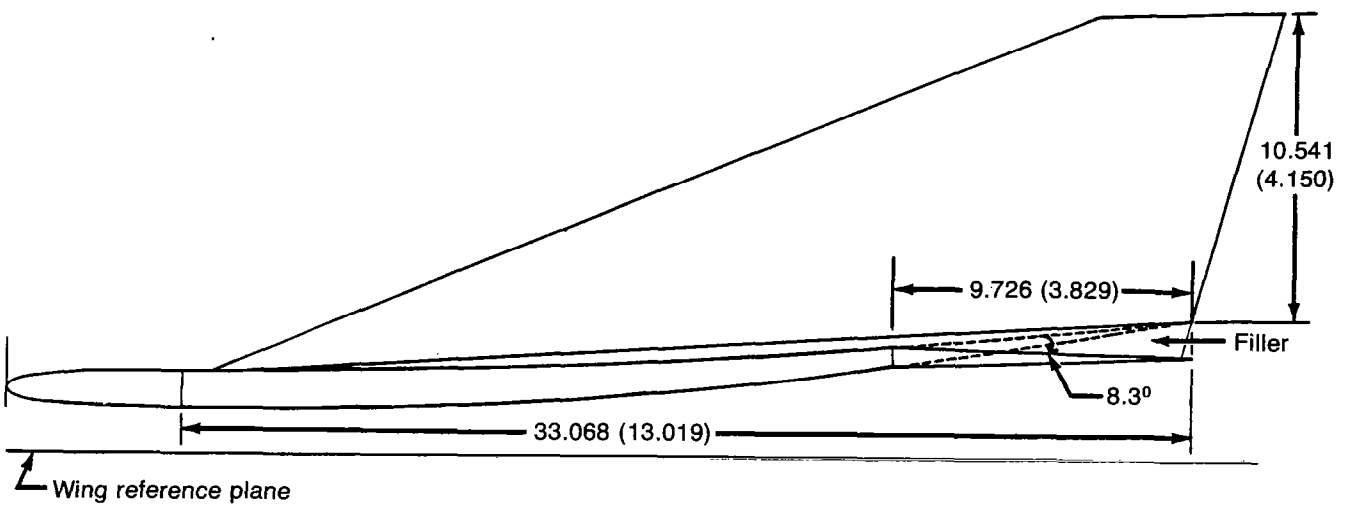

(b) Trailing Edge Control Surface Deflected 8.3°

Figure A-4.—Fin Geometry, Section at 0.725 Semispan

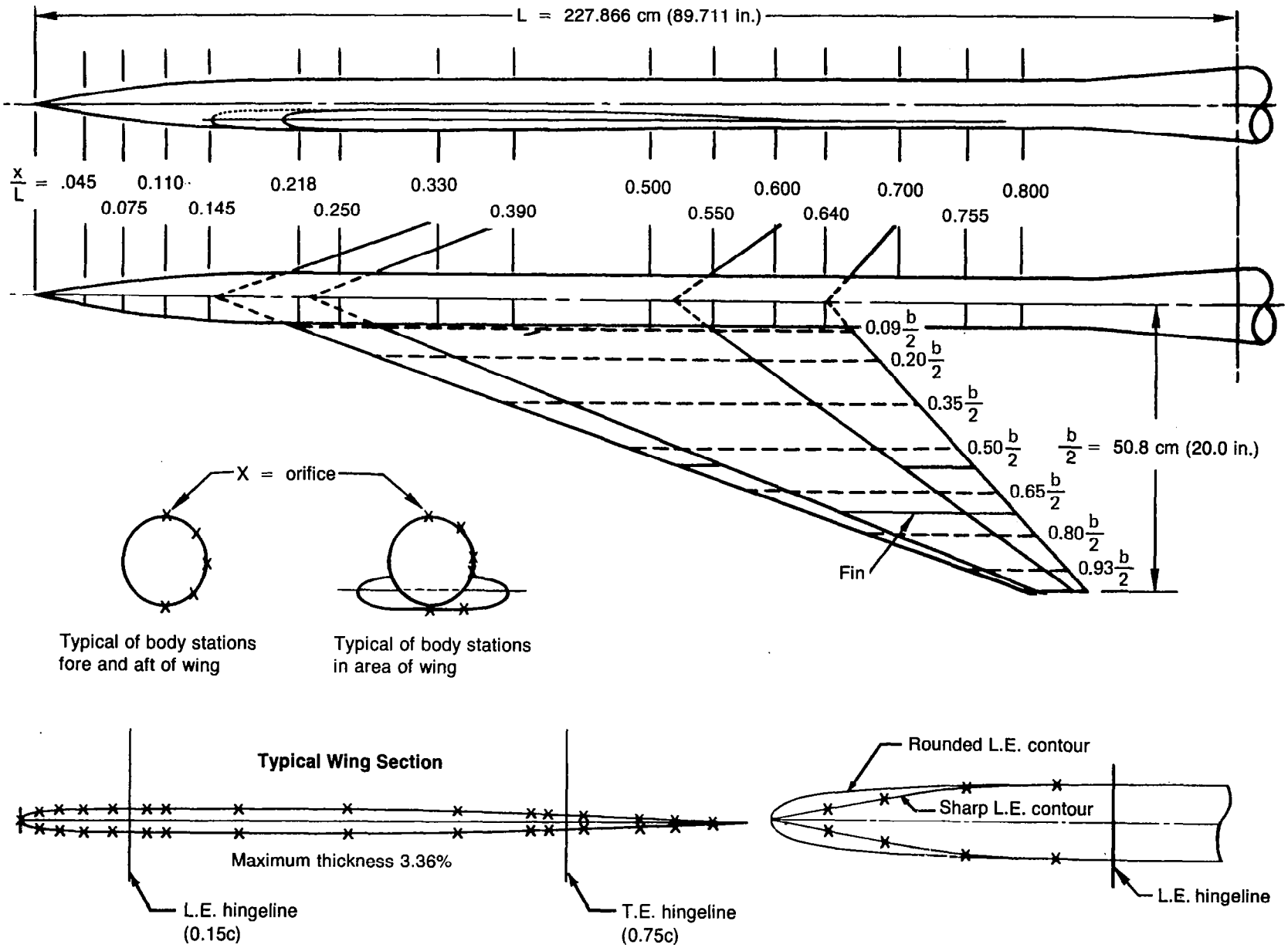

Figure A-5.–Pressure Orifice Locations

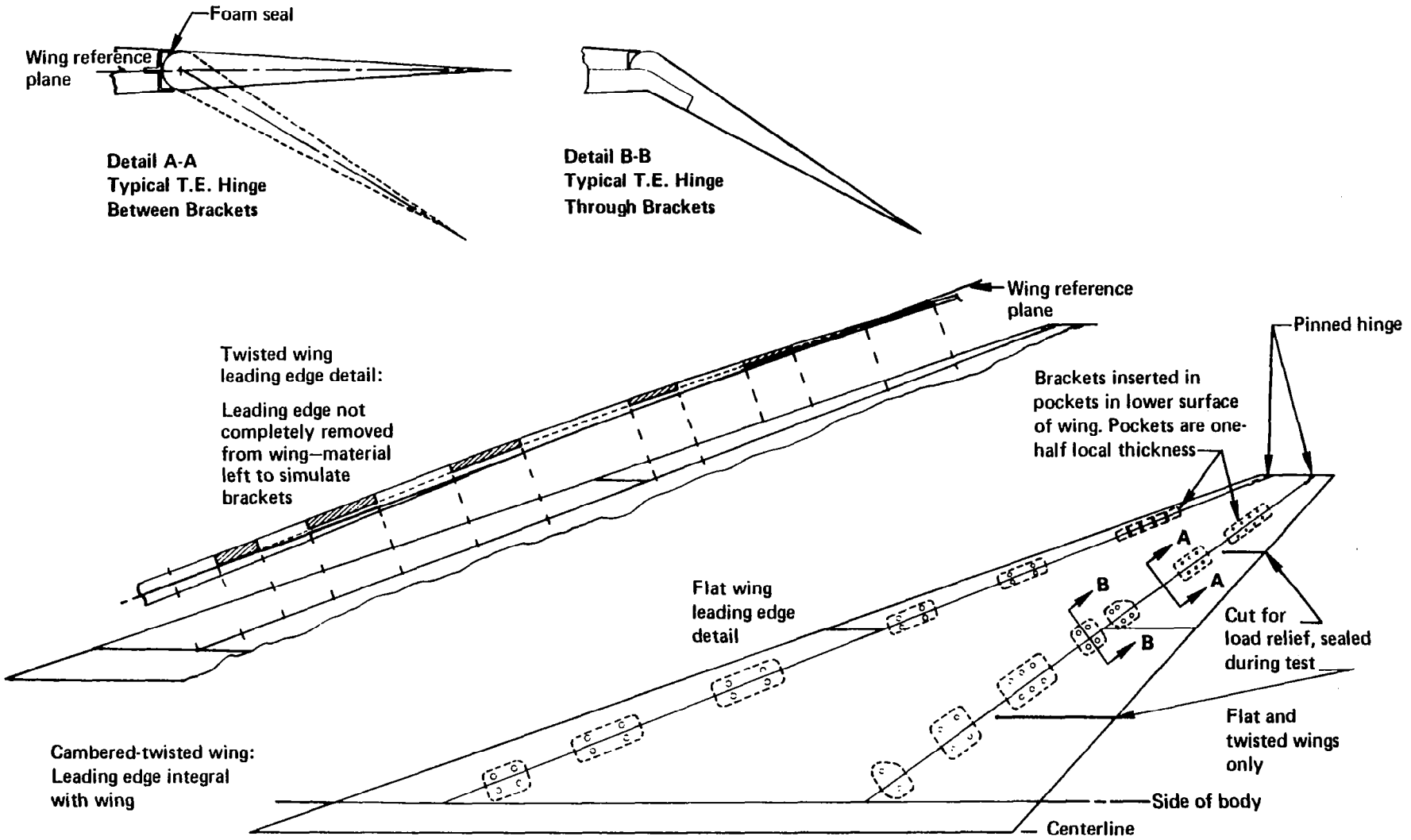

Figure A-6.—Control Surface Bracket Details

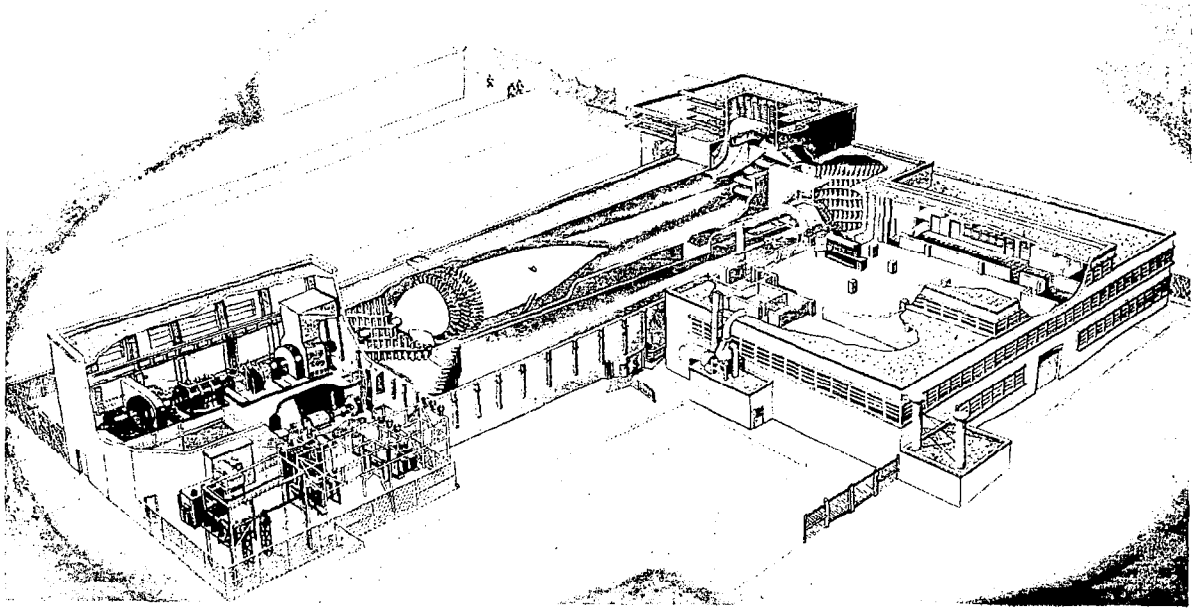

(a) Schematic

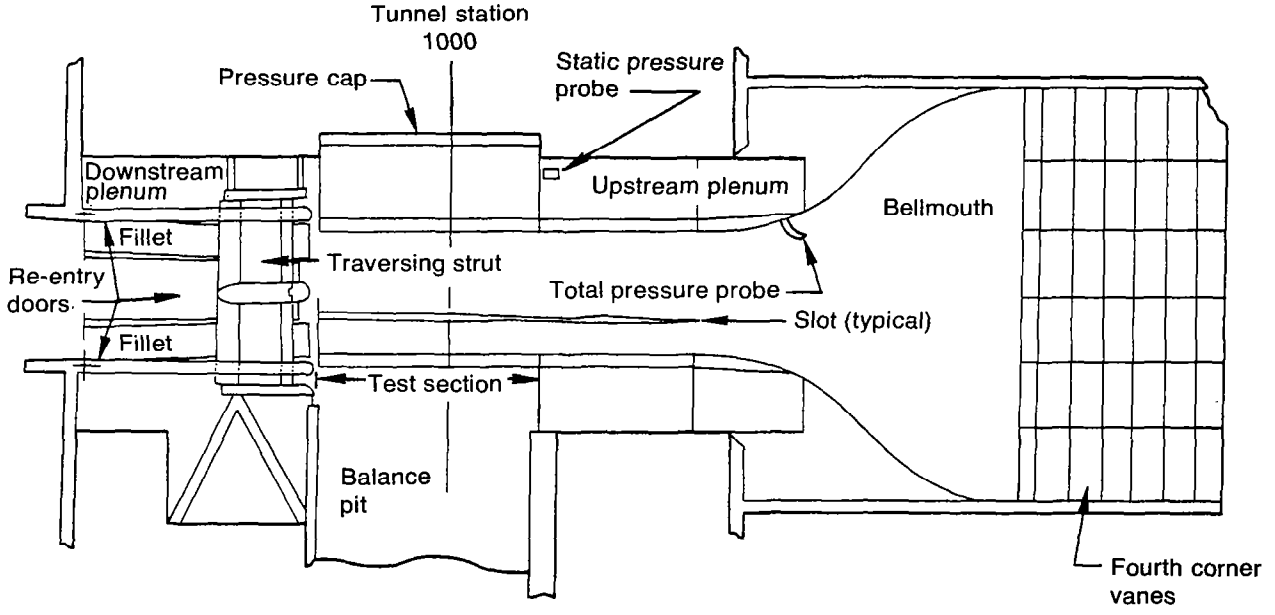

(b) Test Section

Figure A-7.—Boeing Transonic Wind Tunnel

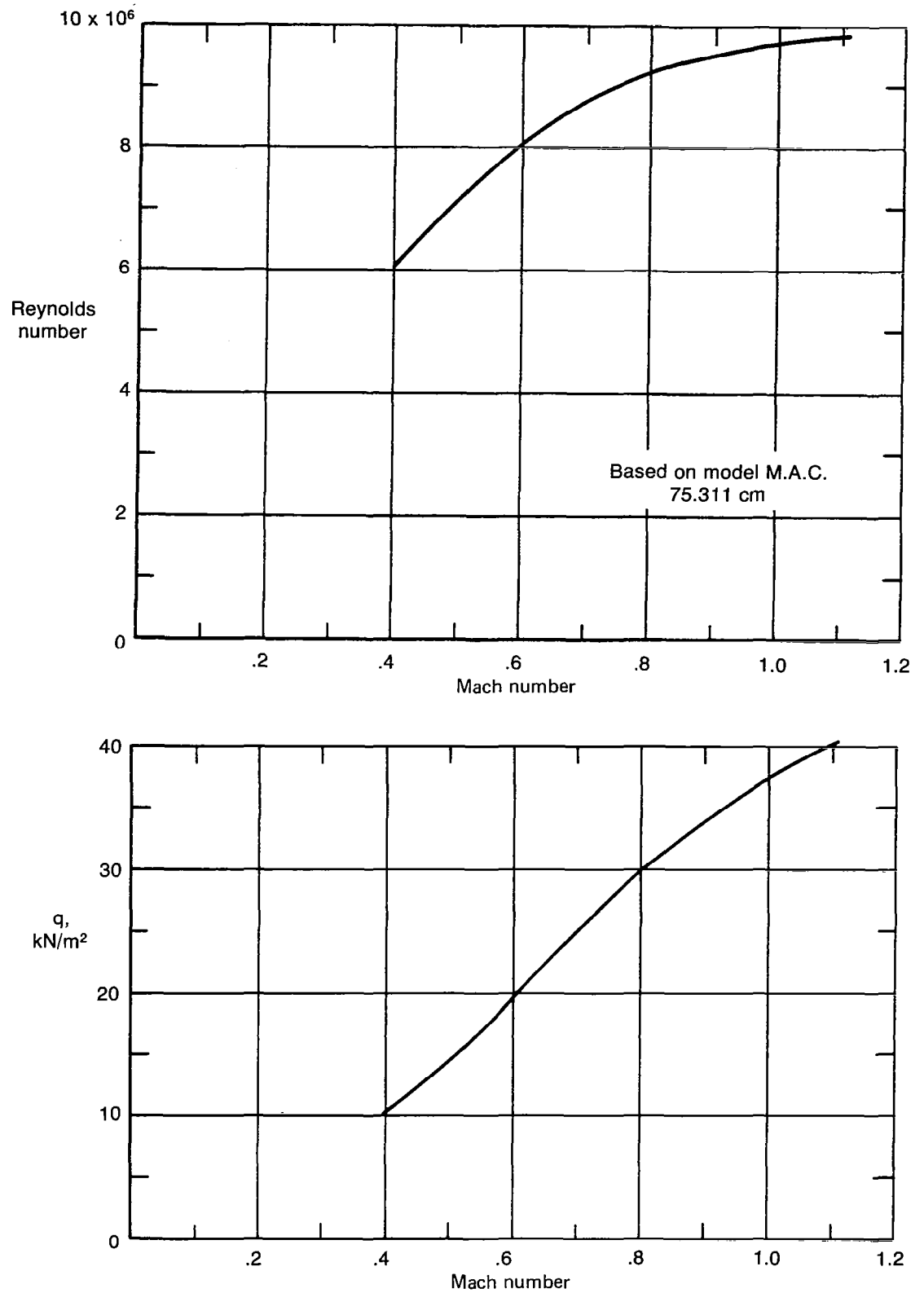

Figure A-8.—Variation of Reynolds Number and Dynamic Pressure With Mach Number

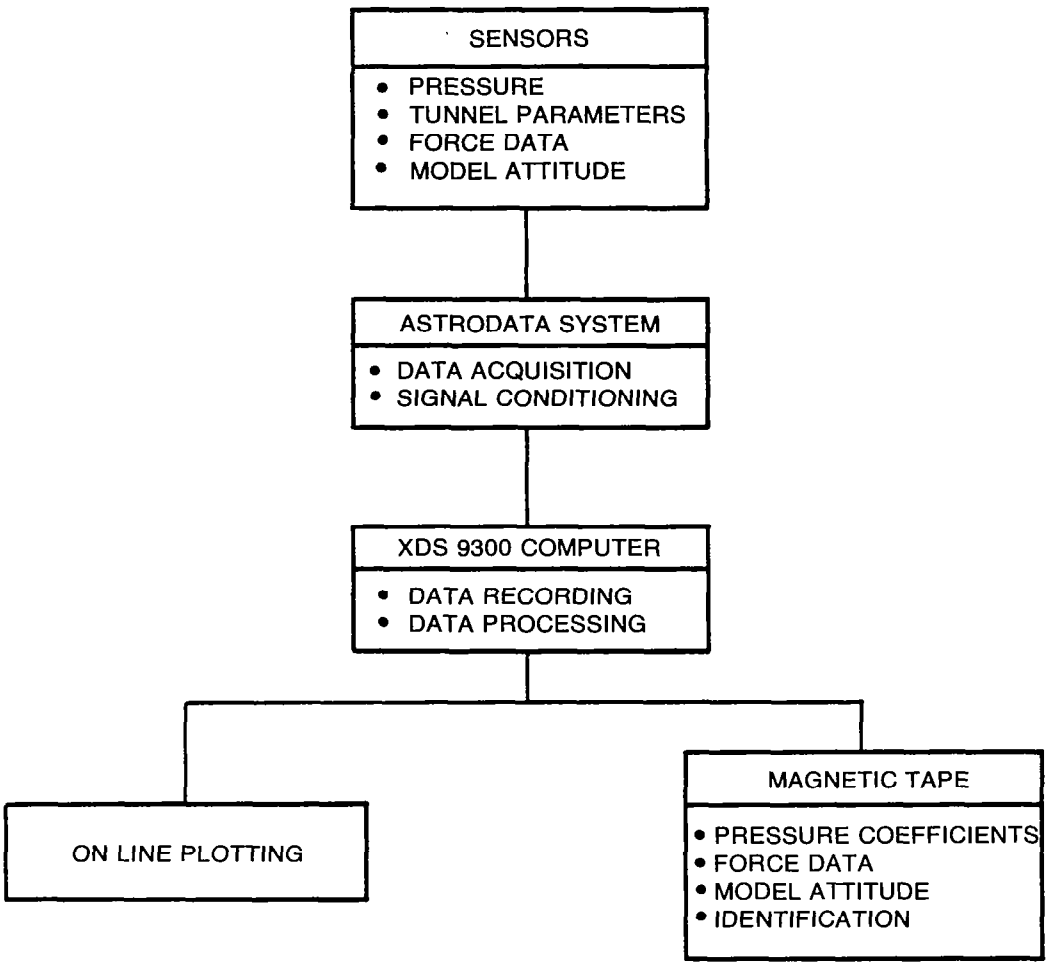

Figure A-9.—Data Acquisition and Reduction System—Boeing Transonic Wind Tunnel

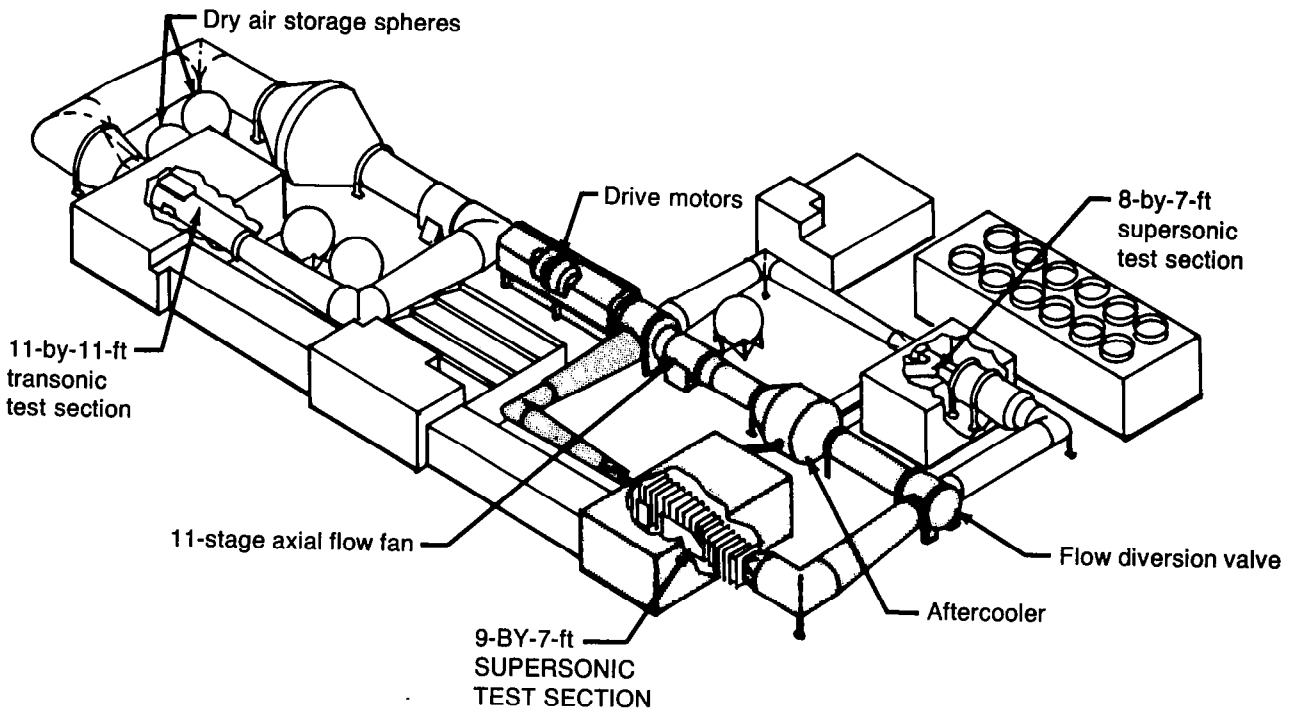

Figure A-10.—Schematic of 9- by 7-ft Supersonic Leg of NASA Ames Unitary Wind Tunnel

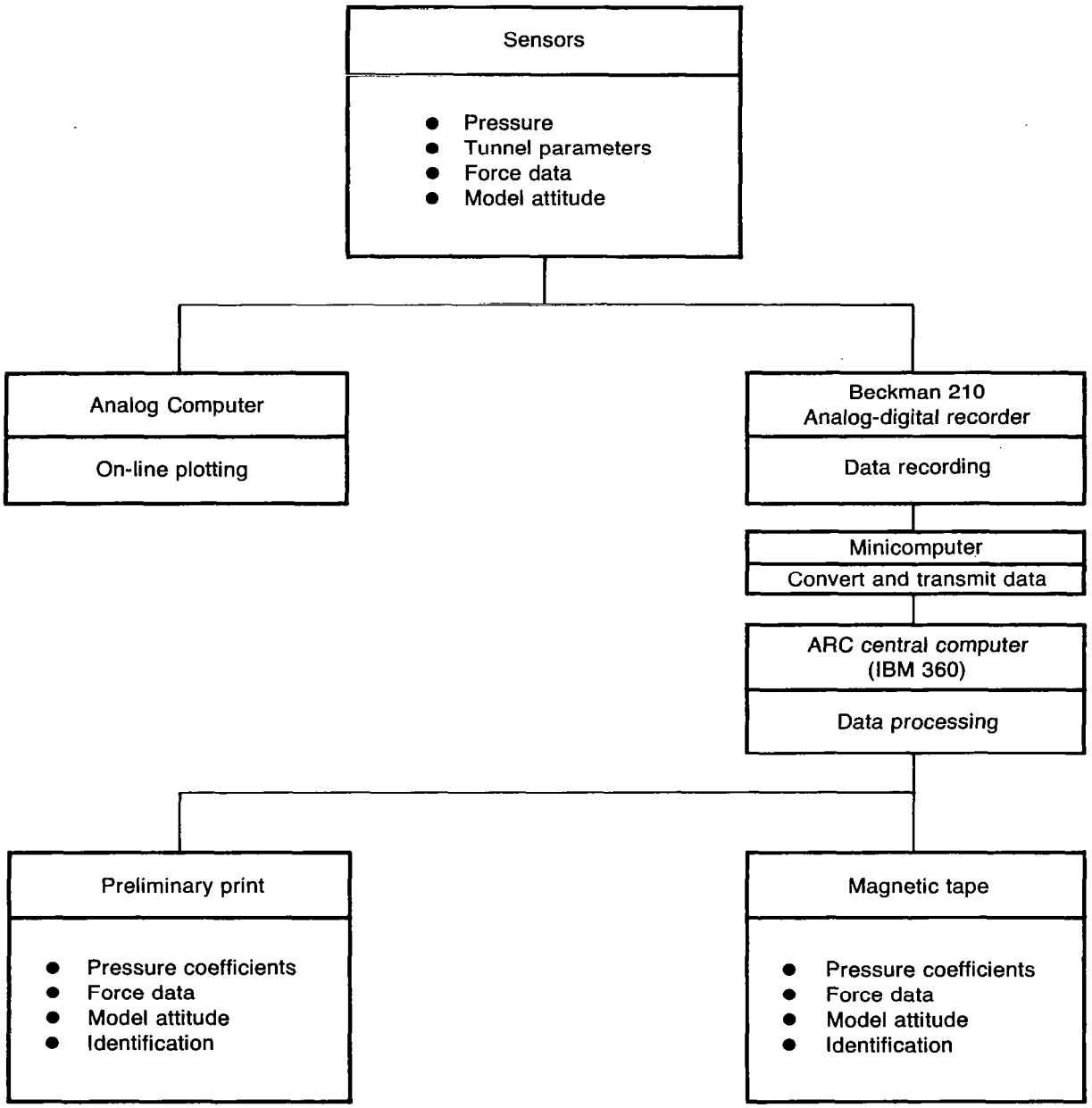

Figure A-11.—Data Acquisition and Reduction System—9- by 7-ft Supersonic Leg of NASA Ames Unitary Wind Tunnel

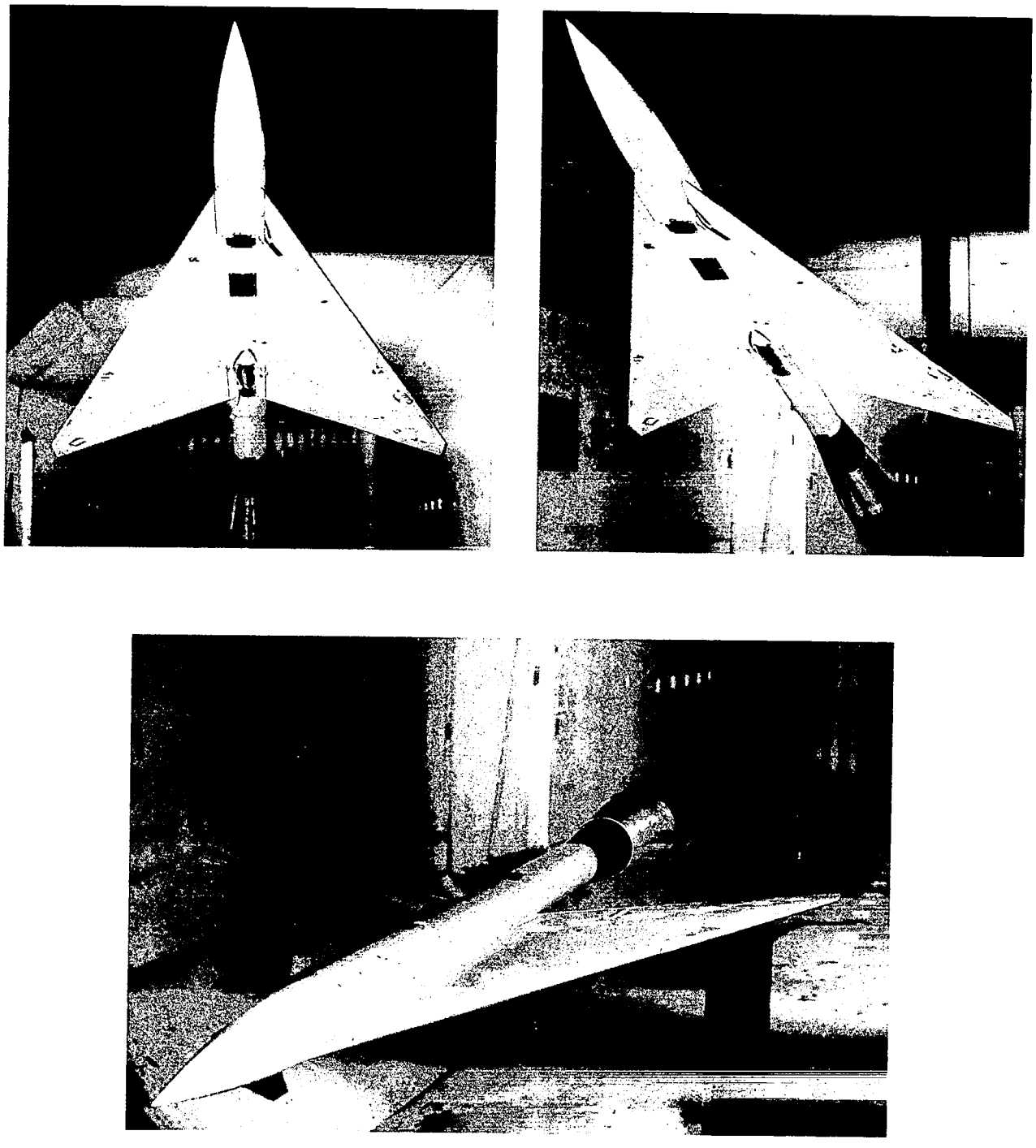

Figure A-12.—Model in Boeing Transonic Wind Tunnel—Flat Wing; L.E. Deflection, Full Span = 0.0°; T.E. Deflection, Full Span = 0.0° (NASA Contract NAS1-12875)

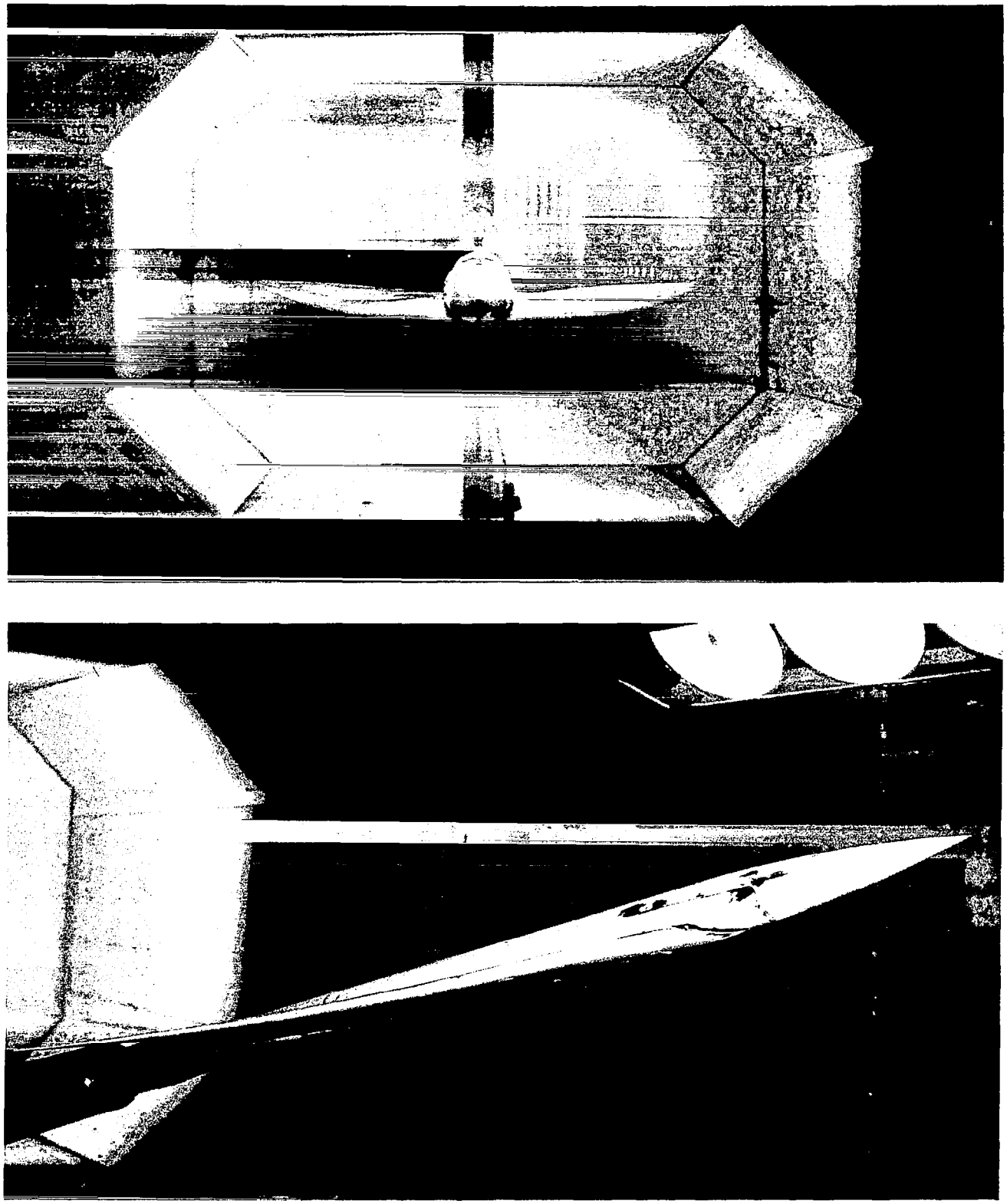

Figure A-13.—Model in Boeing Transonic Wind Tunnel—Twisted Wing; T.E. Deflection, Full Span = 0.0°; (NASA Contract NAS1-14962)

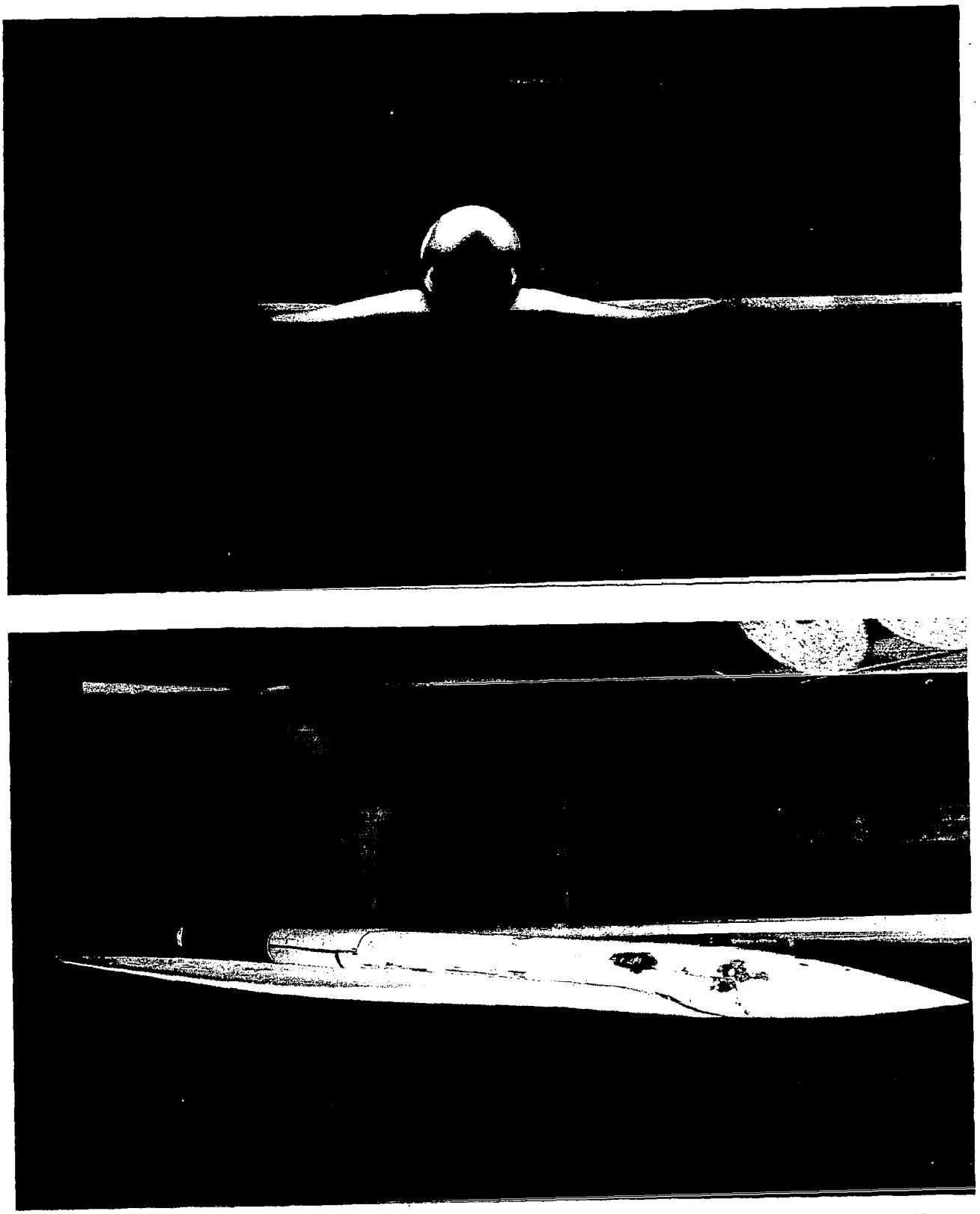

Figure A-14.—Model in Boeing Transonic Wind Tunnel—Cambered-Twisted Wing, Fin Off; T.E. Deflection, Full Span = 0.0°; (NASA Contract NAS1-14962)

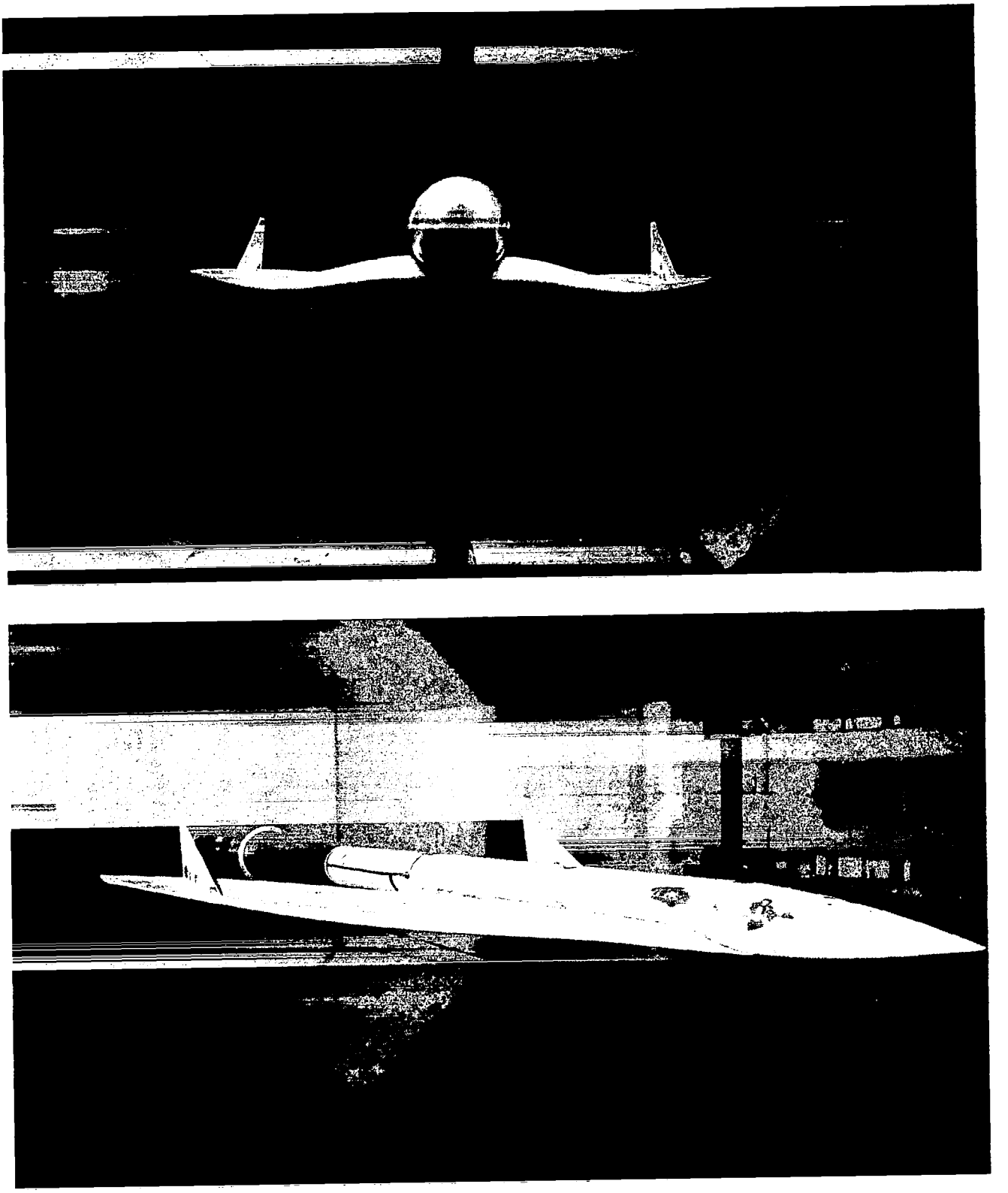

Figure A-15.—Model in Boeing Transonic Wind Tunnel—Cambered-Twisted Wing, Fin On; T.E. Deflection, Full Span = 0.0° (NASA Contract NAS1-14962)

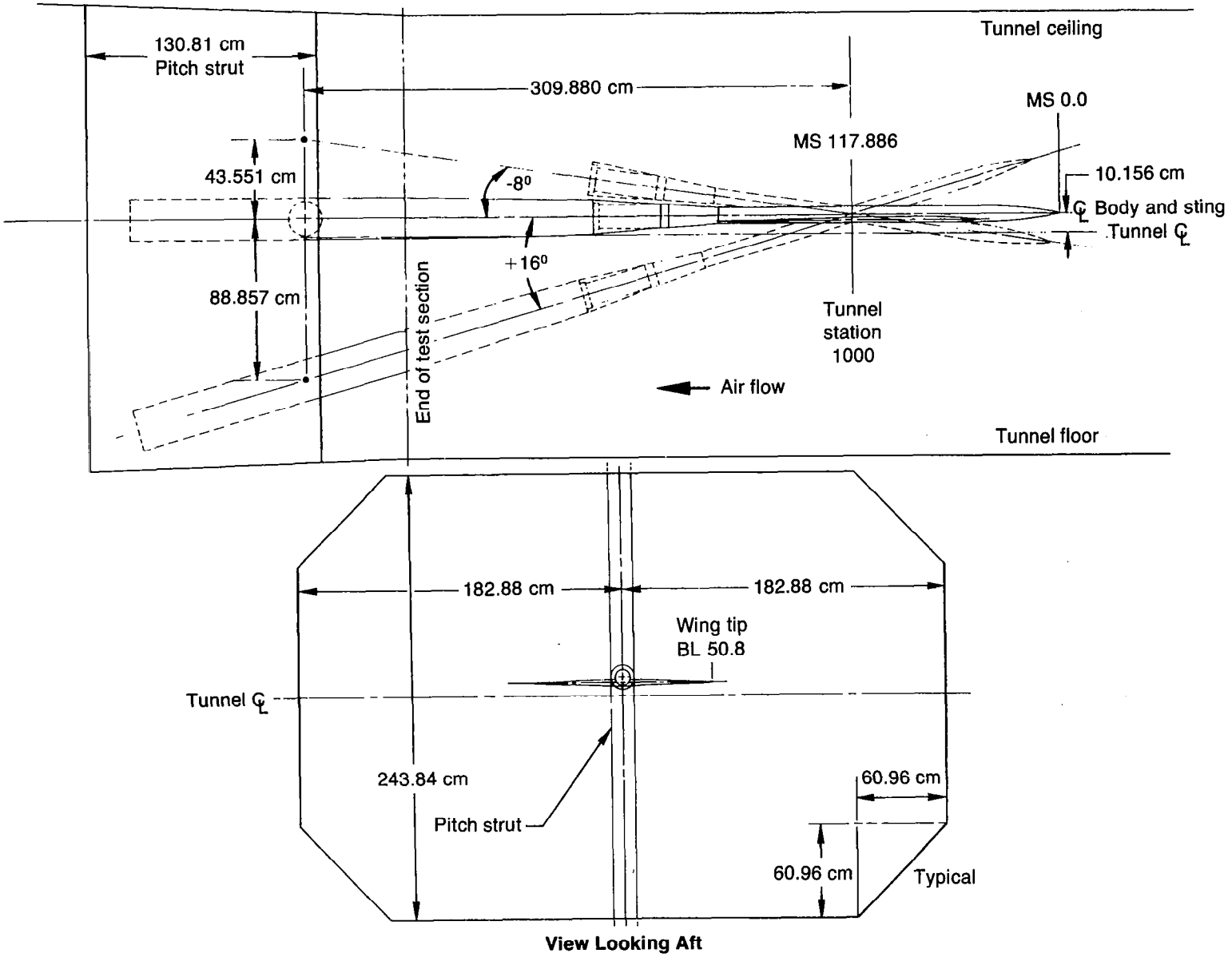

Figure A-16.—Model Installation in Boeing Transonic Wind Tunnel (NASA Contracts NAS1-12875 and NAS1-14962)

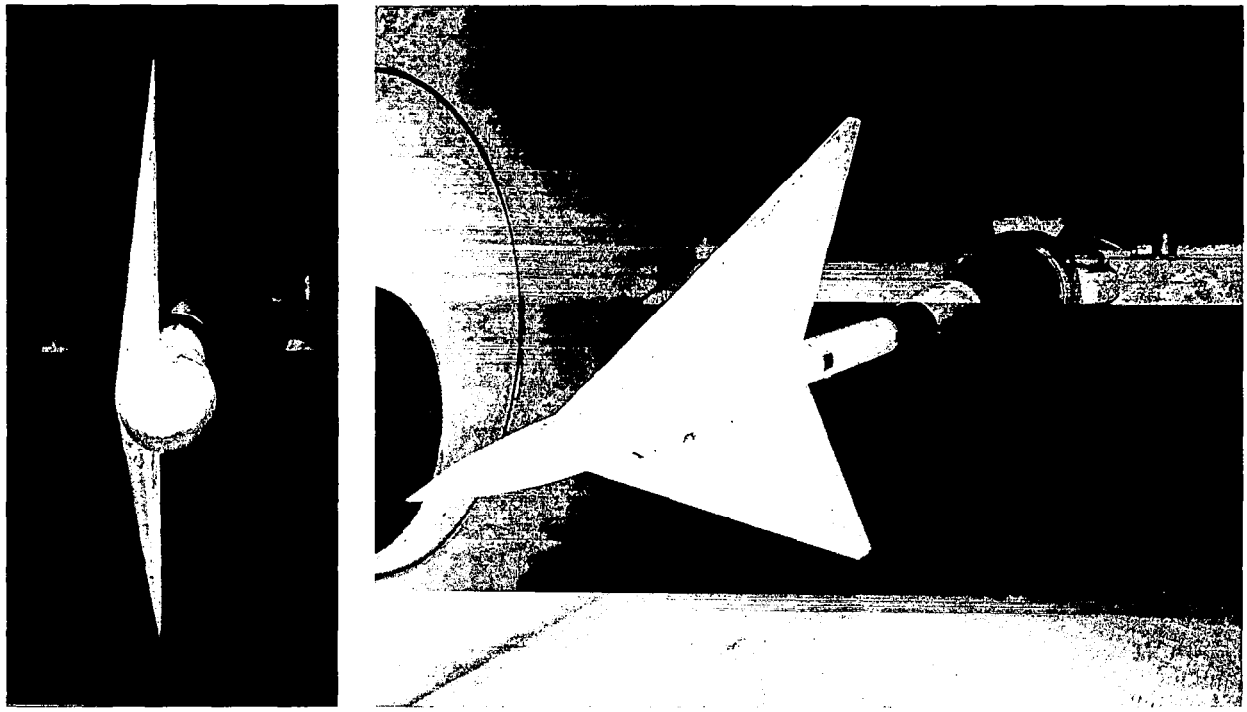

Figure A-17.—Model in 9- by 7-ft Supersonic Leg of NASA Ames Unitary Wind Tunnel—Flat Wing, Rounded L.E. (NASA Contract NAS1-14141)

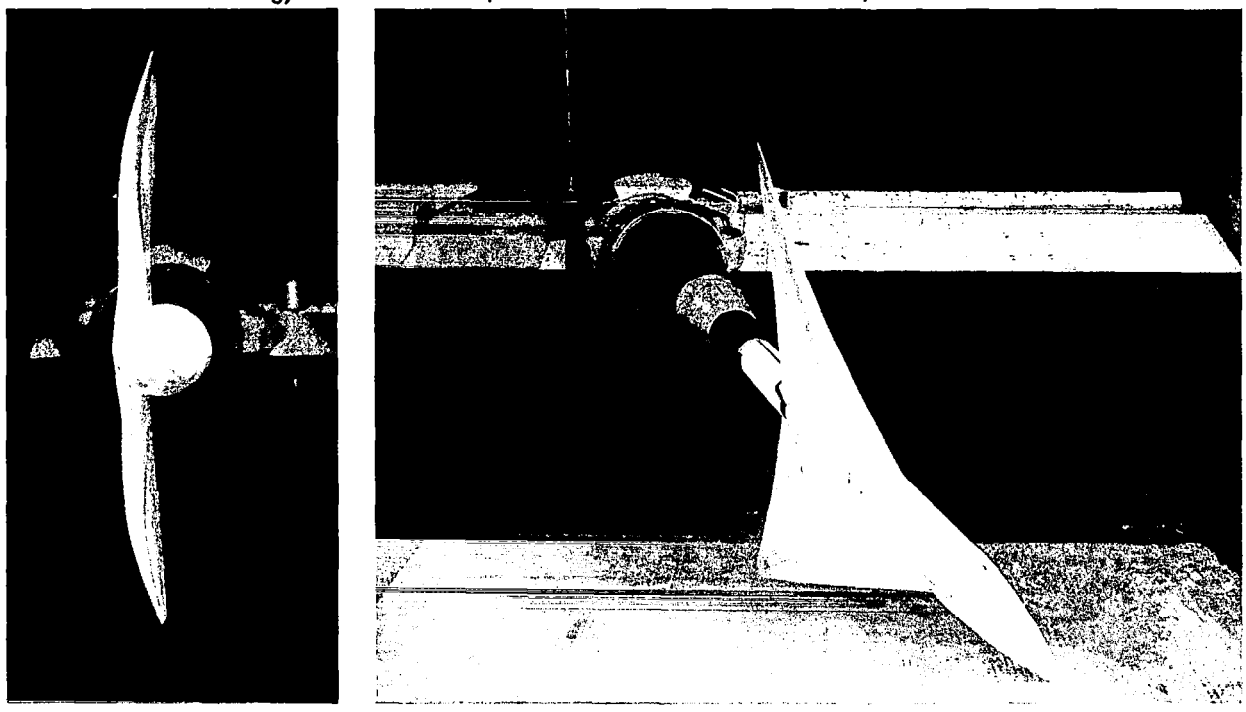

Figure A-18.—Model in 9- by 7-ft Supersonic Leg of NASA Ames Unitary Wind Tunnel—Twisted Wing (NASA Contract NAS1-14141)

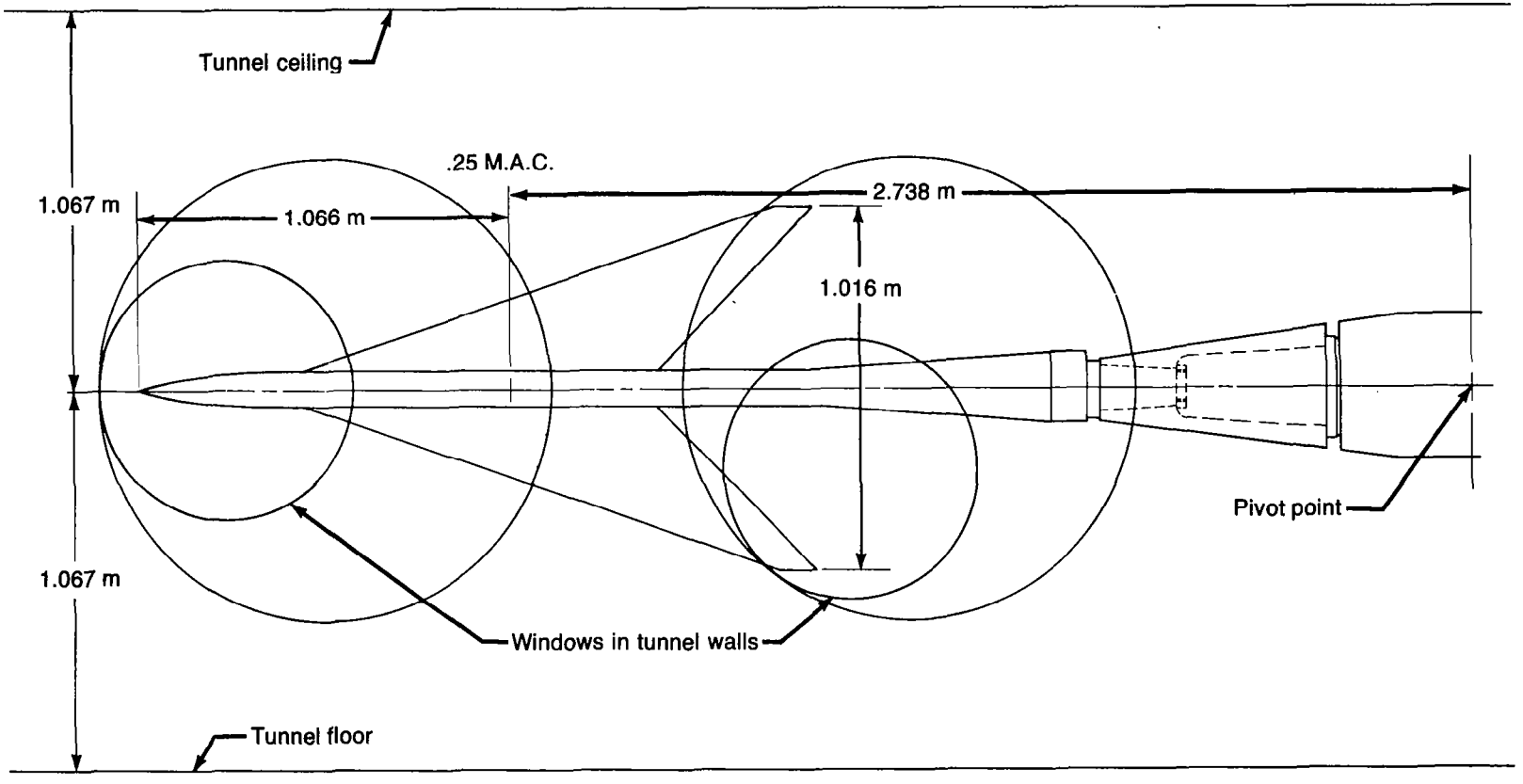

Figure A-19.—Model Installation in 9- by 7-ft Supersonic Leg of NASA Ames Unitary Wind Tunnel (NASA Contract NAS1-14141)

APPENDIX B

DATA REDUCTION

DATA EDITING

There were some cases encountered with these data where the methods of data editing available within the integration programs were not adequate. Because the plotting program assumes that the geometry is the same for all configurations, and the chordwise location of orifices on the various model parts was not absolutely identical, points were added as required. Therefore, some interpolations or extrapolations using selected orifices were done before the integration program was used. The row of orifices on the body at the wing-body intersection was extended in front of the wing and aft of the wing by interpolating between the orifices located at 90^0 and 135^0.

Some specific problems with the data acquisition systems required the replacement of some data for parts of tests. These are identified in appendix A.

Several methods were introduced into the integration program to replace or add data points to account for:

- Plugged or leaking orifices, or bad data points
- Extrapolating the data to leading and trailing edges
- Hingeline discontinuities in the pressure data

These procedures were selected by code for each point. The codes are described in the following list and are illustrated in figure B-1. An additional use of these codes is to ensure that only measured pressure data ($CODE_i = 0$) are identified with symbols on the plots. The subscript i identifies the position of the point from the leading edge of the upper or lower surface of the section.

IF $CODE_i$ = 0, use pressure as entered on tape (measured pressure)

= 20, use as entered on tape (previously replaced value)

= 1, interpolate from adjacent points

= 2, extrapolate from two preceding points

= 3, extrapolate from two following points

= 4, set equal to preceding point

= 5, set equal to following point

= 6, interpolate using points (i-2) and (i+1)

= 7, interpolate using points (i-1) and (i+2)

IF $CODE_i$ = negative of above, evaluate as above but average with corresponding point on opposite surface; used for leading and trailing edges of section only

Editing of the pressure data is done in the following order:

1. Each section is done separately.
2. Each surface (upper or lower) per section is done in the following sequence:
   a. Starting at leading edge, points with codes of 1, 2, and 4.
   b. Starting at trailing edge, points with codes of 3, 5, 6, and 7.
3. Leading- and trailing-edge points with negative codes are evaluated. Both upper and lower surface codes need not be negative and need not be the same negative code.

CALCULATION OF NET PRESSURE COEFFICIENTS

The net lift distribution on the section is calculated by:

$$C_{p,net} = C_{p,lower} - C_{p,upper} \tag{B-1}$$

INTEGRATION OF PRESSURE DATA

To account for the effects on integrated coefficients of the deflected control surfaces, each streamwise section (of which there are NSECT) is divided into segments (of which there are NSEG). These segments are the leading-edge control surface, wing box, and trailing-edge control surface. The upper and lower surfaces of each are integrated separately over the number of points available ((number of orifices + 2) = NP1), and are based on the segment chord length c. Sign conventions are shown in the following sketch. The equations, which use a rectangular integration process, follow.

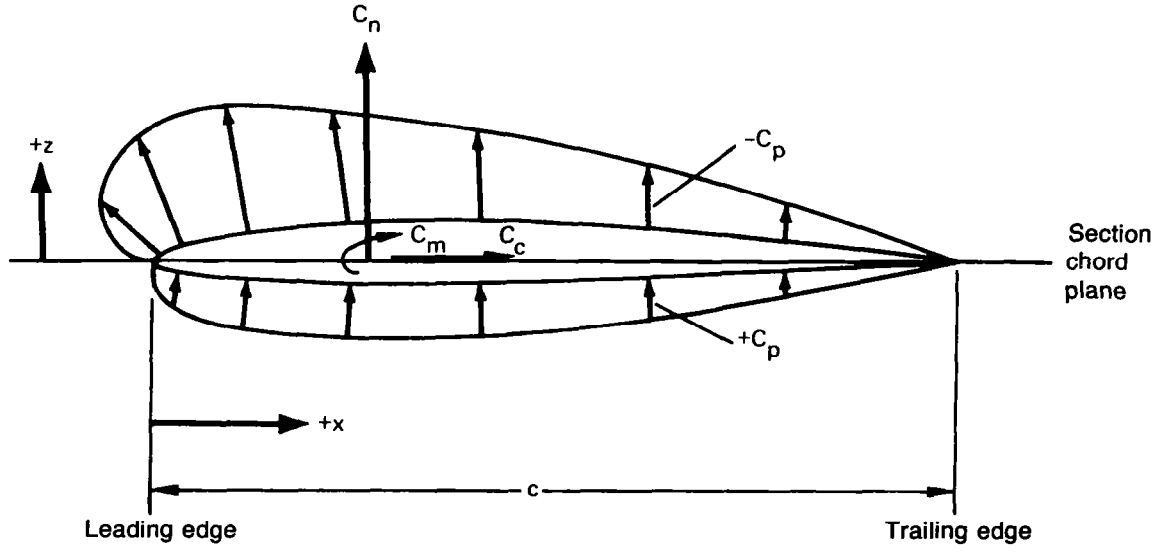

SEGMENT COEFFICIENTS

Integration of the pressures for each segment per surface per section is the first step.

o Normal force coefficient $C_{n,s}$

$$C_{n,s} = 0.5 \sum_{i=2}^{NP1} \left[(C_p)_i + (C_p)_{i-1}\right]\left[\left(\frac{x}{c}\right)_i - \left(\frac{x}{c}\right)_{i-1}\right] \quad \text{(B-2)}$$

$$C_{n,s,net} = C_{n,s,lower} - C_{n,s,upper} \quad \text{(B-3)}$$

o Chord force coefficient $C_{c,s}$

$$C_{c,s} = 0.5 \sum_{i=2}^{NP1} \left[(C_p)_i + (C_p)_{i-1}\right]\left[\left(\frac{z}{c}\right)_i - \left(\frac{z}{c}\right)_{i-1}\right] \quad \text{(B-4)}$$

$$C_{c,s,net} = C_{c,s,upper} - C_{c,s,lower} \quad \text{(B-5)}$$

o Pitching moment coefficient about segment leading edge $C_{m,s}$

$$C_{m,s} = 0.5 \sum_{i=2}^{NP1} \left[(C_p)_i + (C_p)_{i-1}\right]\left[\left(\frac{x}{c}\right)_{i-1} + \frac{\left(\frac{x}{c}\right)_i - \left(\frac{x}{c}\right)_{i-1}}{2.0}\right]\left[\left(\frac{x}{c}\right)_i - \left(\frac{x}{c}\right)_{i-1}\right]$$

$$= 0.25 \sum_{i=2}^{NP1} \left[(C_p)_i + (C_p)_{i-1}\right]\left[\left(\frac{x}{c}\right)_i^2 - \left(\frac{x}{c}\right)_{i-1}^2\right] \quad \text{(B-6)}$$

$$C_{m,s,net} = C_{m,s,upper} - C_{m,s,lower} \quad \text{(B-7)}$$

o Pitching moment coefficient about 0.25 c of segment $C_{m.25c,s}$

$$C_{m.25c,s} = C_{m,s,} + 0.25\, C_{n,s} \quad \text{(B-8)}$$

SECTION COEFFICIENTS

Total section coefficients are obtained by summing the segment coefficients, taking into account both the segment deflections as defined in the following sketch and the segment chord lengths. These coefficients are based on the section chord length c.

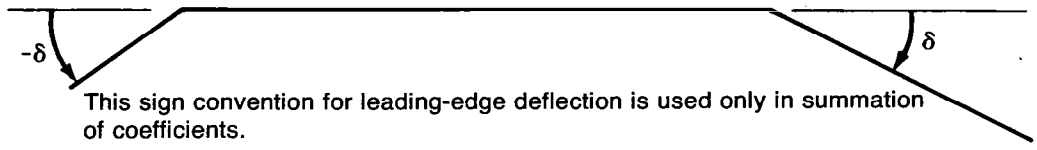

o Normal force coefficient C_n

$$C_n = \sum_{j=1}^{NSEG} (C_{n,s})_j \left(\frac{c_s}{c}\right)_j \cos\delta_j - \sum_{j=1}^{NSEG} (C_{c,s})_j \left(\frac{c_s}{c}\right)_j \sin\delta_j \qquad \text{(B-9)}$$

o Pitching moment coefficient about section leading edge C_m

$$C_m = \sum_{j=1}^{NSEG} (C_{m,s})_j \left(\frac{c_s}{c}\right)_j^2 + \left[(C_{n,s})_1 (1.0 - \cos\delta_1) + (C_{c,s})_1 \sin\delta_1\right] \left(\frac{c_s}{c}\right)_1^2$$

$$- \sum_{j=2}^{NSEG} \left[(C_{n,s})_j \cos\delta_j - (C_{c,s})_j \sin\delta_j\right] \left(\frac{c_s}{c}\right)_j \left[\frac{x_{L.E.,s} - x_{L.E.}}{c}\right]_j \qquad \text{(B-10)}$$

where

c_s is segment chord length, cm

c is section chord length, cm

δ is deflection of segment relative to section chord plane, leading edge up, degrees

$x_{L.E.,s}$ is leading edge of segment, cm

$x_{L.E.}$ is leading edge of section, cm

o Pitching moment coefficient about 0.25 c of section $C_{m.25c}$

$$C_{m.25c} = C_m + 0.25\, C_n \qquad \text{(B-11)}$$

TOTAL SURFACE COEFFICIENTS

To obtain total surface coefficients, the assumption is made that the section coefficients apply for a finite distance on both sides of each row of orifices. The equations for total surface coefficients are as follows:

o Normal force coefficient C_N

$$C_N = \frac{1}{S} \sum_{k=1}^{NSECT} (C_n)_k (S_h)_k \qquad \text{(B-12)}$$

o Bending moment coefficient C_B

$$C_B = \frac{1}{S(b/2)} \sum_{k=1}^{NSECT} (C_n)_k (S_h{}^y)_k \qquad \text{(B-13)}$$

o Pitching moment coefficient about 0.25 M.A.C. C_M

$$C_M = \frac{1}{S\bar{c}} \sum_{k=1}^{NSECT} \left\{ (C_m)_k (S_h{}^c)_k + (C_n)_k (S_h)_k \left[x_{ref} - (x_{L.E.})_k \right] \right\} \qquad \text{(B-14)}$$

where

$\bar{c}$ is reference chord for pitching moment, cm

x_{ref} is reference station for pitching moment, cm (0.25 M.A.C.)

$X_{L.E.}$ is leading edge of section chord, cm

b/2 is reference length for bending moment, cm

DETERMINATION OF GEOMETRIC CONSTANTS REQUIRED FOR INTEGRATION

To obtain total surface coefficients, the assumption is made that the section coefficients apply for a finite distance on both sides of each row of orifices. The input geometry required to calculate the areas, and products of area and length required for the summation of total surface coefficients, is shown in the following sketch.

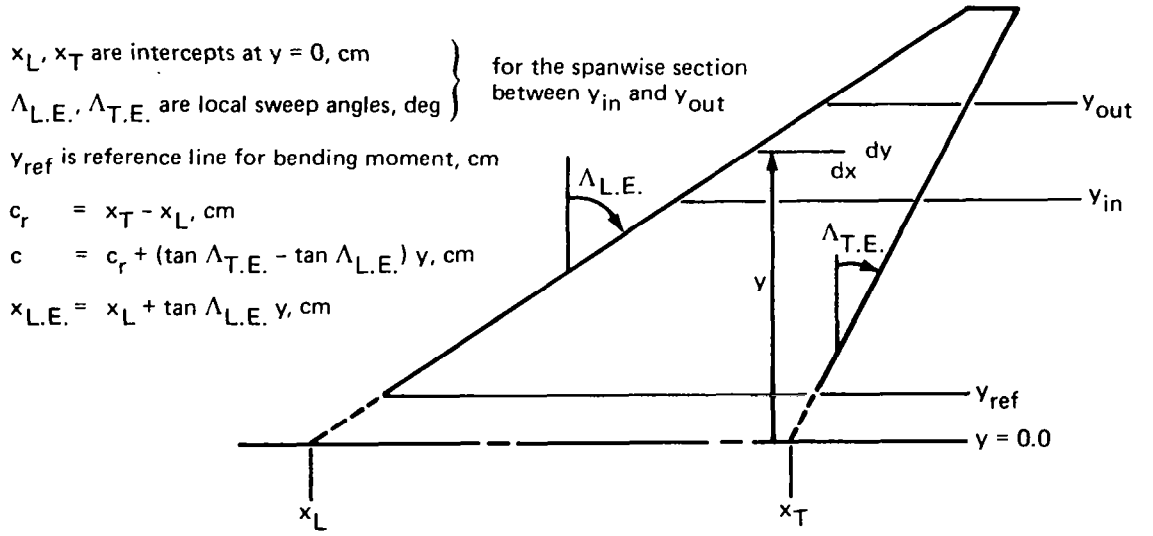

o Section area:

$$S_h = \int_{y_{in}}^{y_{out}} \int_{x_L + \tan \Lambda_{L.E.} y}^{x_T + \tan \Lambda_{T.E.} y} dy\, dx$$

$$= c_r (y_{out} - y_{in}) + 0.5 \left(\tan \Lambda_{T.E.} - \tan \Lambda_{L.E.}\right) \left(y_{out}^2 - y_{in}^2\right) \quad \text{(B-15)}$$

o Product of section area and mean chord:

$$S_h c = \int_{y_{in}}^{y_{out}} \int_{x_L + \tan \Lambda_{L.E.} y}^{x_T + \tan \Lambda_{T.E.} y} c\, dy\, dx$$

$$= c_r^2 (y_{out} - y_{in}) + c_r \left(\tan \Lambda_{T.E.} - \tan \Lambda_{L.E.}\right) \left(y_{out}^2 - y_{in}^2\right)$$

$$+ \frac{\left(\tan \Lambda_{T.E.} - \tan \Lambda_{L.E.}\right)^2}{3.0} \left(y_{out}^3 - y_{in}^3\right) \quad \text{(B-16)}$$

- **Product of section area and bending moment arm:**

$$S_h y = \int_{y_{in}}^{y_{out}} \int_{x_L + \tan \Lambda_{L.E.} y}^{x_T + \tan \Lambda_{T.E.} y} (y - y_{ref}) dy\, dx$$

$$= \frac{c_r - (\tan \Lambda_{T.E.} - \tan \Lambda_{L.E.}) y_{ref}}{2.0} (y_{out}^2 - y_{in}^2)$$

$$+ \frac{\tan \Lambda_{T.E.} - \tan \Lambda_{L.E.}}{3.0} (y_{out}^3 - y_{in}^3) - c_r y_{ref} (y_{out} - y_{in}) \qquad \text{(B-17)}$$

- **Product of section area and leading-edge coordinate:**

$$S_h x = \int_{y_{in}}^{y_{out}} \int_{x_L + \tan \Lambda_{L.E.} y}^{x_T + \tan \Lambda_{T.E.} y} x_{L.E.}\, dy\, dx$$

$$= x_L c_r (y_{out} - y_{in}) + \frac{\tan \Lambda_{L.E.} c_r + x_L (\tan \Lambda_{T.E.} - \tan \Lambda_{L.E.})}{2.0} (y_{out}^2 - y_{in}^2)$$

$$+ \tan \Lambda_{L.E.} \frac{(\tan \Lambda_{T.E.} - \tan \Lambda_{L.E.})}{3.0} (y_{out}^3 - y_{in}^3) \qquad \text{(B-18)}$$

- **Total surface reference area:**

$$S = \sum_{k=1}^{NSECT} (S_h)_k \qquad \text{(B-19)}$$

- **M.A.C. and X coordinate of M.A.C. leading edge:**

$$\bar{c} = \frac{1}{S} \sum_{k=1}^{NSECT} (S_h c)_k \qquad \text{(B-20)}$$

$$x_{L.E.,M.A.C.} = \frac{1}{S} \sum_{k=1}^{NSECT} (S_h x)_k \qquad \text{(B-21)}$$

The required integration constants for the wing and body are shown in table B-1.

Table B-1.—Integration Constants

Reference area = 3128.45 cm^2
M.A.C. = 75.311 cm
Half span = 50.80 cm

Pitching moment referenced to 0.25 M.A.C.

Bending moment referenced to $0.086\frac{b}{2}$ (y_{ref} = 4.374 cm)

L.E. of M.A.C. at B.S. 87.760 cm

Wing

2y/b	$\frac{\Delta y}{(b/2)}$	Area cm^2	Area • chord cm^3	Area • $(y-y_{ref})$ cm^3
0.09	0.0425	219.69	22 357.	167.
0.20	0.1575	733.51	67 415.	4 206.
0.35	0.1500	580.54	44 374.	7 857.
0.50	0.1400	437.93	27 084.	9 148.
0.65	0.1600	377.64	17 722.	10 729.
0.80	0.1300	210.35	6 794.	7 528.
0.93	0.1400	129.79	2 487.	5 505.

Body

Longitudinal section	Area cm^2	Area • L cm^3
1	356.61	81 258.
2	504.32	114 916.
3	70.94	16 164.

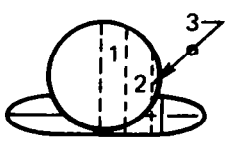

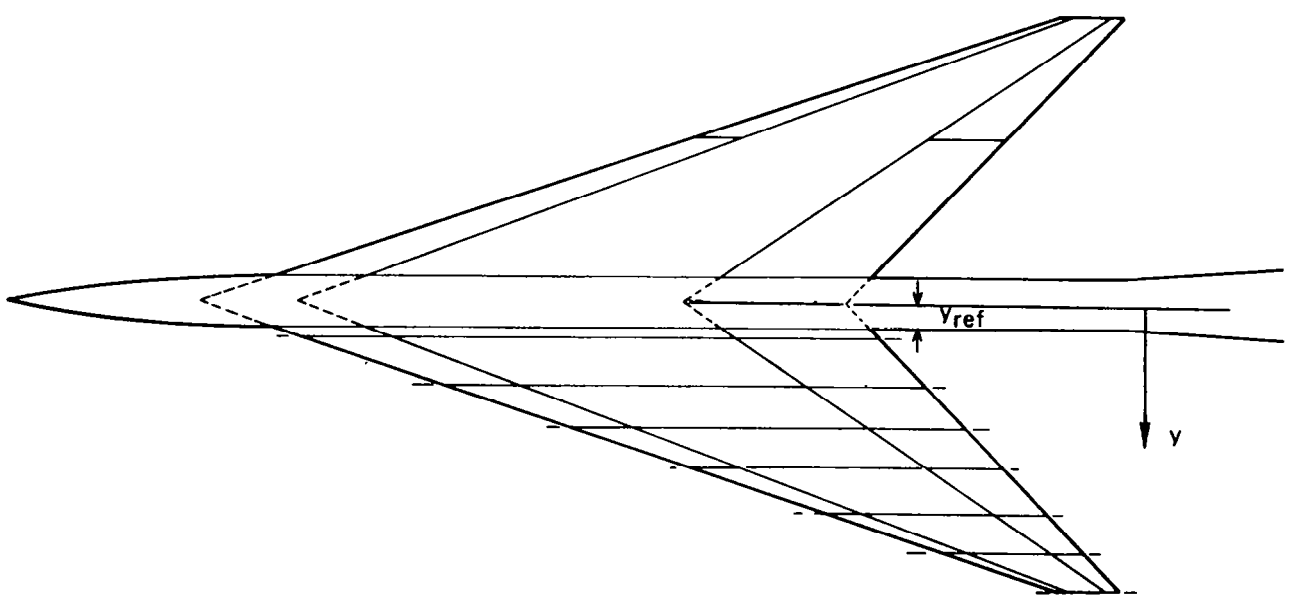

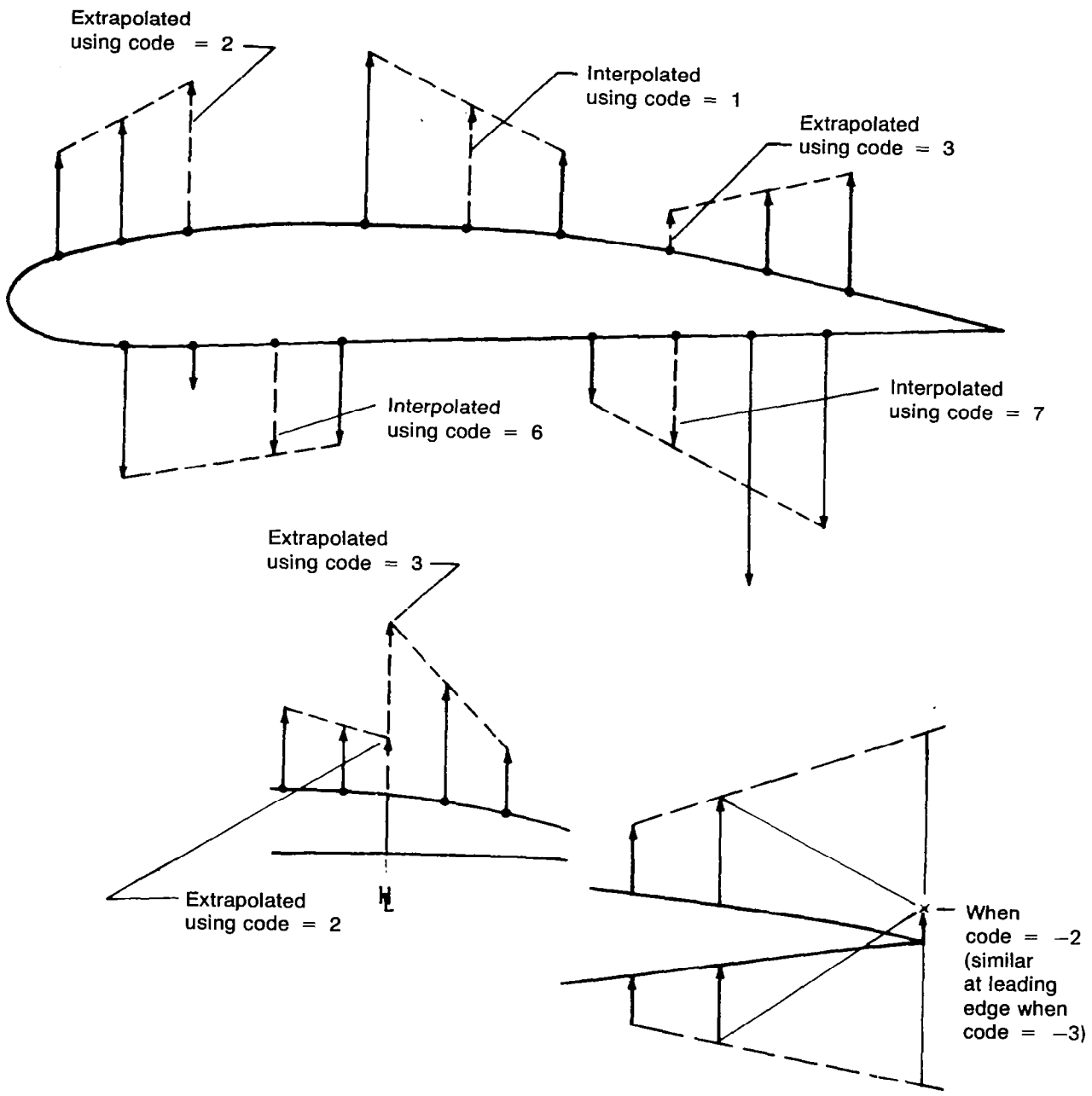

Figure B-1.—Codes Used to Interpolate and Extrapolate

REFERENCES

1. Manro, Marjorie E.; Tinoco, Edward N.; Bobbitt, Percy J.; and Rogers, John T.: Comparisons of Theoretical and Experimental Pressure Distributions on an Arrow-Wing Configuration at Transonic Speeds. Aerodynamic Analyses Requiring Advanced Computers – Part II, NASA SP-347, 1975, pp. 1141-1188.

2. Manro, M. E.; Bobbitt, P. J.; and Rogers, J. T.: Comparisons of Theoretical and Experimental Pressure Distributions on an Arrow-Wing Configuration at Subsonic, Transonic, and Supersonic Speeds. Prediction of Aerodynamic Loading. AGARD CP-204, Feb. 1977, pp. 11-1 – 11-14.

3. Bobbitt, Percy J.; and Manro, Marjorie E.: Theoretical and Experimental Pressure Distributions for a 71.2° Swept Arrow-Wing Configuration at Subsonic, Transonic, and Supersonic Speeds. Proceedings of the SCAR Conference – Part 1, NASA CP-001 [1977], pp. 85-122.

4. Manro, Marjorie E.; Manning, Kenneth J. R.; Hallstaff, Thomas H.; and Rogers, John T.: Transonic Pressure Measurements and Comparison of Theory to Experiment for an Arrow-Wing Configuration – Summary Report. NASA CR-2610, 1976.

5. Manro, Marjorie E.; Manning, Kenneth J. R.; Hallstaff, Thomas H.; and Rogers, John T.: Transonic Pressure Measurements and Comparison of Theory to Experiment for an Arrow-Wing Configuration, Volume I: Experimental Data Report – Base Configuration and Effects of Wing Twist and Leading-Edge Configuration. NASA CR-132727, 1975.

6. Manro, Marjorie E.; Manning, Kenneth J. R.; Hallstaff, Thomas H.; and Rogers, John T.: Transonic Pressure Measurements and Comparison of Theory to Experiment for an Arrow-Wing Configuration, Volume II: Experimental Data Report – Effects of Control Surface Deflection. NASA CR-132728, 1975.

7. Manro, Marjorie E.; Manning, Kenneth J. R.; Hallstaff, Thomas H.; and Rogers, John T.: Transonic Pressure Measurements and Comparison of Theory to Experiment for an Arrow-Wing Configuration, Volume III: Data Report – Comparison of Attached Flow Theories to Experiment. NASA CR-132729, 1975.

8. Manro, M. E.: Supersonic Pressure Measurements and Comparison of Theory to Experiment for an Arrow-Wing Configuration. NASA CR-145046, 1976.

9. Manro, Marjorie E.: Transonic Pressure Measurements and Comparison of Theory to Experiment for Three Arrow-Wing Configurations – Summary Report. NASA CR-3434, 1982.

10. Manro, Marjorie E.: Transonic Pressure Measurements and Comparisons of Theory to Experiment for Three Arrow-Wing Configurations, Volume I: Experimental Data Report – Basic Data and Effect of Wing Shape. NASA CR-165701, 1981.

11. Manro, Marjorie E.: Transonic Pressure Measurements and Comparisons of Theory to Experiment for Three Arrow-Wing Configurations, Volume II: Experimental Data Report – Effect of Trailing-Edge Control Surface Deflection and a Wing Fin. NASA CR-165702, 1981.

12. Manro, Marjorie E.: Transonic Pressure Measurements and Comparisons of Theory to Experiment for Three Arrow-Wing Configurations, Volume III: Data Report – Comparison of Attached-Flow Theories to Experiment. NASA CR-165703, 1981.

13. White, R. P., Jr.; Gangwani, S. T.; and Janaki Ram, D. S.: A Theoretical and Experimental Investigation of Vortex Flow Control for High Lift Generation. Office of Naval Research Report ONR-CR212-223-4, December 1977.

14. Brown, Clinton E.; and Michael, William H., Jr.: On Slender Delta Wings With Leading-Edge Separation. NACA TN 3430, April 1955.

15. Johnson, F. T.; Lu, P; Brune, G. W.; Weber, J. A.; and Rubbert, P. E.: An Improved Method for the Prediction of Completely Three-Dimensional Aerodynamic Load Distributions of Configurations With Leading Edge Vortex Separation. AIAA Paper 76-417, AIAA 9th Fluid and Plasma Dynamics Conference, July 1976.

16. Smith, J. N. B.: Inviscid Fluid Models, Based on Rolled-Up Vortex Sheets, for Three-Dimensional Separation at High Reynolds Numbers. AGARD Lecture Series No. 94 on Three-Dimensional and Unsteady Separation at High Reynolds Numbers, February, 1978.

17. Samant, S. S.; and Janaki Ram, D. S.: Documentation of Computer Codes for Predicting the Lift of Low Aspect-Ratio Wings With Attached Vortex Flows. RASA/SRL Report No. 14-78-04, December, 1978.

18. Abbott, I. H.; and Von Doenhoff, A. E.: Theory of Wing Sections. New York, Dover Publications, Inc., 1959.

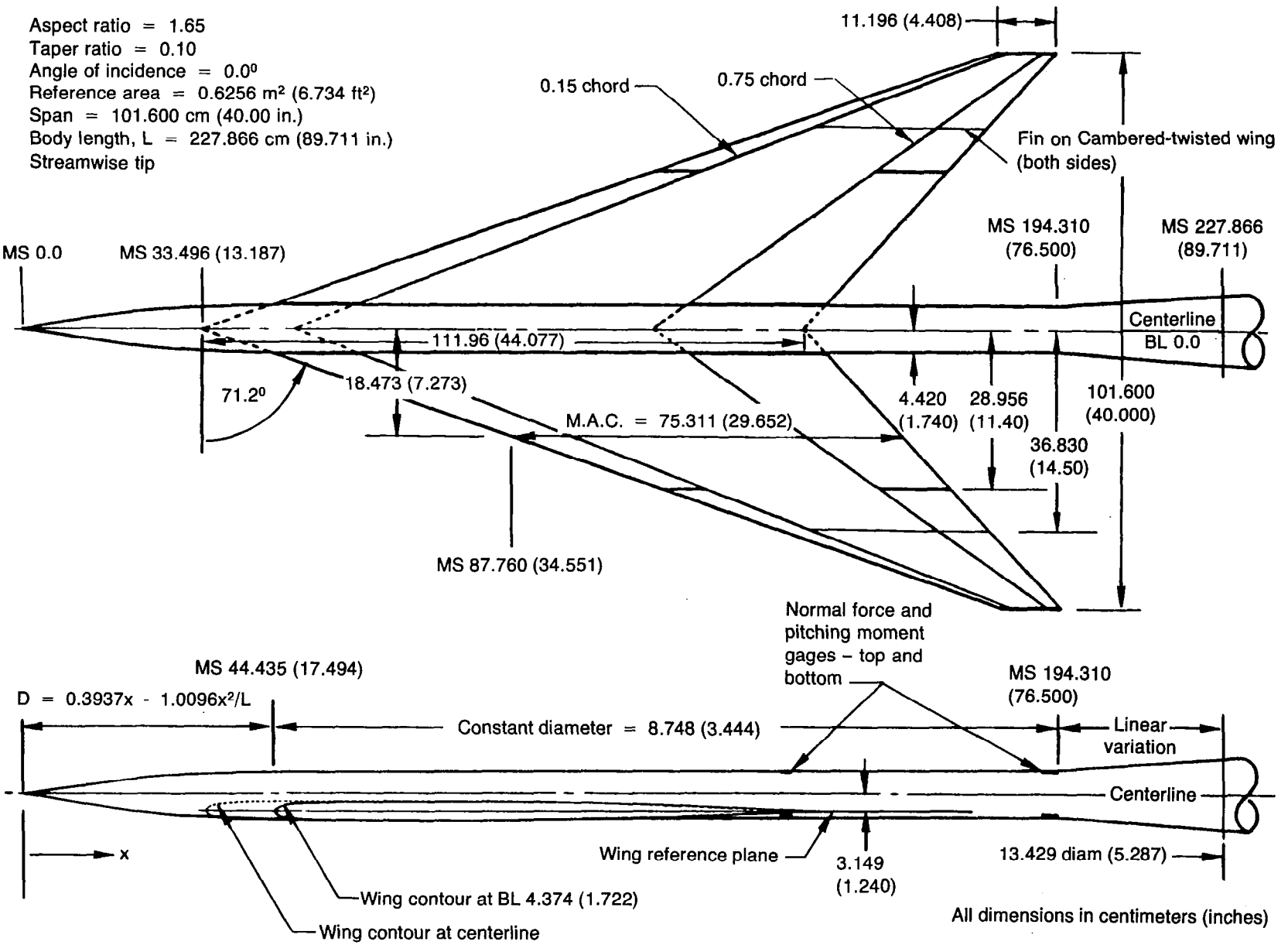

Figure 1.—General Arrangement and Characteristics

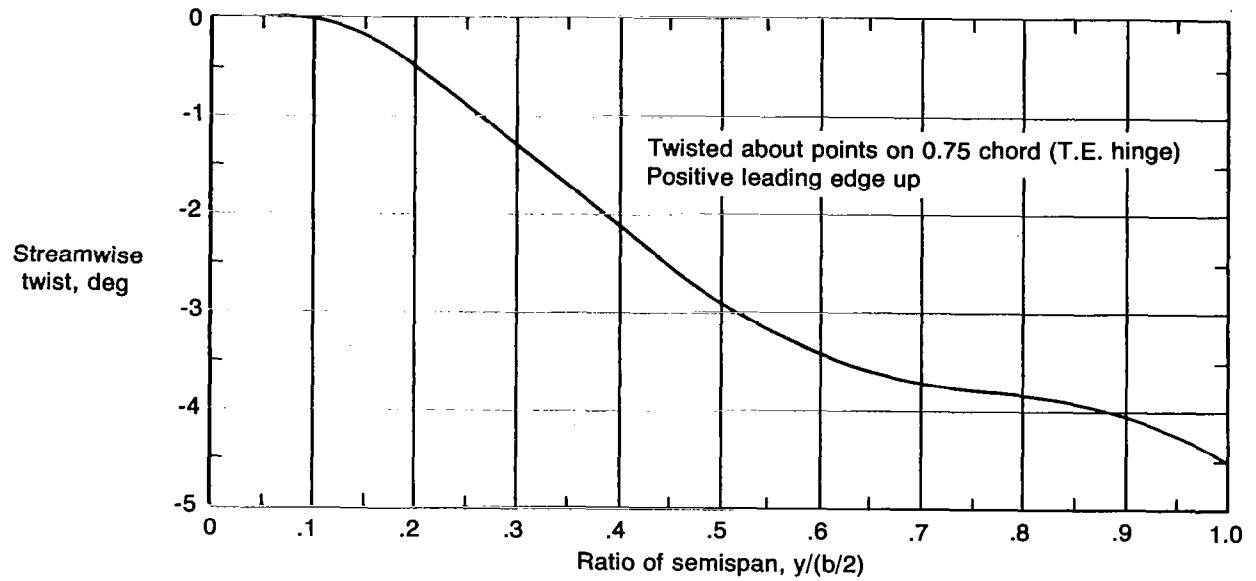

Figure 2.–Spanwise Twist Distribution for the Model Wing

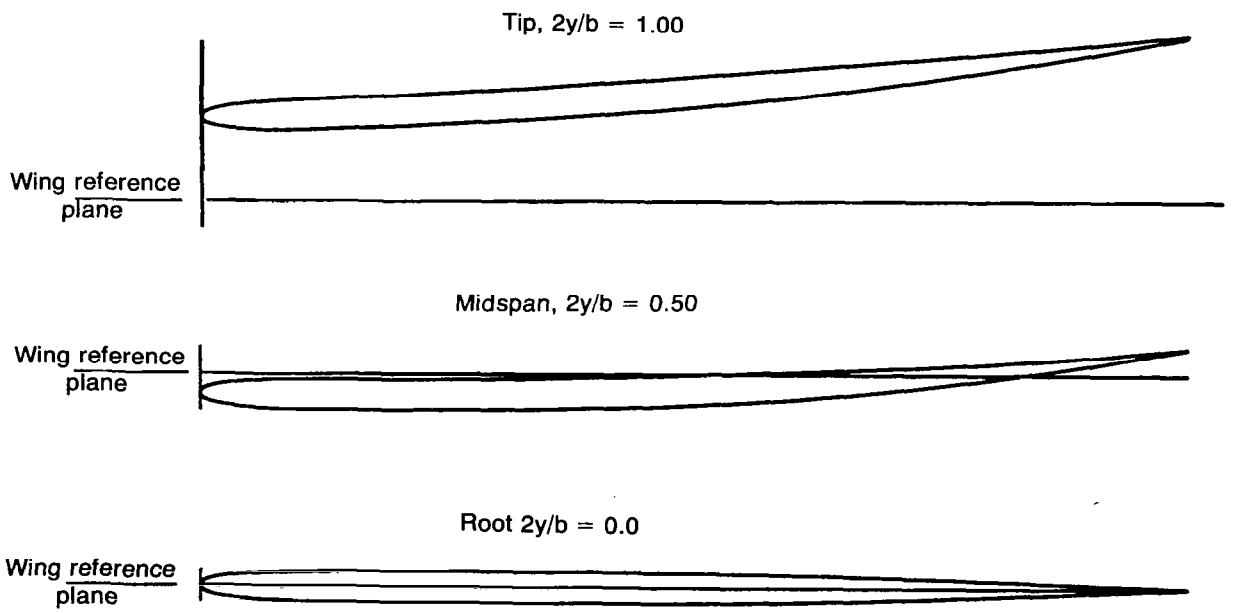

Figure 3.–Cambered-Twisted Wing Section Geometry

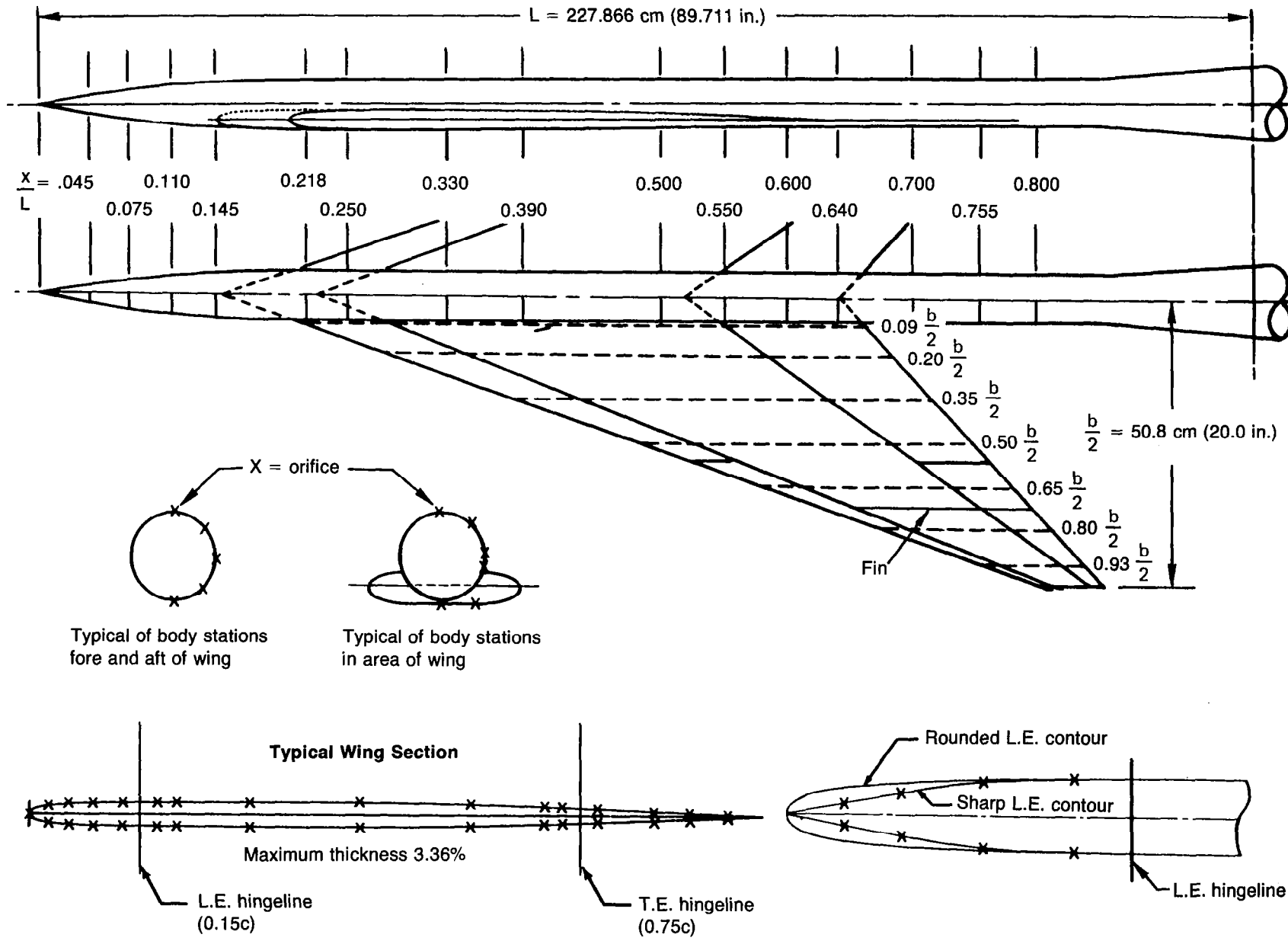

Figure 4.—Pressure Orifice Locations

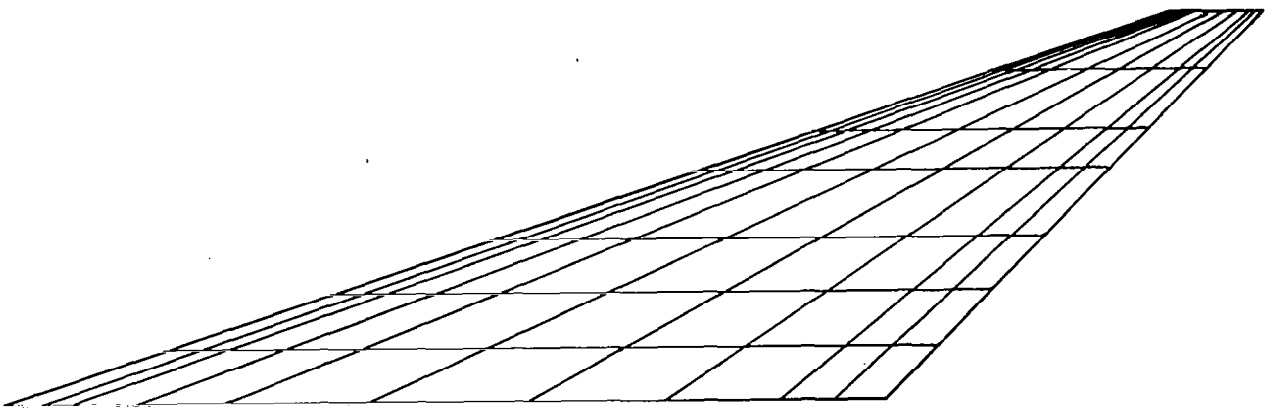

Figure 5.–Surface Paneling for Arrow Wing

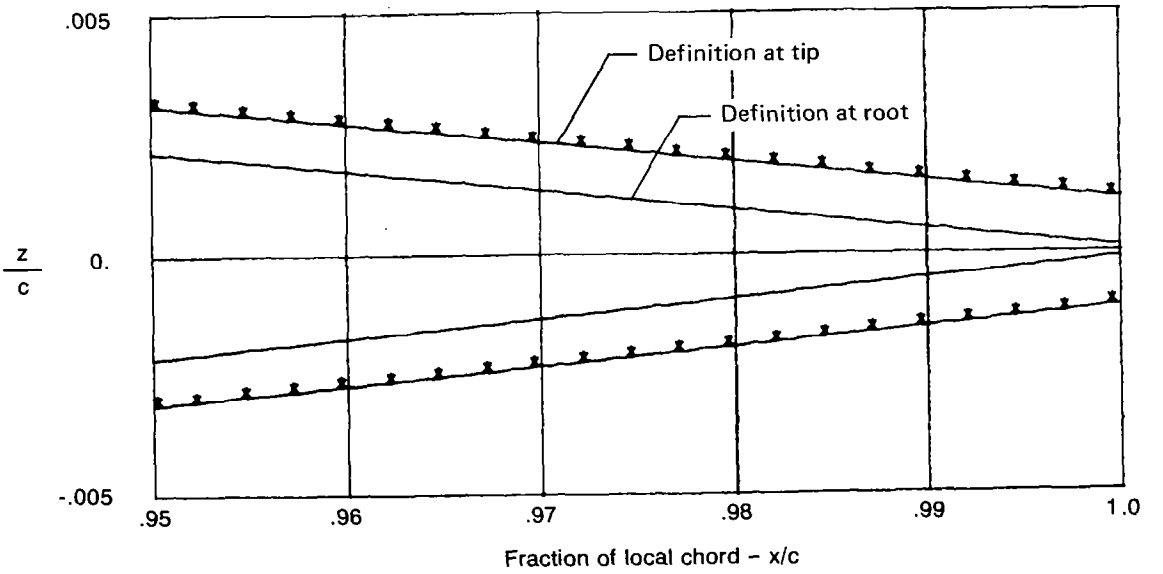

Figure 6.–Comparison of Nondimensional Definition of the Trailing Edge of the Airfoil, Flat Wing

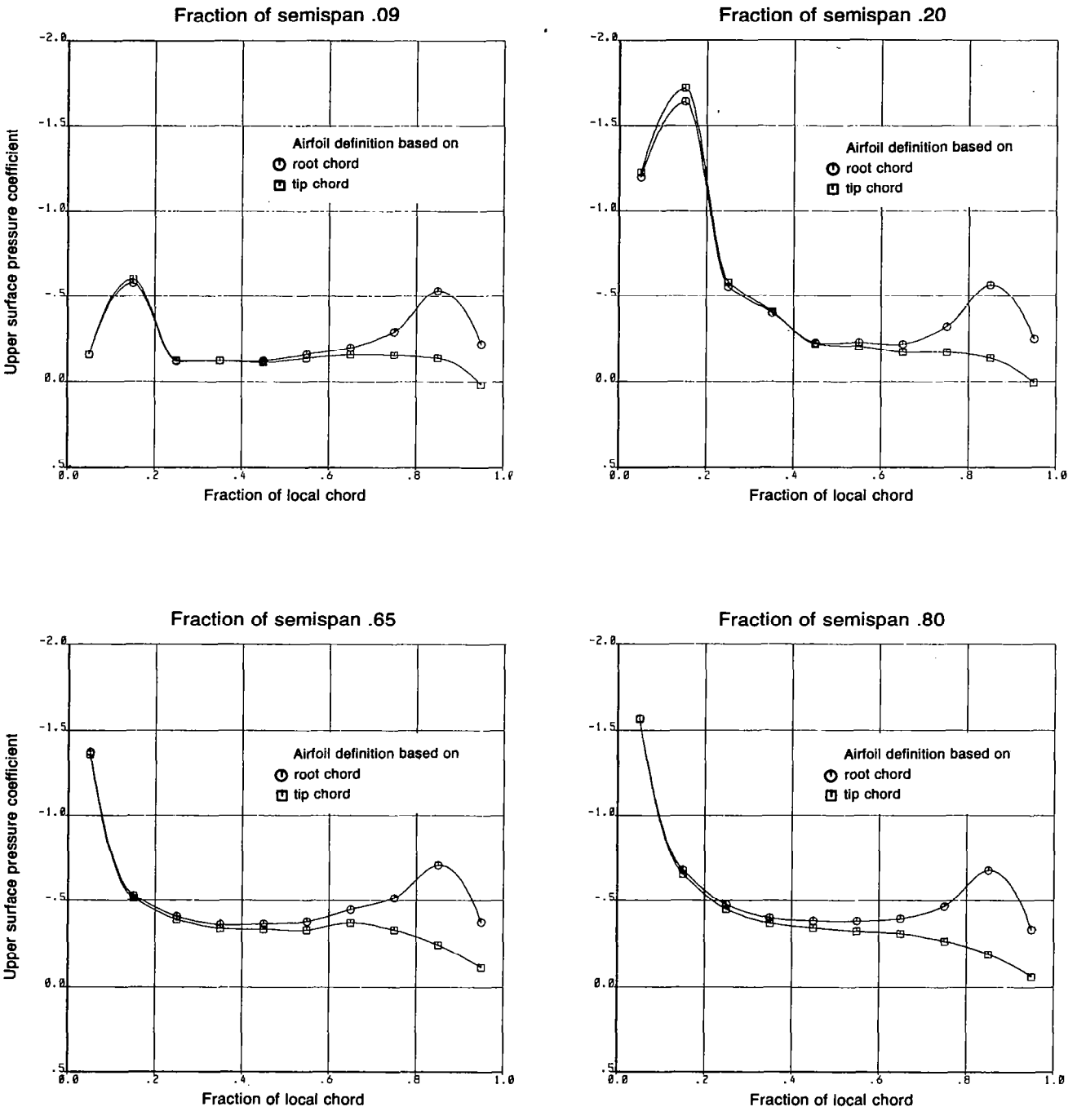

Figure 7.—Comparison of Predicted Pressure Distributions for Two Airfoil Definitions, Flat Wing, Rounded L.E., M = 0.40, $\alpha = 16^{\circ}$

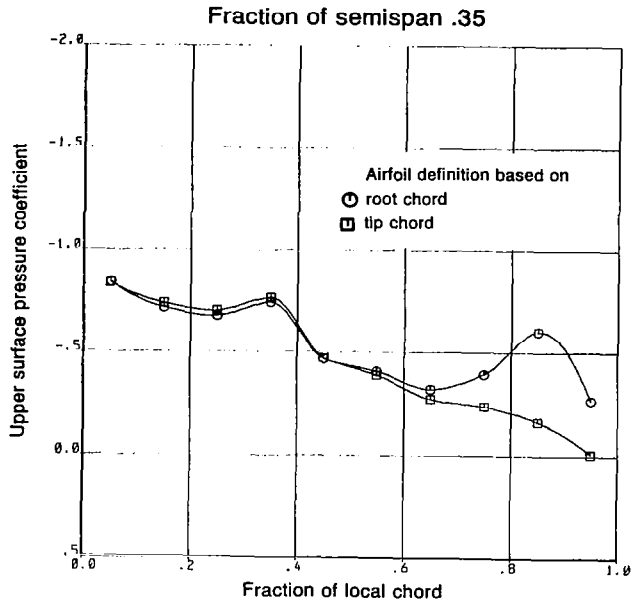

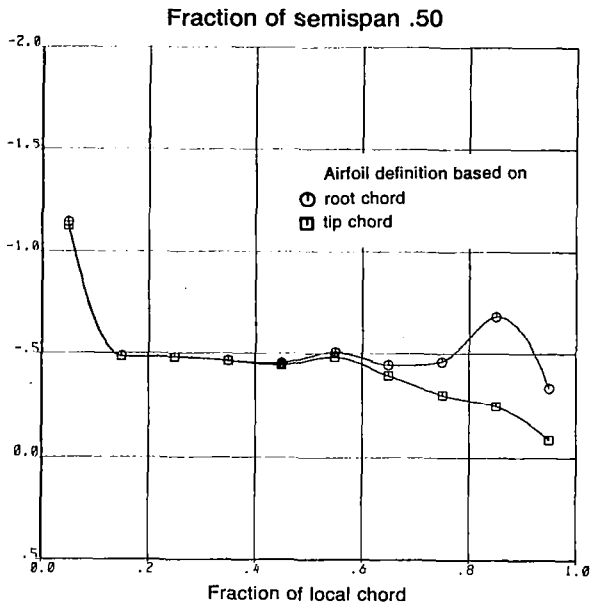

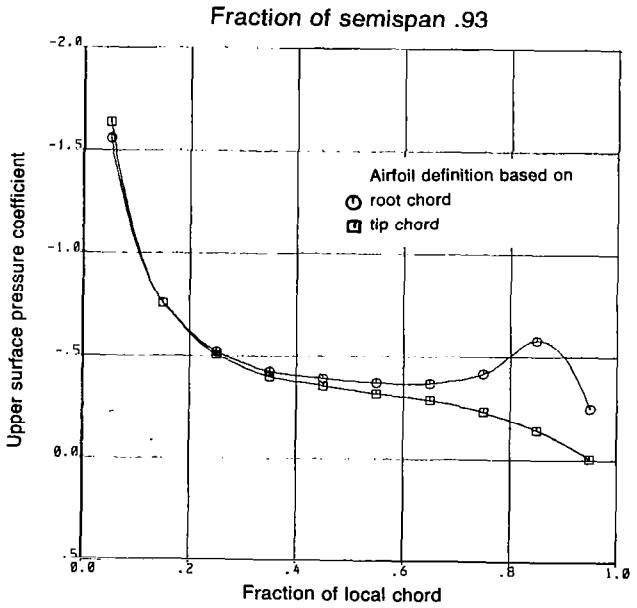

Figure 7.—(Concluded)

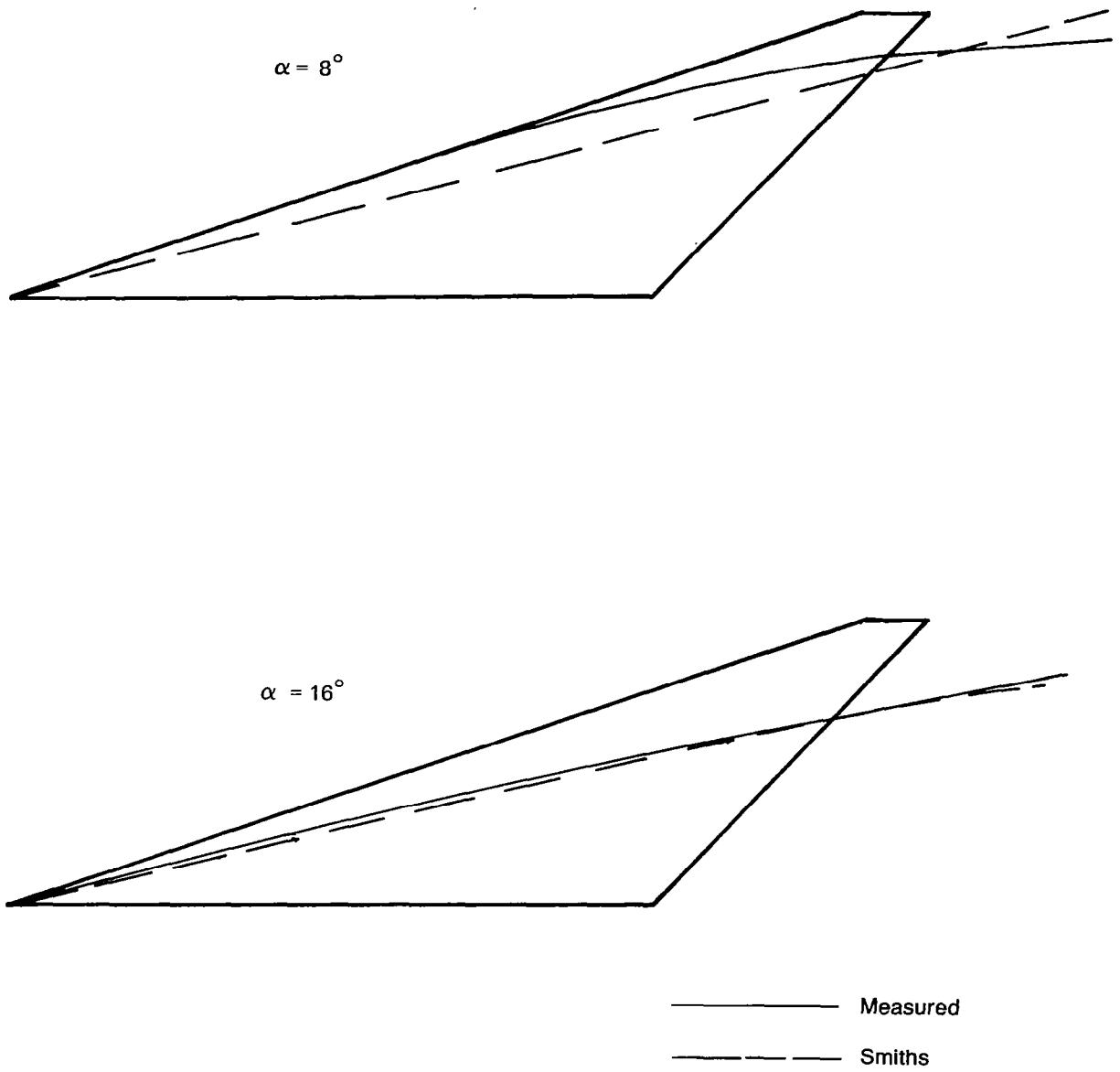

Figure 8.—Horizontal Position of Vortex on Planform, Flat Wing, Rounded L.E., M = 0.40

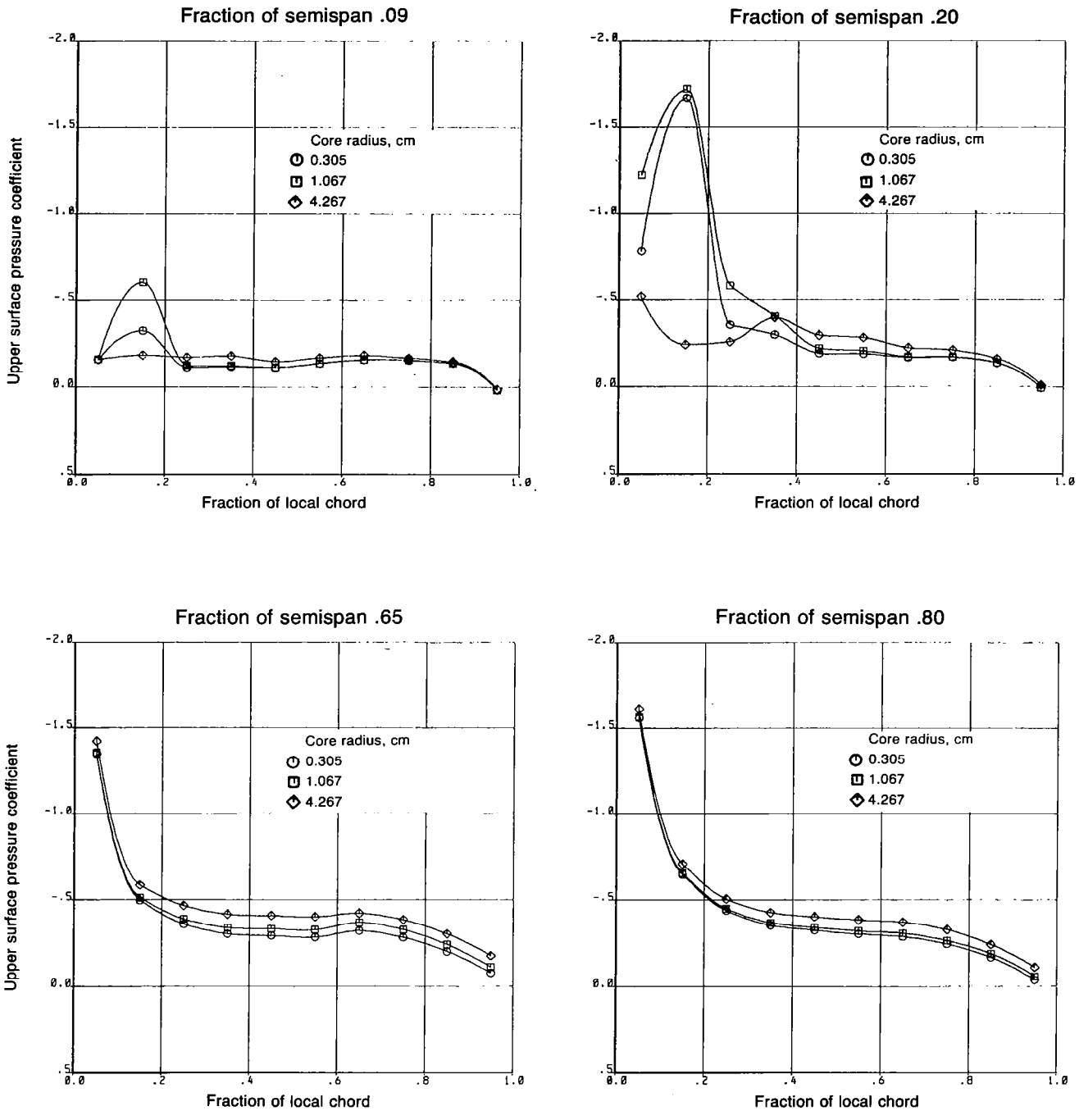

Figure 9.—Effect of Initial Core Radius in White's Method, Flat Wing, Rounded L.E., M = 0.40, $\alpha = 16°$

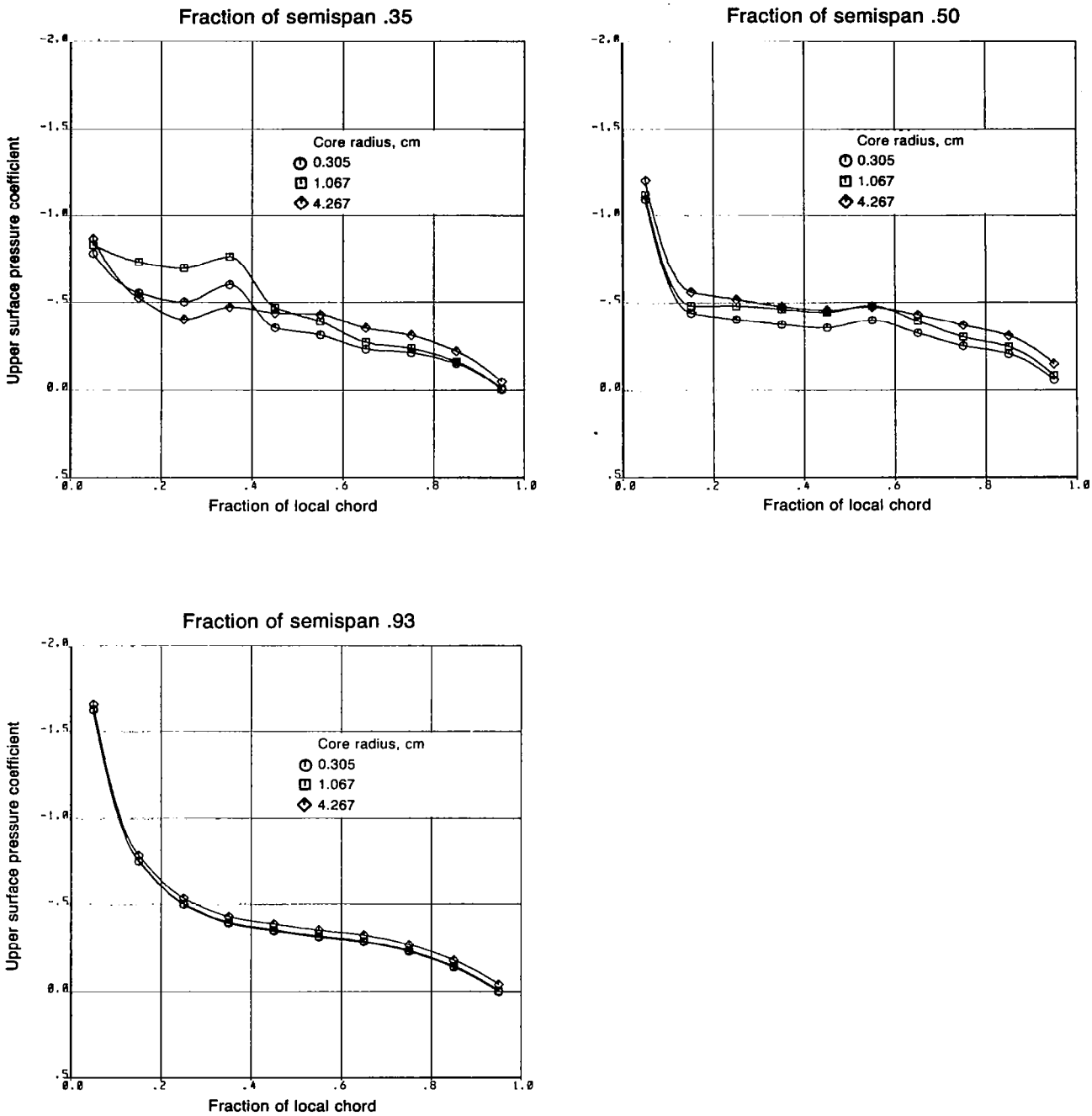

Figure 9.—(Concluded)

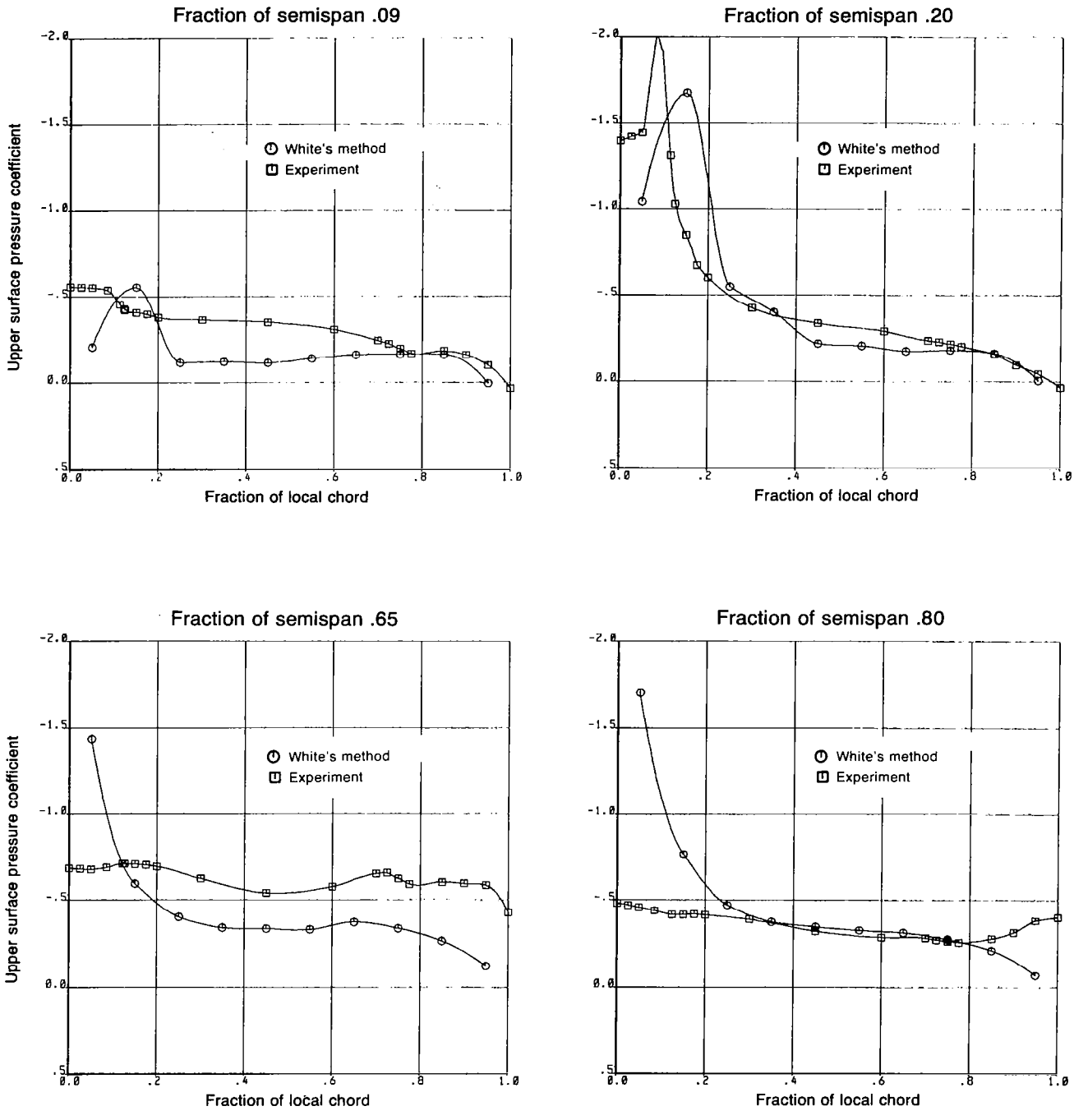

Figure 10.—Theory-to-Experiment Comparison of Wing Upper Surface Pressure Distributions—Flat Wing, Sharp L.E., M = 0.40, α = 16°

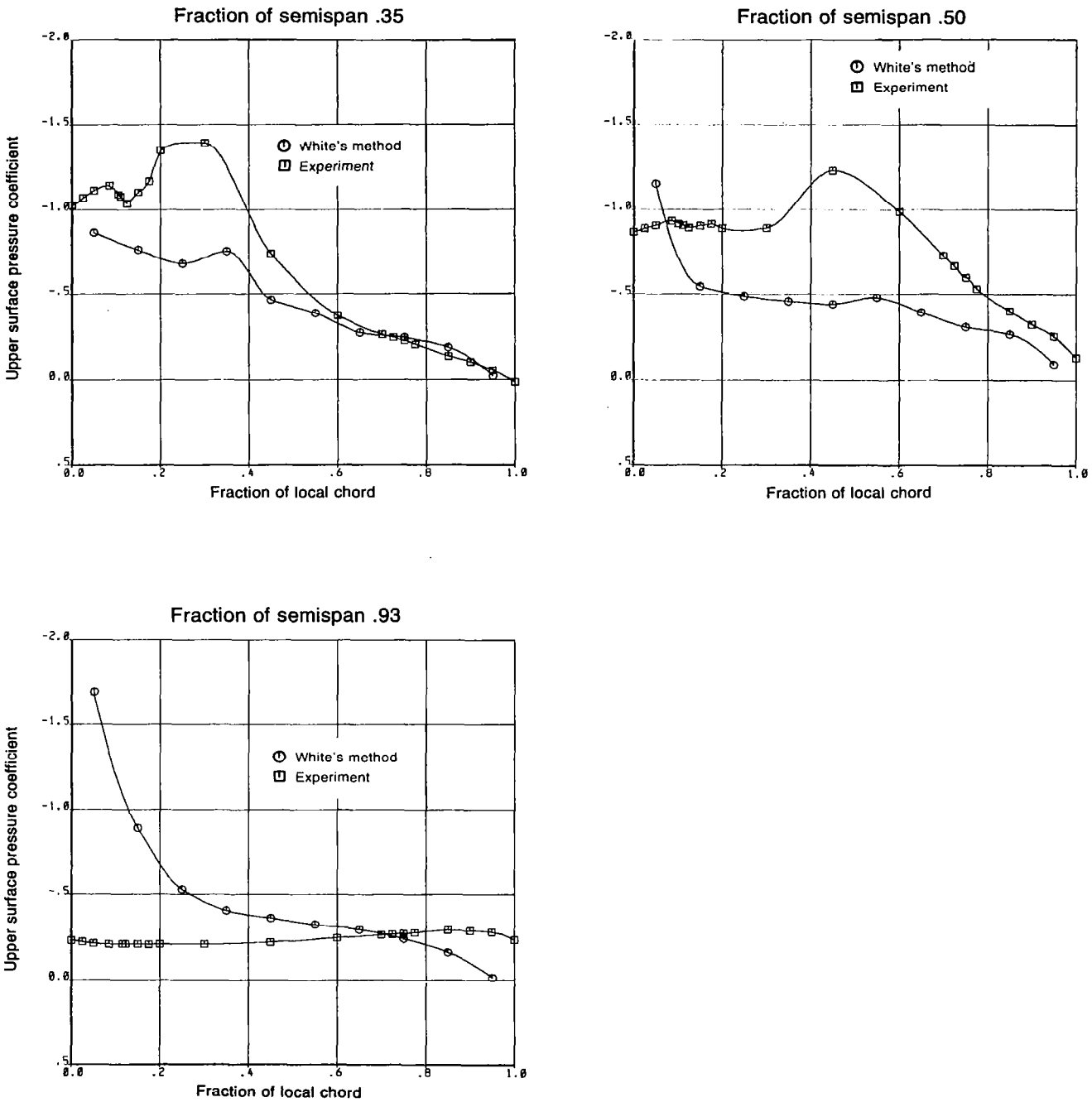

Figure 10.—(Concluded)

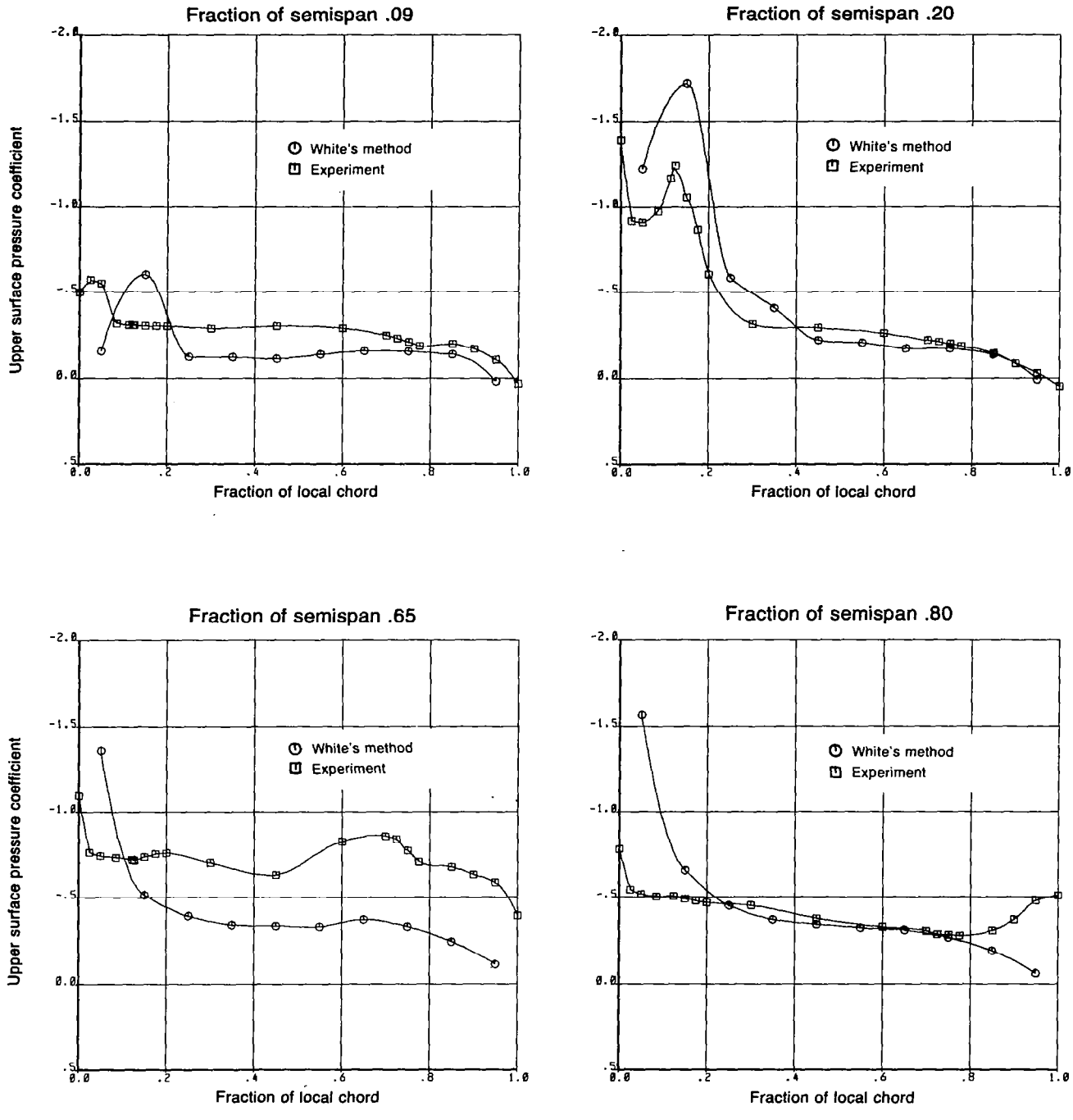

Figure 11.—Theory-to-Experiment Comparison of Wing Upper Surface Pressure Distributions—Flat Wing, Rounded L.E., M = 0.40, α = 16°

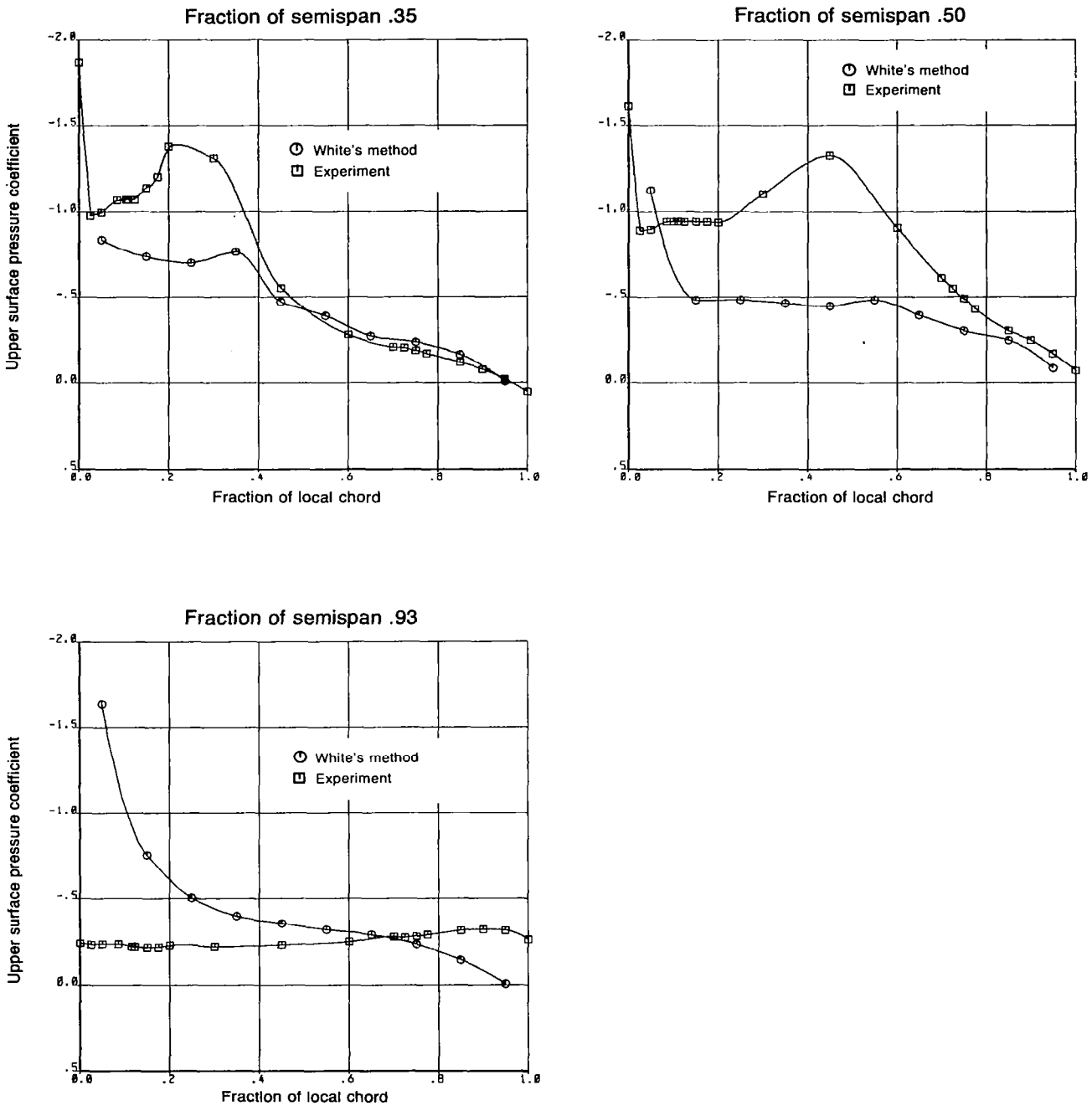

Figure 11.—(Concluded)

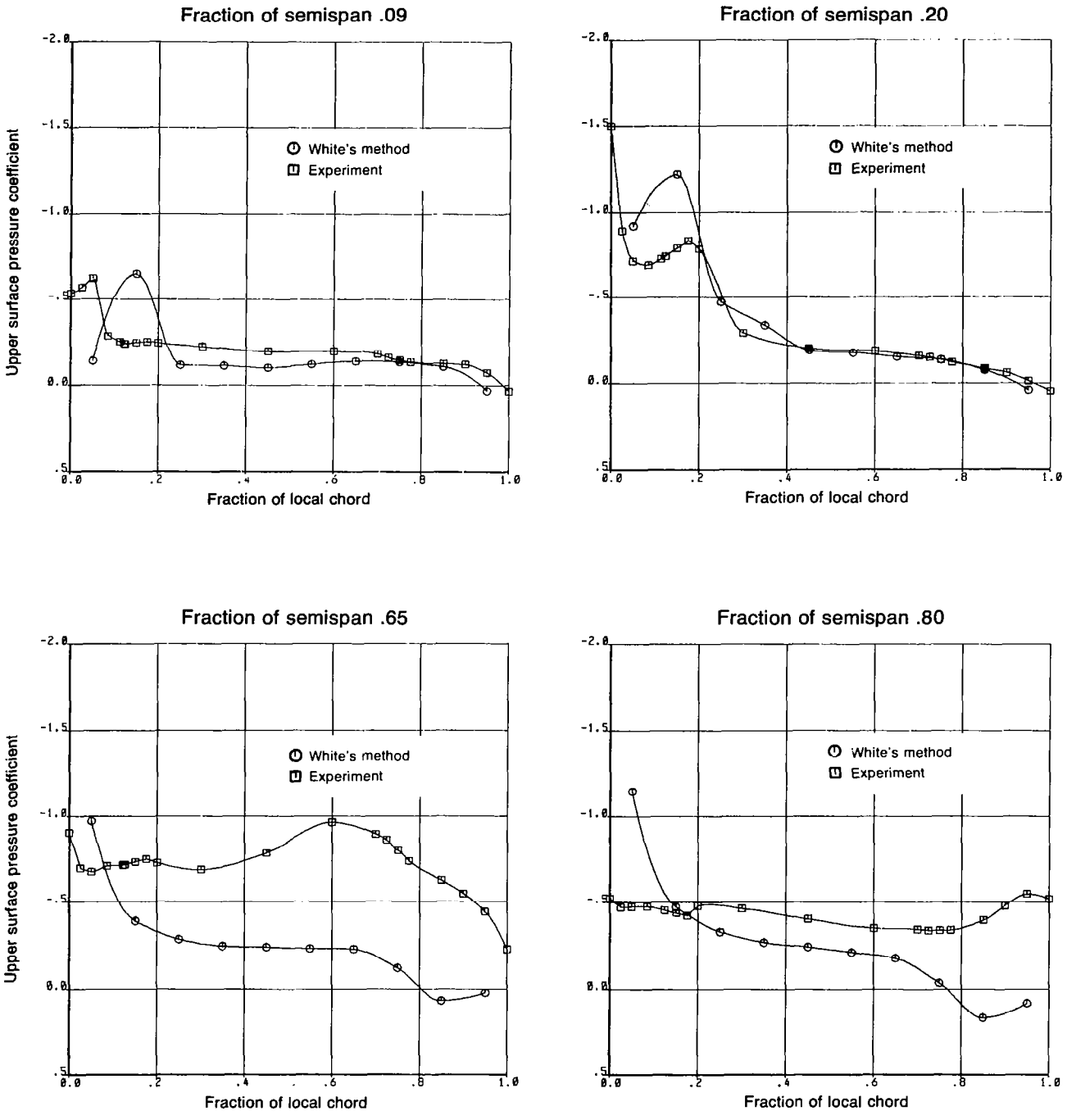

Figure 12.—Theory-to-Experiment Comparison of Wing Upper Surface Pressure Distributions—Twisted Wing, Rounded L.E., M = 0.40, α = 16°

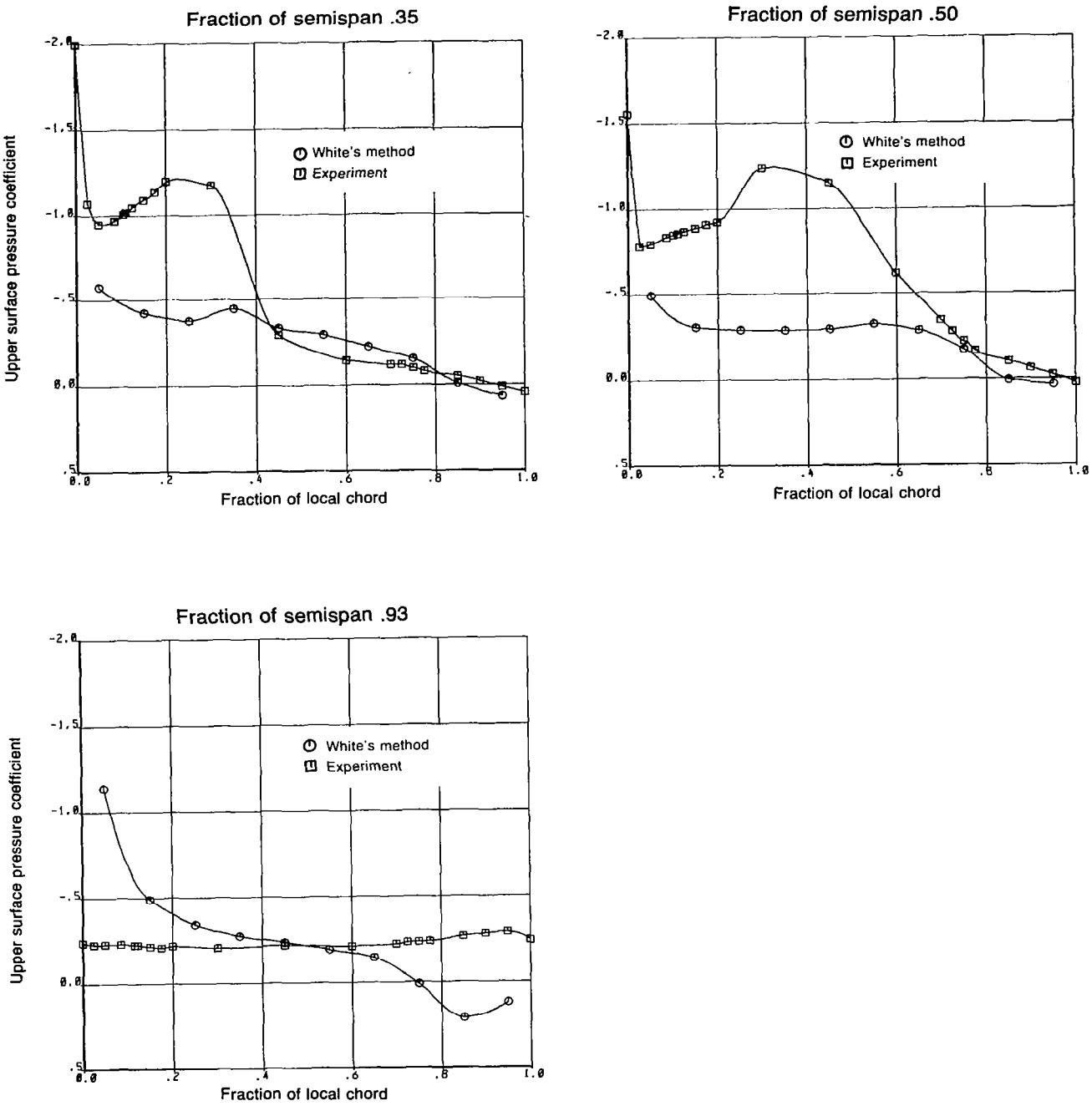

Figure 12.—(Concluded)

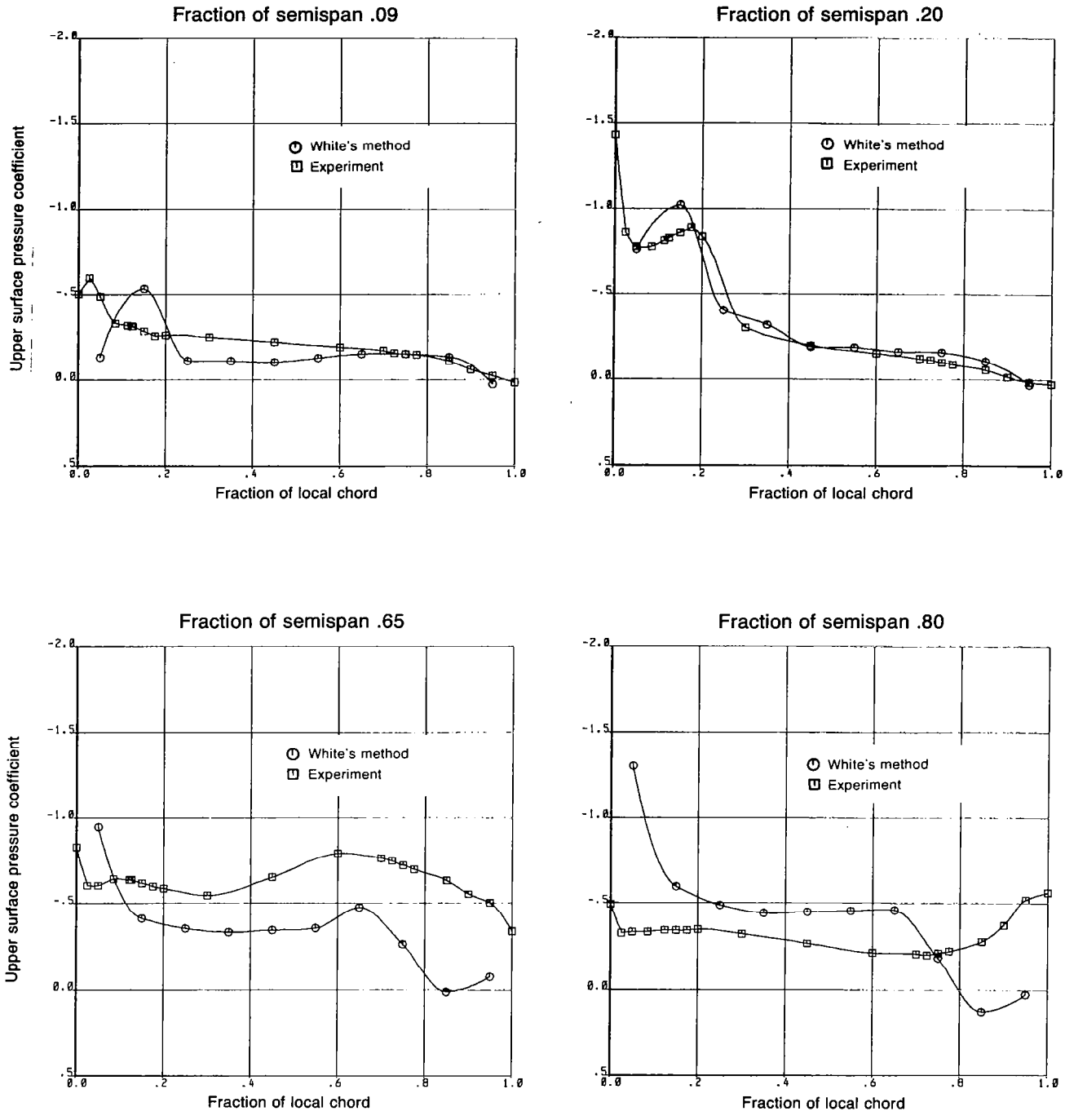

Figure 13.—Theory-to-Experiment Comparison of Wing Upper Surface Pressure Distributions—Cambered-Twisted Wing, Rounded L.E., M = 0.40, α = 16°

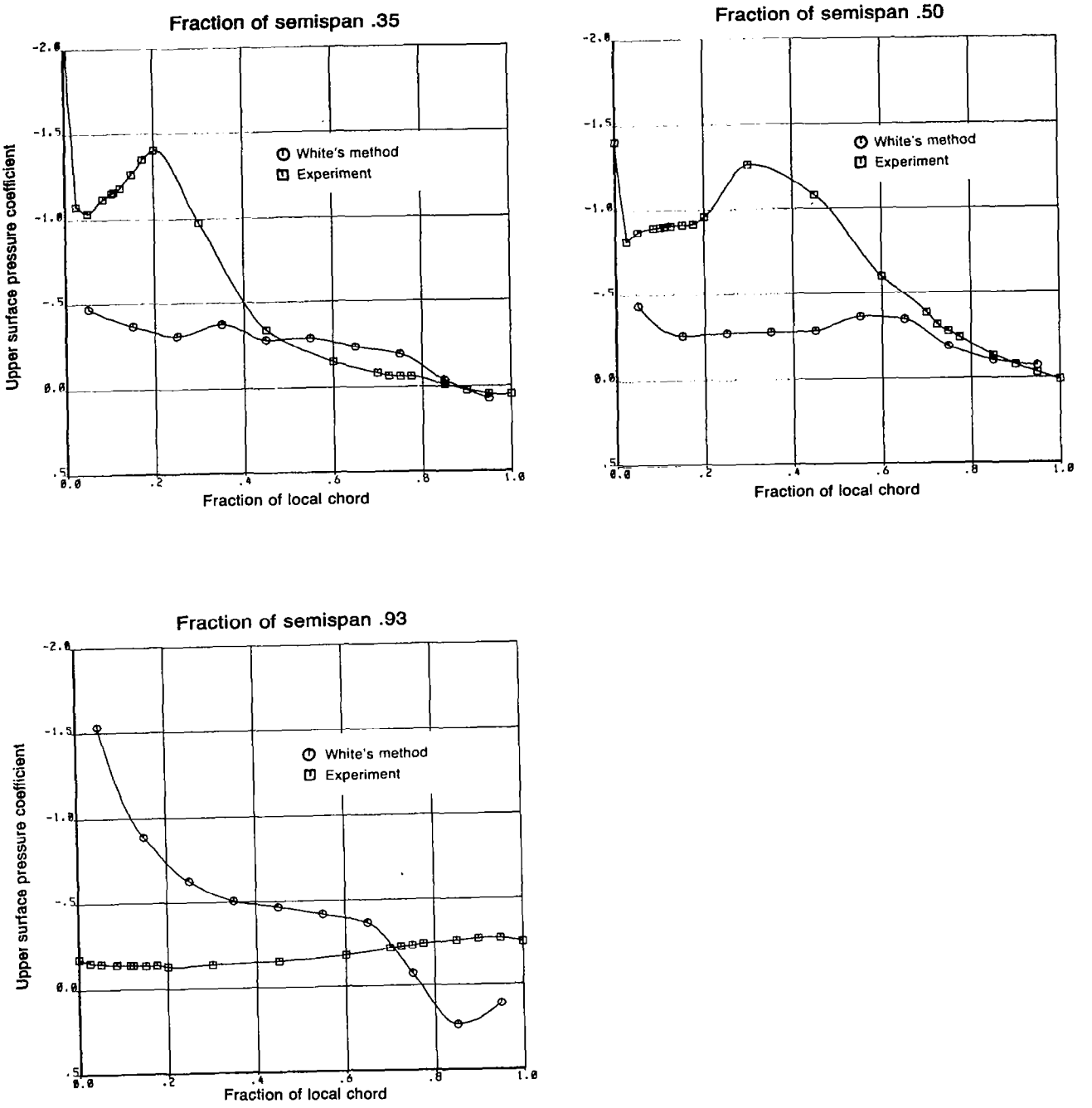

Figure 13.—(Concluded)

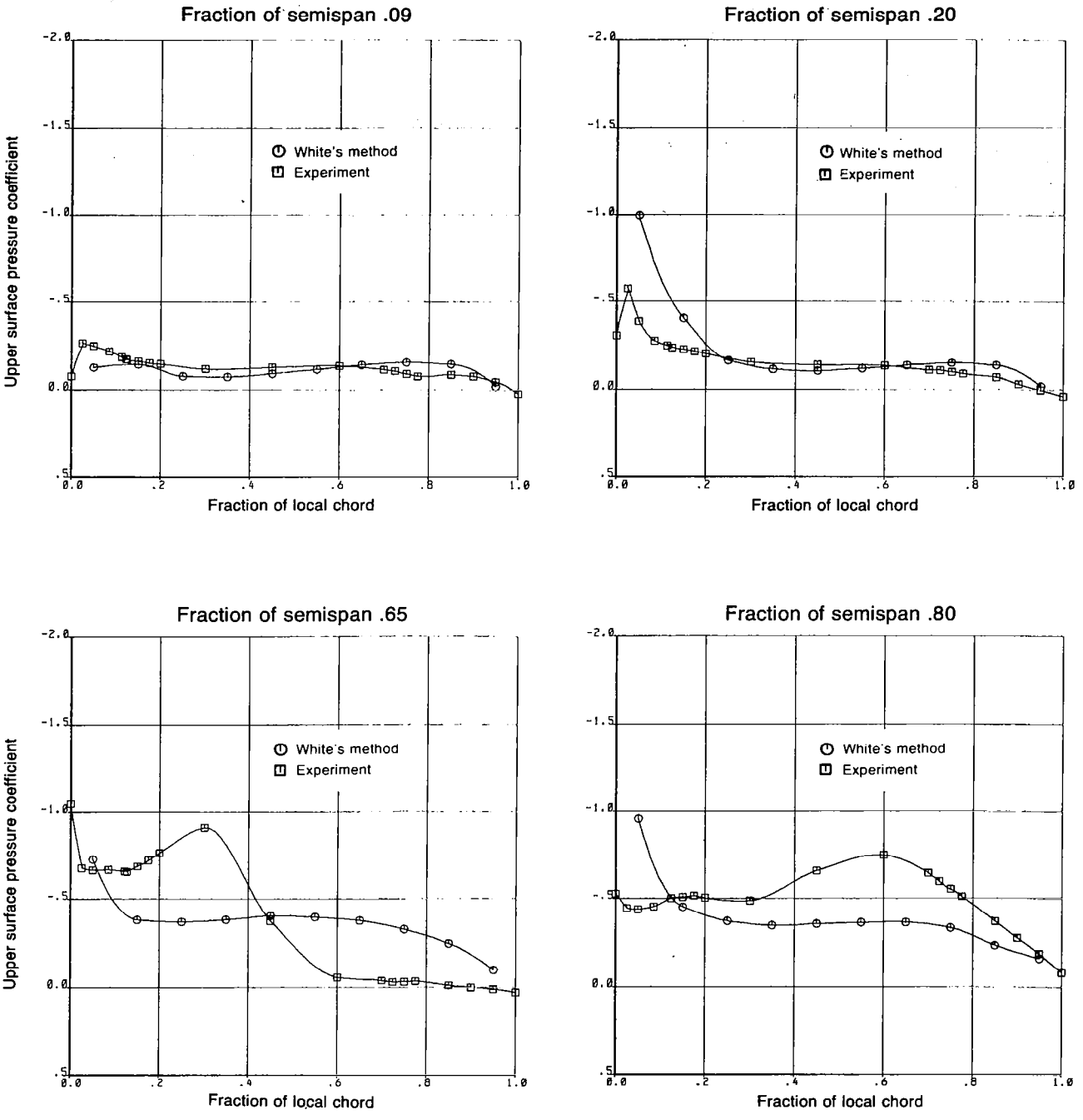

Figure 14.—Theory-to-Experiment Comparison of Wing Upper Surface Pressure Distributions—Flat Wing, Rounded L.E., $M = 0.40$, $\alpha = 8°$

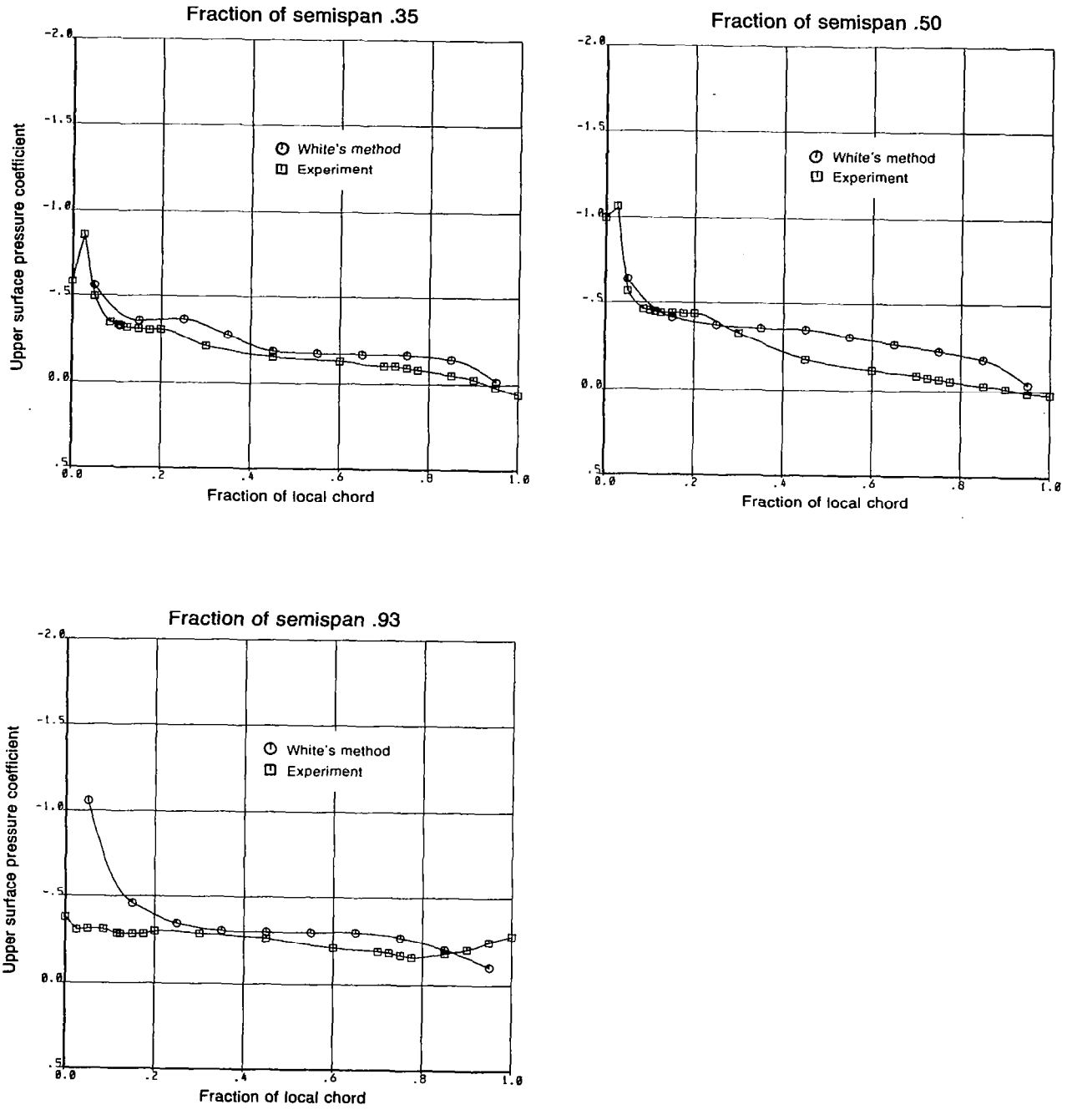

Figure 14.—(Concluded)

1. Report No.	2. Government Accession No.	3. Recipient's Catalog No.
NASA CR-3640		

4. Title and Subtitle	5. Report Date
AEROELASTIC LOADS PREDICTION FOR AN ARROW WING Task I – Evaluation of R. P. White's Method	March 1983
	6. Performing Organization Code
7. Author(s)	8. Performing Organization Report No.
Christopher J. Borland	D6-51762-1
9. Performing Organization Name and Address	10. Work Unit No.
Boeing Commercial Airplane Company P.O. Box 3707 Seattle, Washington 98124	11. Contract or Grant No. NAS1-15678
12. Sponsoring Agency Name and Address	13. Type of Report and Period Covered
National Aeronautics and Space Administration Washington, D.C. 20546	Contractor Report
	14. Sponsoring Agency Code 743-01-12-02

15. Supplementary Notes

Technical monitor – Percy J. Bobbitt, Chief, Transonic Aerodynamics Division, NASA Langley Research Center, Hampton, Virginia.
Principal investigator – Marjorie E. Manro, Boeing Commercial Airplane Company.

16. Abstract

The accurate prediction of loads on flexible, low aspect-ratio wings is critical to the design of reliable and efficient aircraft. The conditions for structural design frequently involve nonlinear aerodynamics.

Two separated-flow computer programs and a semi-empirical method for incorporating the experimentally measured separated-flow effects into a linear aeroelastic analysis were evaluated under this contract. These three tasks are documented separately.

This report describes the evaluation of R. P. White's (RASA Division of Systems Research Laboratories) separated-flow method (Task I). This method was developed for moderately swept wings with multiple, constant-strength vortex systems. The flow on the highly swept wing used in this evaluation is characterized by a single vortex system of continuously varying strength. The data comparisons show, as currently formulated, that this method does not predict the pressure distribution on this highly swept wing.

The evaluation of The Boeing Company's Three-Dimensional Leading-Edge Vortex (LEV) code (Task III) is presented in NASA CR-3642. The development and evaluation of a semi-empirical method to predict pressure distributions on a deformed wing from an experimental data base (Task II) is described in NASA CR-3641.

These evaluations were based on a large experimental data base (for three wing shapes), which was obtained under previous NASA contracts: NAS1-12875, NAS1-14141, and NAS1-14962. Linear theoretical methods were also evaluated under these contracts.

17. Key Words	18. Distribution Statement
Aeroelasticity Experimental pressure distributions Aerodynamic theory Arrow-wing configuration Wind tunnel test	Unclassified-unlimited Subject category 02

19. Security Classif. (of this report)	20. Security Classif. (of this page)	21. No. of Pages	22. Price
Unclassified	Unclassified	94	A05

NASA-Langley, 1983